

Ultrafast Dynamics of Nanoparticles in Highly Intense X-Ray Pulses

vorgelegt von

M. Sc.

Maximilian Jakob Bucher

geb. in Frankfurt am Main

von der Fakultät II - Mathematik und Naturwissenschaften

der Technischen Universität Berlin

zur Erlangung des akademischen Grades

Doktor der Naturwissenschaften

- Dr. rer. nat. -

genehmigte Dissertation

Promotionsausschuss:

Vorsitzender: Prof. Dr. Mario Dähne

Berichter/Gutachter: Prof. Dr. Thomas Möller

Berichter/Gutachter: Prof. Dr. Christoph Bostedt

Tag der wissenschaftlichen Aussprache: 24. Dezember 2016

Berlin 2016

M.Sc. Maximilian Jakob Bucher

Argonne National Laboratory

Chemical Sciences and Engineering Division

Argonne, IL 60439, United States

SLAC National Accelerator Laboratory

Linac Coherent Light Source

Menlo Park, CA 94025, United States

Technische Universität Berlin

Institut für Optik und Atomare Physik

10623 Berlin, Germany

E-Mail: max@max-bucher.de

Web: <https://www.max-bucher.de>

This work is licensed under a Creative Commons “Attribution 4.0 International” license.



More information can be found under

<https://creativecommons.org/licenses/by/4.0/deed.en>

Abstract

abstract text here

Kurzfassung

deutsche Kurzfassung hier

Contents

1	Introduction	1
2	Fundamental Concepts	5
2.1	Why X-ray free electron laser?	5
2.1.1	From bending magnets to undulator	7
2.1.2	Self amplification by spontaneous emission	9
2.1.3	Soft X-ray self seeding	11
2.1.4	Novel X-ray pump–probe techniques	15
2.2	Rare gas clusters	18
2.2.1	Creation of a homogenous cluster	19
2.2.2	Creation of a heterogeneous cluster	24
2.3	Light-matter interaction	26
2.3.1	Small angle X-ray scattering	27
2.3.2	Ionization of matter	30
2.3.3	Charge migration	36
2.4	Ionization of clusters in intense X-ray pulses	38
2.4.1	Formation and expansion of a nanoplasma	39
2.4.2	Imaging of transient states	41
2.4.3	Tampered layers to inhibit the nanoplasma expansion	44
3	Experimental Setup	47
3.1	The atomic, molecular and optical physics instrument and front end enclosure at the LCLS	47
3.2	The LAMP end-station at AMO	52
3.3	Sample delivery	55
3.4	The large area pn-CCD detectors	57
3.5	Time of flight mass-spectrometer	60
4	Methods	63
4.1	The computing environment at LCLS	63

Contents

4.2	pnCCD photon detectors	65
4.2.1	Combining multiple pnCCD detectors	67
4.2.2	Impact of X-ray pump – X-ray probe on diffraction pattern	71
4.3	Acqiris data sampling	72
4.4	Data filtering	74
4.5	Phase retrieval from a single diffraction pattern	75
4.5.1	Principle of phase retrieval	75
4.5.2	2D reconstructions and limitations	76
4.5.3	1D projections and phase reconstructions	80
4.6	2D electron density and diffraction image simulations	81
5	Results and discussion	83
5.1	Pristine xenon pump–probe data	83
5.1.1	iToF traces with xenon as sample	83
5.1.2	Xenon diffraction images	83
5.1.3	Reconstructions of xenon cluster single shot images	83
5.1.4	pnCCD image pump – probe considerations	83
5.1.5	Time of flight data	84
5.2	Pristine helium cluster pump-probe data	84
5.2.1	iToF data with helium as sample	84
5.2.2	Diffraction images of helium cluster	84
5.3	Helium-xenon core-shell systems and pump–probe data	84
5.3.1	Time-of-flight data of helium-xenon core-shell systems	85
5.3.2	Diffraction images of helium-xenon core shell systems	85
5.3.3	Core-shell system considerations	85
5.4	Static data	85
5.5	Conclusion of the X-ray pump – X-ray probe study	85
6	Summary and outlook	87
6.1	Summary	87
6.2	Outlook	87
7	Bibliography	89
8	Appendix	A
8.1	Source alignment	A
8.2	Python code psana example	A

Contents

8.3 Matlab code on spherical integrations	C
8.4 Python code on 1D phase-retrieval	D
8.5 Python code on combining detectors	E

9 Index

I

10 Acknowledgment

K

List of Figures

2.1	Aerial view of the Linac Coherent Light Source.	6
2.2	Schematic setup of an undulator.	8
2.3	Undulator gain curve correlated to microbunching.	10
2.4	SASE single-shot and average spectra	12
2.5	Soft X-ray self-seeding spectra and brilliance of various lightsources.	13
2.6	Schematic setup of an undulator based pump–probe scheme.	16
2.7	Schematic setup of a bunch based pump-probe setup.	18
2.8	Schematic of a supersonic gas expansion into a vacuum.	20
2.9	Schematic of a pickup (gas-)source.	25
2.10	Principle of scattering rays of an atom.	29
2.11	Total absorption cross-sections for helium and xenon.	32
2.12	Schematic illustration of common charge transfer processes	36
2.13	Fluorescence spectra from xenon and neon K-LL Auger spectrum.	37
2.14	Schematic of the nanoplasma creation and expansion.	39
2.15	Measurement and simulation of the nanoplasma expansion in xenon cluster.	42
2.16	Experiment that shows early evolution of the nanoplasma transition.	43
2.17	Time of flight spectra of argon and xenon core-shell systems.	45
3.1	Schematic overview of the AMO beamline instrumentation in the LAMP configuration. The indicated distances below the schematic items are in meters from the interaction region. As the X-ray beam enters the instrument, it can be visualized on a YAG crystal diagnostics (D). A set of 2 slits (S) cuts the beam in the vertical and horizontal to reduce straylight from the Kirkpatrick-Baez (KB) optics. The differential pumping section of the LAMP end-station houses another YAG crystal diagnostics (D) and an option couple in an optical laser (L-IN) on-axis with the X-rays. The front and back pnCCD (F/B-pnCCD) are located downstream of the IR with further beam viewing options (D). From [1].	48

List of Figures

3.2 Left graph: Atomic neon charge state yield from time-of-flight mass spectroscopy as a function of Z, relative to optimal focus position Z = 0. Z = 0 ± 1 is a favorable length for sample injection. Right diagram: Comparison of atomic neon charge state yield from time-of-flight mass spectroscopy for different cases. Red: Experimental data from October 2009 with 4 blades (S) opened. Green: Experimental data from November 2013 with (S) closed. Blue: Experimental data from November 2013 with (S) opened.	50
3.3 a)-d), ex-situ microscope imprint study of a lead tungstate (PbWO_4) sample that was irradiated with single LCLS pulses at 1600eV at different gas attenuation using the LCLS gas attenuator. e) crater area as a function of the gas attenuation. The slope of the curve could be used to determine the focal spot size to be TBD.	51
3.4 Overview of the AMO instrument in the LAMP end-station configuration. From left to right, the beam propagates through the Kirkpatrick-Baez (KB) optics, the differential pumping (DP) section, the interaction chamber (C1), the front pnCCD chamber (C2-1), the rear pnCCD chamber (C2-2) and finally the diagnostics (DIA) system. The C1 chamber has the AMO rare-gas cluster jet installed at the most distant conflat vacuum flange. For scale, the large, open conflat flanges on the C1 chamber are 12 inch.	52
3.5 Inside view of the C1 chamber showcasing the interaction region.	53
3.6 Side view of the rear and front pnCCD detector in C1, C2-1 and C2-2. The interaction region (IR) is in the center of C1. The beam propagates along the Z-axis where the rear pnCCD is placed 731.68 mm away from the IR (original engineering distances). The half detector height is 38.3 mm and results in a half scattering angle of 4.26° . With the gate-valve installed, the front pnCCDs are able to travel along the z-axis from 370.9 mm to 120.9 mm downstream of the IR. The front pnCCDs position along the y-axis is adjustable and they can detect photons up to 86.3 mm from the beam axis. At maximum extension, the pnCCDs are thus able to detect photons up to a half scattering angle of $\frac{\Theta}{2} = 38.84^\circ$. TBD	54
3.7 caption TBD	55

3.8 Schematic of the Parker-Hannifin Series 99 pulsed in-line valve and custom copper nozzle. The nozzle is clamped to the pulsed valve using an indium gasket to seal. The vespel poppit is attached to the magnetic cylinder and opens or closes the valve. If a current is run through the solenoid, the magnetic cylinder and thus the valve actuated. From [2]	57
3.9 Geometry of a single pnCCD module with a detailed view of the beam conveying hole. A single module consists of 1024×512 pixel. Each pixel is $75\mu m$ which results in an active area of $76.8 \times 38.4 mm^2$. The chip is surrounded by a non-active edges, which are $1.15 mm$ wide on beam facing edges. The hole reduces the active area on one module by 60×22 pixel, or 4.5×1.65 mm and allows the beam to propagate through a $2.4 \times 1.7 mm^2$ hole.	58
3.10 Drawing of the time of flight spectrometer.	61
3.11 Sideview of the spectrometer showing ion, electron and photon trajectories upon interaction with LCLS. The image was created with SIMION. From [3]	62
4.1 Diagram of the computing environment at LCLS and DAQ traffic. The recorded data is exchanged through Ethernet and after digitization, is stored on a cache and FFB cluster, where psana computer have access to the online environment during the experiment. Eventually, the data is moved to the more permanent offline environment, where data can be analyzed on psana computers or through a load sharing facility. See more in text. From [4]	64
4.2 ADU histograms from electronic noise of not illuminated pnCCDs in highest gain mode. The green, plus symbols reflect a histogram of ADU values from raw electronic noise of pnCCD pixel. One can see that the noise is set off zero at $\mu_r = 1515$ ADU and has a standard deviation $\sigma_r = 136$. The same data shifts to the blue stars are after applying the pedestal subtraction. The noise is centered around $\mu_p = -3$ and it's standard deviation is reduced to $\sigma_p = 109$. For the red data points, the common-mode corrections have additionally been applied. Now, the noise is well-centered at $\mu_c = 0$ ADU and σ_c is significantly reduced to 17. Note again, that this is an ADU histogram of purely electronic noise in highest-gain imaging mode.	66

List of Figures

4.3	A combined pnCCD image using the full image of the front pnCCD and a down-sampled image of the rear pnCCD. The red circles in the image are drawn in to visualize the alignment of the detectors. As described in the text, the intensities in the image are normalized and corrected for different electronic gains and distance to specific detectors. The shaded areas are not covered by the pnCCDs and are therefore masked out.	69
4.4	In this graph a 2D diffraction image was projected onto 1D assuming a spherical symmetry of the diffraction pattern. The green data points are gathered from the rear pnCCD and the front pnCCD data points are reflected by the blue data points. The red curve is a simulated scattering curve from an ideal sphere that has a radius of 49nm . The amplitude of the red curve has been fitted to the data points and it agrees well with the data over 8 diffraction rings. The gray shaded area shows the transition area from rear to front detector.	70
4.5	Left: electron density of an expanding spherical symmetric nanoplasma. Right: red line, scattering of an intact sphere. Brown, scattering of an expanding sphere with $k = 5\text{nm}$. Blue, combined scattering of an intact and expanding sphere that has been pumped with 10% and probed with 90% of the overall pulse energy. See more information in text.	71
4.6	caption. Left image from [5]	72
4.7	caption	73
4.8	Left: Average Xenon cluster size of intense hits as a function of pump-probe delay Δt . Right: Average intensity on the front pnCCD of intense hits as a function of the pump-probe delay Δt	74
4.9	Example of a phase retrieval algorithm.	76
4.10	A set of reconstructions of Xe-cluster yielded from the diffraction pattern in figure 4.3 and the corresponding real-space error over number of iterations. The real space image gathered from the rear pnCCD uses no data from the front pnCCD. This reconstruction shows a not spherical object although the density distribution appears to be reasonable for a nanoparticle. The real space image reconstructed from the full front and rear pnCCD data set appears to be a spherical object but the missing areas disturb the diffraction pattern and it has become unphysical. The Xe-cluster reconstructed without the dead areas has the expected spherical shape and the density distribution appears to be physical.	78

4.11 Left: Electron density of a $R \approx 100\text{nm}$ expanding sphere with $k = 5 \text{ nm}$, projected onto a 2D plane. Right: Blue curve, spherical projection of the 2D projection to 1D. Red dashed line, point of expanding density at $k = 5 \text{ nm}$	81
4.12 Comparison of analytical scattering from a sphere of radius $R = 202 \text{ nm}$ (black curve), equation 2.39, and scattering of a sphere of radius $R = 202 \text{ nm}$ from 2D simulations projected onto 1D (green, dashed curve). Envelope of scattering intensity, called Porod's law, which is $\propto q^{-4}$ (red curve). The analytical scattering and developed simulations agree well with each other.	82
5.1 caption. MAKE IMAGE NICER	84
8.1 caption	B

List of Tables

2.1	Parameter K_{gas} values for rare gases.	23
2.2	Differential absorption cross-sections and ionization potentials for xenon. .	34
2.3	Absorption cross-sections and ionization potentials for xenon and helium .	34
2.4	Atomic scattering factors for helium and xenon.	35
3.1	caption TBD.	56
3.2	Typical generated ADU values and dynamic range using 1k eV photons at all pnCCD gain settings. It is a valid approximation to linearly extrapolate to other photon energies.	59
3.3	Set voltages to the time of flight spectrometer. Ion side use only.	62
4.1	Typical parameter used in the Hawk software package	77

1 Introduction

Investigating matter with light is one of the most fundamental approaches to study nature. Whether we look at things by eye or use more advanced methods for example using lasers, it is an invaluable tool to understand nature. Through light, we can study the shapes of objects, investigate fundamental particles, study quantum mechanics and so much more. Key aspect in almost any study involving light is its wavelength. The wavelength of light can make you feel cozy at home with a modern LED light bulb or shroud your home in a blue, uncomfortable haze when you use older light bulbs. At the end of the 19th century, Röntgen discovered the then novel X-radiation and quickly realized its impact due to its different wavelength. Soon, he was able to take first medical X-ray images, later X-rays could be used to investigate fundamental aspects of atoms. The success story continues until today, where short wavelength X-rays enables the study of the workhorse in human bodies, namely proteins. The shape of a protein, which is only a few nanometers in size, cannot be seen in a microscope anymore and only X-rays can be used to unravel their shape with sufficient resolution. The shape of a biomolecules is of particular interest because it defines its biological function. The chemical structure of most human biomolecules are fairly similar and affect the function little. Medical drugs often aim to affect biological functions such that the specific shape of a protein becomes very important for drug research and drug design.

However, there is more to light than just its wavelength. The intensity of light plays a crucial role, for example when we are sitting in front of a fire and the warm glaze of infrared (IR) radiation can be felt on our skin. Anyway, using high intense radiation allows us to create an environment comparable to the inside of the sun, where fusion processes create energy and other interesting high energy processes are happening. Intense light is also needed if you want to study the very small because the interaction between matter and light becomes very small on length scales of for example a protein. To study the shape of a protein a certain interaction is needed and since we do not want to change the protein, we have to adjust the intensity of light.

Last but not least, light can come in short flashes for example when taking a photograph. At night, when the flash is too long, the pictures often get washed out. It is

1 Introduction

similar when you study nature, if you want to look at some movement or more general dynamics, your light flash must be short enough to resolve this dynamic, otherwise it gets washed out. Proteins function also through movement. Many of their dynamics could already be deciphered but it is unclear what one would discover if one would look at even faster timescales.

Summarizing, a light flash can be described by its wavelength, intensity and duration. To study matter, e.g. proteins, one has to optimize these three parameters a lot. Therefore, a new kind of light source was developed that is particularly interesting for imaging the very small on the nanometer scale. The first one of these light sources, a so called free electron laser (FEL), was built in Hamburg, Germany. First experiments with FELs that showed proof of principle studies showcasing capabilities of FELs as a highly intense and ultra short light pulse source. As a result, more advanced X-ray free electron laser (XFEL) were built to further improve capabilities. The first hard XFEL was built in Menlo Park, California at Stanford University and is called the Linac Coherent Light Source (LCLS). It is a 4.1 km long machine¹, the most straightest building in the world², is build underneath the ground and the interstate I-280 crosses it via a bridge³. This massive machine delivers what is needed to use imaging techniques that have been out of reach so far. To name a few, with LCLS it is possible to study protein crystals of much smaller size, one can study single particles for example viruses and cells. And LCLS is not limited to imaging techniques, one can study atoms and molecules in thus far unreachable regimes and also understand magnetism better. The reason these new areas of study area accessible through LCLS lay in the light parameters. LCLS produces light with a very short wavelength (X-rays from 4.6 nm to 0.1 nm), it has a very high intensity ($10^{18} Ws/cm^2$) and ultra short pulses ($1 - 500 fs$). The combination of these parameters is unique in the world and enables us to look at things that have been hidden so far.

Let us now imagine that we expose a protein to the very intense X-rays from LCLS (or any other XFEL). Within the first moment of interaction from the light and the proteins, the protein scatters photons distinctive to its shape that we are able to measure and hence recover the shape of the protein. But the protein will also absorb the light and therefore energy and will become very hot, much like the conditions on the surface of the sun. The hot protein will expand quickly and disintegrate into its atomic components. While

¹Measurement on Google maps from the injector building to the far experimental hall.

²The European XFEL in Hamburg, Germany is currently build to similar engineering requirements.

³On a fun note, the accelerator part of LCLS is actually older than the I-280 and do avoid interruptions of the experiments, the bridge was built long before the interstate and there are pictures of this bridge that is not connected to any streets.

the scattering process is desired the inevitable absorption process will ultimately hinder the scattering process and limit the resolution of our measurement. The damage that occurs to the sample is an ultra-fast process that can only be studied with an even faster light pulse. It is a process that thus far is known to exist but has been hidden due to the limitation of other light sources. XFEL offer now the opportunity to study this process that is applicable to a variety of X-ray imaging techniques ranging from crystallography to spectroscopic applications over to the imaging of single particles.

This thesis discusses an experiment performed with LCLS to study the effects and dynamics induced by radiation damage on homogenous xenon and helium clusters and heterogeneous clusters consistent of xenon and helium. A detailed and time-resolved X-ray pump – X-ray probe study is undertaken to first induce X-ray related dynamics via a X-ray pump pulse and then create a single-shot image of the cluster at a given time delay. We combine the single particle imaging technique with a time-of-flight mass spectrometer that yields insights into ionization dynamics, absorbed energies and particle heterogeneity. Rare gas clusters are used as sample target as they are an ideal nanosamples in the gas phase. They are easy to produce and easy to transport to the interaction region with LCLS. Furthermore they can be tuned in size and multiple rare gases, here xenon and helium, can be combined to form a single nanometer sized heterogeneous cluster. We present the data from the study in form of real space images from clusters complemented by diffraction images. Furthermore, we correlate the time-of-flight data to each image.

The thesis is organized as follows, chapter 2 discusses fundamental aspects and background information to the performed studies. Chapter 3 focuses on the experimental setup of this study, chapter 5 presents the results obtained and finally 6 summarises the previous chapters and provides an outlook for further studies.

2 Fundamental Concepts

This chapter tries to condense the theoretic concepts that will reoccur throughout the present thesis. We start off in section 2.1 with an introduction to the key aspects of X-ray free electron lasers (XFEL) including the beam operating modes self-amplified spontaneous emission (SASE), self-seeding and X-ray pump – X-ray probe. Section 2.2 is about the formation of rare gas clusters via supersonic jets and pickup sources. We then dive into the interaction of light and matter in section 2.3 that discusses coherent, elastic X-ray scattering, and inelastic processes in atoms. The chapter ends with section 2.4 describing the nanoplasma formation in pristine cluster and core-shell systems.

2.1 Why X-ray free electron laser?

X-rays were first created through *Bremsstrahlung*, where an electron beam with kinetic energies E_{kin} of 100eV - 100keV hit a block of copper and the deceleration of electrons in the copper led to the creation of X-rays. Since then, there has been tremendous progress in the creation of X-rays and are commonly created in synchrotron facilities for scientific purposes. In a synchrotron facility, electrons are accelerated near the speed of light $E_{\text{kin}} > \text{MeV}$ and then injected into a storage ring. The electrons are deflected at bending magnets to circle around the ring. The acceleration at the bending magnet leads to the emission of X-rays. Typically, electrons are bunched together to increase the amount of emitted photons and a synchrotron can store many electron bunches, thus a high repetition rate of light pulses on the order of megahertz. The X-ray pulses are characterized through the so called spectral brightness [6] or sometimes brilliance. We can define the spectral brightness as [7]

$$B = \frac{n}{A \Theta \Delta E}, \quad (2.1)$$

with n being the number of photons per second, A the source area, Θ the divergence of the beam, and ΔE 0.1% of the spectral bandwidth of the light pulse. The spectral brightness is an overall measure of the quality of a light source. The development of modern synchrotron light sources is hence often measured and compared to previous achieved

2 Fundamental Concepts



Figure 2.1: Aerial view of the Linac Coherent Light Source (LCLS). LCLS uses the last third of the SLAC Linear Accelerator but is overall a 4.1km long machine. The accelerator and buildings are stretched far because of the process light is generated. From [8]

B values. The motivation to improve the spectral brightness is to let a sample interact with as many photons possible, in the shortest time as possible and with an energy resolution as best as possible. In other words, more brilliant light sources are needed to create images of even smaller particles, or investigate dynamics that are even faster. To give a numerical example and to get a better understanding of the improvements needed, let us look at non-linear absorption dynamics in atoms and molecules. One can conservatively estimate that a typical absorption cross section at soft X-rays¹ is around $\sigma = 1 \text{ megabarn (Mb)}$ [9]. Typical X-ray focii are² $A = 1\mu\text{m}^2$ such that the number of photons n_{in} needed to absorb just 1 photon per atom n_{abs} is

$$n_{in} = \frac{n_{abs}A}{\sigma} = \frac{10^{-8}\text{cm}^2}{10^{-18}\text{cm}^2} = 10^{10} \quad \text{photons.} \quad (2.2)$$

An example of a modern synchrotron source is NSLS-II and it produces 1.710^4 photons per pulse in the Si111 bandwidth at pulse durations of a few ten picoseconds [10]. That is far out of reach to investigate non-linear, or multi-photon, processes. While this back on the envelope type of calculation might be off by an order of magnitude or so depending on the specific case, it illustrates the order of magnitude improvement scientists were looking for to unravel entire new aspects of nature. As it is not possible to use conventional optical methods to control X-rays, a progressive United States defense program in the 80's ignited an atomic bomb to create an X-ray beam that was intended

¹X-rays with wavelengths of 10nm to 0.2nm.

²Focus size at the AMO endstation at LCLS.

2.1 Why X-ray free electron laser?

for use as anti-(space)missile defense [11]. In a similar time, it was also proposed to build free electron laser [12, 13] to increase the spectral brightness. Free electron laser, amplify the light along a straight line to create optical laser alike radiation and a FEL can be seen in birds eye view in figure 2.1. Construction of the first hard X-ray finished in 2009 and the FEL is called Linac Coherent Light Source (LCLS). X-ray free-electron lasers (XFEL) are able to create 10^{12} photons per pulse and achieve pulse lengths of a few femtoseconds and allow the study of ultrafast processes, for example the movement of electrons in chemical reactions [14, 15]. The beam parameters of FEL increased the spectral brightness by many orders of magnitudes³ and we will explore this topic in detail in the next few subsections. Few XFEL exist today, LCLS at SLAC National Accelerator Laboratory in the United States, SACLAC at RIKEN in Japan but more are being build. The European XFEL near DESY⁴ in Germany, the SwissFEL at Paul Scherrer Institut and the PAL-XFEL at Pohang Accelerator Laboratory in South Korea.

2.1.1 From bending magnets to undulator

In synchrotron lightsources as well as free electron lasers, X-rays are generated using (bending) magnets. The first improvement to creating X-rays at a bending magnet was through a *wiggler*. Wigglers consist of magnets that are arranged in an alternating order to force the electron bunch on a sinusoidal trajectory. An electron bunch that is traveling through a wiggler near the speed of light is wiggled along its path using magnetic fields, which causes the particles to emit radiation. Wigglers can be considered as a series of bending magnets, which is why the total emitted power $P_{emitted}$ is proportional to the number of magnets m [17]

$$P_{emitted} \propto m, \quad \text{in a wiggler magnet.} \quad (2.3)$$

The emitted radiation has a broad, continuous spectrum and the center of that spectrum can be controlled by changing the speed or kinetic energy of the electron bunch. Wigglers have been used at the Stanford Synchrotron Radiation Lightsource (SSRL) in 1979 to generate X-rays. Independently from wigglers, undulators were developed [18]. A schematic setup of an undulator can be seen in figure 2.2. Wigglers and undulators create radiation because of the same principle, an electron bunch is accelerated near the speed of light and then forced on a sinusoidal pathway. In undulators, the separation of magnets is named undulator period λ_U . The undulator period and magnetic fields

³See figure 2.5 for an illustration of the improvement in brilliance.

⁴abbreviation for Deutsches Elektron Synchrotron

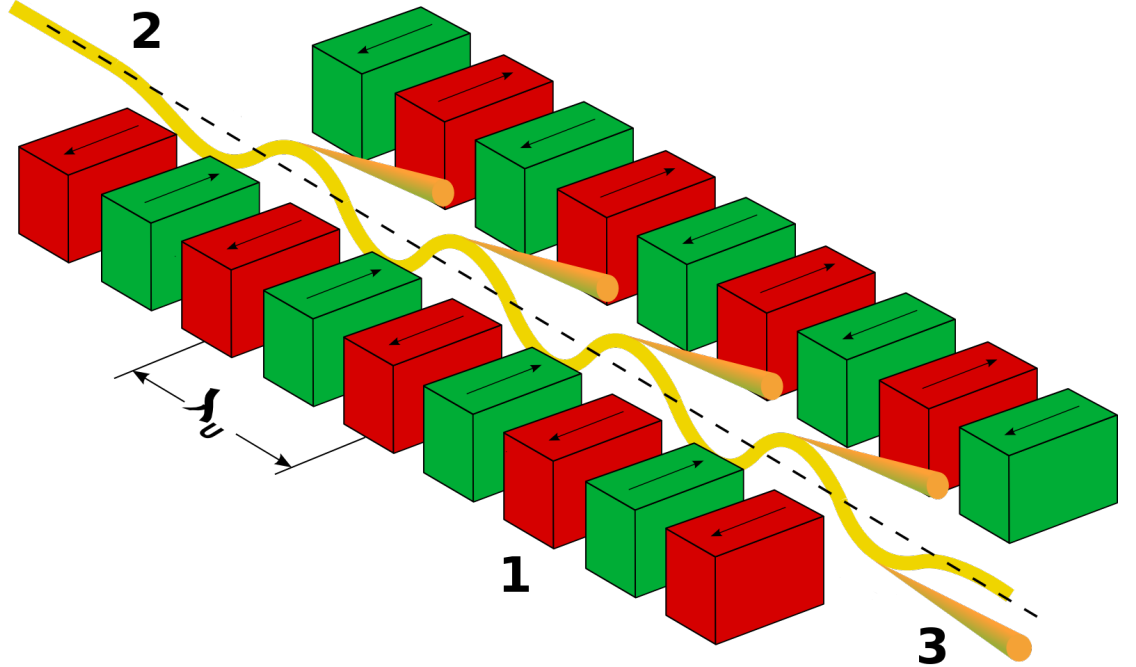


Figure 2.2: Schematic setup of an undulator with a period of λ_U . (1) Magnets in alternating polarity; the arrows indicate the direction of the magnetic field. (2) Incoming electron bunch near the speed of light. (3) Emitted light in beam direction due to sinusoidal movement of the electron bunch. From [16].

are chosen such that the emitted radiation per period constructively interferes with each other. Thus the emitted power P_W now scales with [19]

$$P_{\text{emitted}} \propto m^2, \quad \text{in an undulator magnet} \quad (2.4)$$

The emitted wavelengths of undulators have a more narrow spectrum and a higher flux than wigglers. We can further characterize undulator (and wiggler) by the strength parameter K , which is given by [20]

$$K = \frac{e B_{\max} \lambda_U}{2\pi m_e c}, \quad (2.5)$$

2.1 Why X-ray free electron laser?

with e being the elementary charge, B_{\max} being the maximum magnetic field in the undulator (wiggler), m_e being the mass of an electron and c being the speed of light, we can write in convenient units

$$K \approx 0.934 B_{\max} \lambda_U \quad [\text{T cm}] . \quad (2.6)$$

Undulator typically have $K < 1 \text{ Tcm}$ (and wiggler $K \gg 1 \text{ Tcm}$). Undulator magnets are large constructs of a few meters and their undulator period is on the order of centimeter. The electrons emit radiation in the nanometer wavelength regime because the electrons near the speed of light have to be considered relativistic and in view of the electrons the undulator period λ_U appears shorter. We can account for the relativistic effects and express the resonantly amplified wavelength λ_r by [20]

$$\lambda_r = \frac{\lambda_U}{2\gamma} \left(1 + \frac{K^2}{2} + \gamma^2 \Psi^2 \right) , \quad (2.7)$$

with the kinetic energy γ of the electron bunch in the undulator and the electrons observation angle Ψ . Summarizing, modern lightsources use undulators to generate radiation as these magnets create more photons that have a narrow spectral bandwidth compared to bending magnets and wiggler. Undulators are characterized by the strength parameter given in equation 2.6, which is only dependent on the undulator gap λ_U and the magnetic field B . The fundamental amplified wavelength is given by the resonance condition equation 2.7.

2.1.2 Self amplification by spontaneous emission

If an electron bunch travels through just one undulator, the emitted power scales with linearly with the number of electrons N_e , which is due to the finite size and random electron density distribution of an electron bunch. If the electrons emit light from the same point or separated by $n \lambda_r$ ($n = \{1, 2, 3, \dots\}$) the emitted photons would constructively interfere and would be coherent. FEL use this idea to generate their light pulses. FEL have a straight and long undulator section⁵, where multiple undulators are connected in series. As the electron bunch travels through the FEL undulator section, microscopic effects play a role that could be neglected in typical synchrotron radiation sources. In vacuum, light will always be faster than electrons near the speed of light. This slight velocity difference means that the co-propagating photons and electrons have a phase

⁵LCLS has a 112m long undulator section.

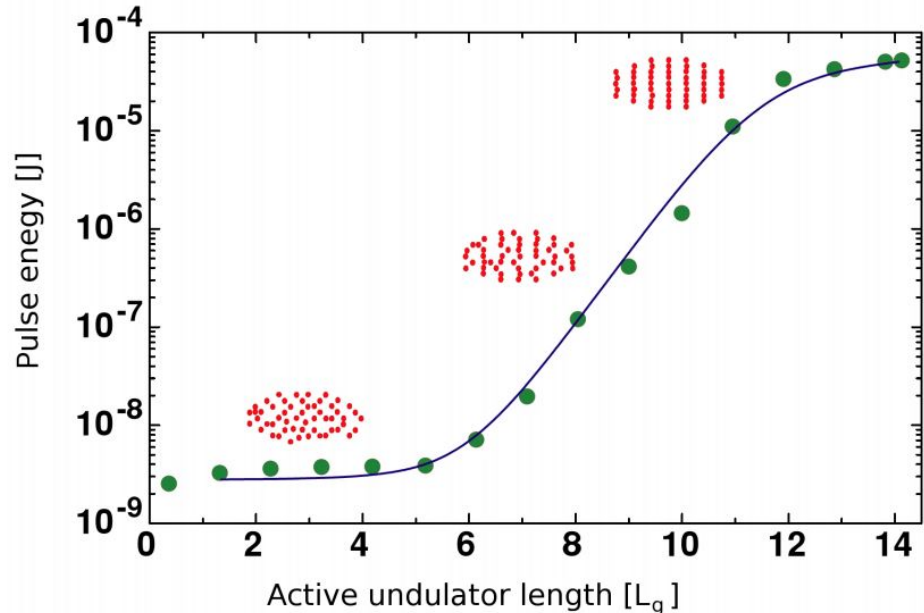


Figure 2.3: Undulator gain curve correlated to microbunching. The X-ray pulse energy is plotted algorithmically over the undulator length L_g (blue curve, green dots) and shows an exponential growth until saturation. The electron bunch (red dots) starts with a random density distribution, as the bunch travels through the undulator modulates the electron density and the electrons are microbunched. Upon optimal microbunching, the X-ray lasing process saturates. From [21, 22]

2.1 Why X-ray free electron laser?

difference and interact with each other. Depending on the phase, an electron will either gain or loose velocity. Over each undulator period, we can describe this *slippage* with $\lambda_r(\Psi = 0)$. As a result, the initial uniform electron density is periodically modulated. The modulated electron bunch structure is called *microbunching*. The creation of microbunching as it travels through undulators is illustrated in figure 2.3. The increasingly structured electron beam amplifies a more narrow wavelength bandwidth and the number of electrons that are in phase with the photons increases over the travel length through the undulator. The lasing process saturates when the microbunching is fully developed. Initially (random) created photons in the undulator define the microbunching as it travels through the undulators and amplifies these photons through subsequent spontaneous emission. Hence, this type of radiation (or FEL operation mode) is called *Self Amplification by Spontaneous Emission* (SASE). SASE achieves laser alike amplification of the radiation power P_{SASE} scales [see 7, p. 61]

$$P_{\text{SASE}} \propto N_e^2, \quad \text{SASE operation} \quad (2.8)$$

SASE spectra can be seen in figure 2.4. A SASE spectrum is different from shot-to-shot and has distinct peaks that are defined by the initial photons on top of a more broad background. The electrons interact with the light field because of their narrow spatial and kinetic energy distributions that define the so called *emittance* of an electron bunch. Only the linear accelerator of FEL are able to compress an electron bunch in space and energy, i.e. create a low emittance electron bunch, such that it can interact with the photons and microbunch. Since the creation of X-rays affects the kinetic energy of the electron bunch γ and the lack of optics, XFEL use one (compressed) electron bunch⁶ in a long set of undulators to create one light pulse. This is also called a *single-pass high-gain* FEL. Without going into much detail, optics can be used to build *multi-pass low-gain* FEL that are able to reuse electron bunches [24], which leads to higher repetition rates and more narrow spectrum but fewer photons per pulse.

2.1.3 Soft X-ray self seeding

Another FEL beam mode is the seeded type. In contrast to the SASE operation, where the initial photons are randomly emitted and further amplified, a seeded FEL starts with a given *seed* of photons. If the set of initial photons is monochromatic, mostly this wavelength is amplified as the bunch travel through the undulator. The initial photon seed

⁶the European XFEL uses a so called bunch train, where multiple electron bunches are accelerated in series.

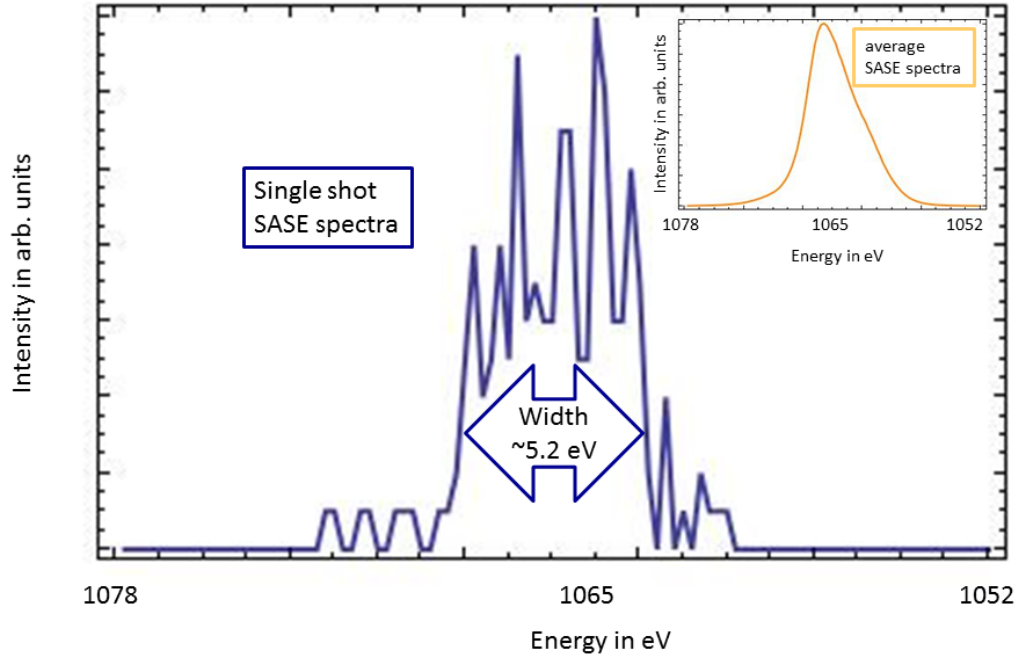


Figure 2.4: Spectra of FEL SASE operation. The large blue spectra is a SASE spectra from a single FEL shot using a photoelectron spectrometer as described in [23]. Note the spiky peak structure on a background pedestal. Within the narrow bandwidth of a FEL pulse some energies are getting more strongly amplified due to the microbunching. The yellow graph in the inset is an average spectrum of several hundred single-shots and has a low energy tail, which is due to FEL-jitter.

2.1 Why X-ray free electron laser?

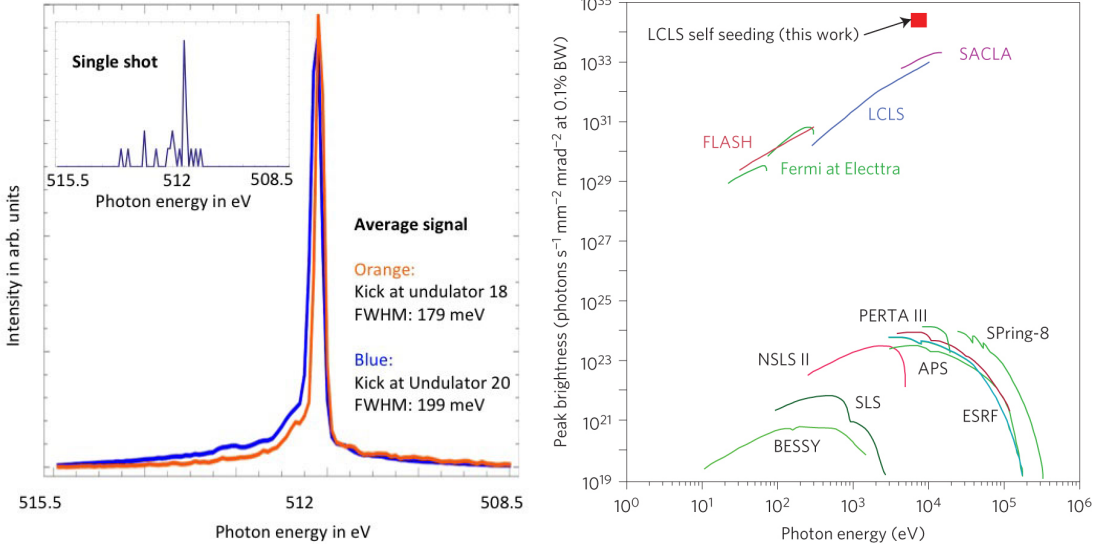


Figure 2.5: Left, normalized average spectra of soft X-ray self-seeding operations using the SXRSS and AMO instrument at LCLS [23]. The self-seeding spectra is characterized by a sharp spectral peak around a desired energy accompanied by a SASE radiation type spectral pedestal. The often undesired SASE pedestal is suppressed, when the electron bunch travel through undulators is shortened, here kick at LCLS undulator 18 vs. 20. The right image shows the peak spectral brightness of various light sources over a wide photon energy range. Soft X-ray self-seeding has a spectral brightness that exceeds current SASE FEL sources. From [25].

2 Fundamental Concepts

can be created through various processes and the wavelength of the photon seed is the critical parameter in determining which method to choose. For example, in the infra red (IR) to extreme ultra violet (XUV) regime, conventional lasers can be used to place the initial photons seed. However, due to the lack of lasers available at X-rays wavelength regimes, the idea of *self-seeding* gained traction. In self-seeding, an electron bunch is first send through a few undulator magnets to generate a few SASE photons, the electrons and photons are then separated using a magnetic chicane, which also neutralizes the microbunching in the electron bunch. The monochromator selects a small wavelength slice from the comparably broad SASE spectrum of the initial photons. Photons exiting the monochromator are considered as *seed*. The seed and the electron bunch are overlapped again using the magnetic chicane and then send through more undulators. Here, the seed modulates the electron bunch and thus only a narrow spectral band is amplified. A typical spectrum of a soft X-ray self-seeded beam can be seen in the left figure 2.5. The characteristics of a self-seeded spectrum are an intense peak at the selected wavelength regime on top of a broad SASE background pedestal. The background is an artifact of the amplification of some spontaneous emission events and can be suppressed by using fewer undulator magnets. Self-seeded beams have a significantly reduced pulse energy by an order of magnitude, depending on the exact beam parameters, as compared to SASE operations. However, in their main peak, self-seeded beams have a higher spectral brightness when compared to a SASE spectrum. Using equation 2.1 the increase in spectral brightness compared to SASE is understandable and it is illustrated in the right figure 2.5. Self-seeded beam operations have recently been demonstrated at LCLS. At hard X-rays, the Hard X-Ray Self-Seeding (HXRSS) instrument uses a diamond crystal to select a wavelength slice [26]. At soft X-rays, the Soft X-ray Self Seeding (SX RSS) instrument uses a grating as dispersive element [27]. A seeded beam using an external laser generate photons as initial seed has been demonstrated at the extreme ultra violet (XUV) FEL FERMI at Ellettra-Sincrotrone in Italy [28]. The peak intensity in a narrow spectral band makes seeded beams interesting for a variety of applications particular in condensed matter physics, where it is instrumental to excite with narrow bandwidth photons. Of course there are also applications in atomic and molecular physics, ranging from linear absorption spectroscopy [29], to ultrafast photoemission spectroscopy on molecules [23], to non-linear stimulated Raman spectroscopy [30], to ultra-fast photoemission studies. Particular interesting for this work is the magnetic chicane from the SX RSS instrument that has been used as described in the next chapter.

2.1.4 Novel X-ray pump–probe techniques

In order to study X-ray induced phenomenon using X-ray imaging and spectroscopy techniques, as it is discussed in the present work, two X-ray pulses are needed . Here, a pump pulse is used to induce dynamics in the sample system and a probe pulse is used to probe them at a certain time delay Δt . Pump–probe experiments are commonly used as they allow a precise study of dynamics. The pump pulse gives a very controllable starting point, i.e. time zero in the dynamic process, and the probe pulse can perform a measurement at a later time delay Δt . Sometimes pump and probe pulse are switched, which is indicated by a negative time delay Δt , often to verify time zero or to probe the system before any dynamics have occurred.

Creating two X-ray flashes to create a pump–probe experiment is a technical challenge and again this challenge is due to the lack of X-ray optics. In order to overcome this challenge, two methods have been proposed. Method one, mirror based beam-split and delay systems [31, 32] that split one pulse into a pump and probe beam and allow the delay of the latter. These systems are typically limited to short times delays, as the optics have to fit into existing setups and have a low transmission of X-rays over the mirrors. Method two, uses accelerator based schemes [33, 34] that manipulate electron bunches to create two X-ray pulses. Limitations arise depending on the scheme, e.g. limited pulse delay Δt or pulse energy split through limited electron beam separation or length of magnetic chicane. Both methods have been demonstrated at LCLS and have found use to complement the more widely available optical laser pump – X-ray probe methods particularly in the chemical sciences [35–37].

Another aspect to pump–probe experiments is the tunability of wavelengths in each pulses, for example to resonantly pump and off-resonance probe or vice versa. Equation (2.7) indicates which parameters can be tuned to create two pulses of different color. One, the undulator parameter K can be tuned to change the emitted wavelength, or two, the lorentz factor γ can be different if there are two electron bunches. A potential third option are variable gap undulators that allow a change of period λ_U . At LCLS λ_U is fixed but future upgrade plans for LCLS-II include variable gap undulators [38]. As the accelerator based X-ray pump – X-ray probe method, let us describe these schemes in greater detail.

Undulator parameters $K_{1,2}$ based pump–probe scheme

The first developed accelerator based pump–probe technique at LCLS [33] uses a difference in undulator parameters $K_{1,2}$ to create two pulses of different wavelength, the time

2 Fundamental Concepts

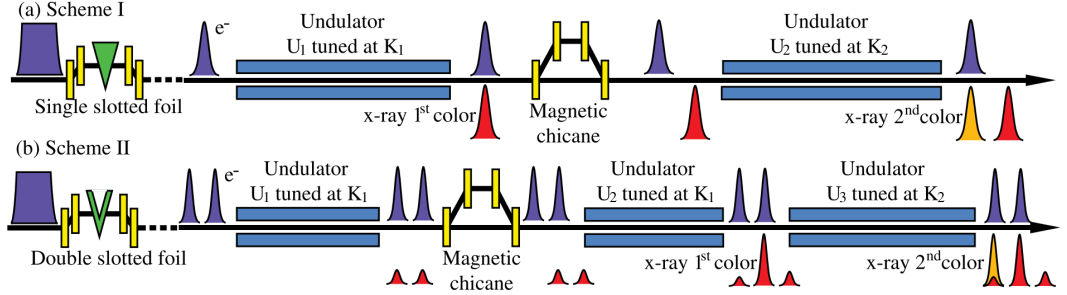


Figure 2.6: Schematic setup at LCLS of undulator parameter K_i based pump–probe schemes. Scheme I creates one electron bunch using a single slotted foil and scheme II creates two electron bunches using a double slotted foil. The electron bunches emit radiation with a wavelength depending on K_i . A time delay Δt between pulses is introduced using a magnetic chicane. From [33]. Reprinted with permission from APS.

delay is introduced through a magnetic chicane and a schematic setup can be found in figure 2.6.

Following the figure, in scheme I, one electron bunch is created through a single slotted foil⁷ The use of the slotted foil enables control over the pulse duration. The electron bunch then travels through an undulator section U_1 tuned at strength parameter K_1 and is stimulated to lase but the process does not go into saturation such that the electron bunch can be reused in the second undulator section. A magnetic chicane removes the microbunching from section U_1 such that in undulator section U_2 , tuned to undulator strength parameter K_2 , the electron bunch lases again and the process is able to saturate. The maximal color separation between the two pulses is 1.9% in relative difference between K_1 and K_2 .

The time delay Δt between the two pulses is introduced by a magnetic chicane. At LCLS, a dedicated chicane, e.g. from the soft X-ray self-seeding instrument, can reach up to

$$\Delta t_{\max} = 800 \text{ fs}. \quad (2.9)$$

The minimal time delay can be achieved by setting the deflection in the magnetic chicane to zero in which case

$$\Delta t_{\text{drift}} = \frac{l}{v_{\text{el drift}}} - \frac{l}{c} \approx 0 \text{ fs}, \quad (2.10)$$

⁷A single slotted foil or emittance-spoiling foil works comparable to a monochromator. It leaves a certain energy band of the electron bunch within the slot unspoiled and Coulomb scatters or spoils (compare to apertures) the rest. The ‘dispersive’ element is a magnetic chicane. By narrowing the electron beam one also reduces its pulse duration [39].

2.1 Why X-ray free electron laser?

with $l \approx 4m$ being the length between undulator sections U_1 and U_2 and c being the speed of light and v_{el} drift being the drift velocity of the electron bunch. As the electron bunch travels close to the speed of light t_{\min} is typically on the tens of attosecond timescale. The timing jitter between the two light pulses using only one electron bunch comes from the magnetic chicane due to the magnetic field jitter and the electron beam energy jitter. The total contribution to the timing jitter is less than 0.4% of the time delay Δt imposed by the chicane. Since the delay chicane does not significantly contribute to the delay Δt_{\min} a bigger factor is the velocity mismatch of the light pulse and the electron bunch. This mismatch can be estimated by

$$\Delta t_{\min} - t_{\text{drift}} = \frac{N_u \lambda_r}{c}, \quad (2.11)$$

with N_u being the undulator periods. Given the parameters in study [33], $t_{\min} = 3fs$ such that a partial overlap between the electron bunch and lightpulse could be achieved after the magnetic chicane. It should be noted that this technique has been used in the described experiment.

Scheme II uses a double slotted foil⁸ to create two electron beams. The two beams have a longitudinal separation that translates into the time delay Δt . The electron bunches travel through a first set of undulators U_1 that creates two pulses of the same wavelength, due to the shortness of the section U_1 the lasing process does not saturate. The electron bunches are then delayed using a magnetic chicane such that the leading electron bunch overlaps with the trailing light pulse. This light pulse now functions as a seed for the leading electron bunch such that this pulse saturates in undulator section U_2 . The electron bunches then travel through the magnets at U_3 , where the trailing electron bunch creates a second saturated pulse, the leading electron bunch barely emits radiation in U_3 since its energy spread has become too large after lasing in U_2 . Using this method, two saturated lasing pulses can be generated, however, temporal overlap cannot be achieved.

Twin bunch or Lorentz factor γ based pump–probe scheme

The second developed accelerator-based pump-probe technique at LCLS [34] uses two electron bunches of different energy. A schematic setup of this beam operation can be found in figure 2.7.

The electron bunches are created through a double laser pulse that impinges on a pho-

⁸A double slotted foil works as a single slotted foil but it leaves to parts of the electron beam unspoiled through the two slots.

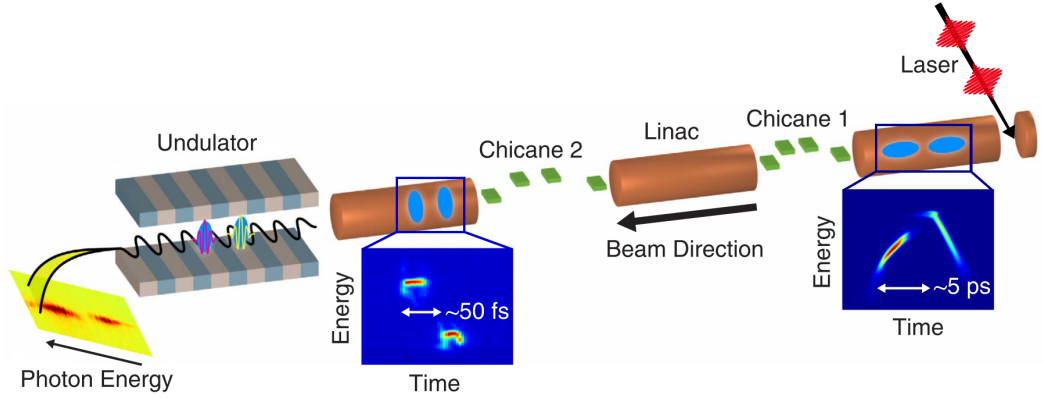


Figure 2.7: Schematic setup of the two bunch, two color pump–probe setup at LCLS. Two laser pulses shot at a cathode create two electron bunches with a delay Δt on the picosecond timescale. Two magnetic chicanes compress the bunches such that a delay Δt on the up to the ten femtosecond timescale is achieved. Both pulses go through one undulator section and the lasing process is saturated. The relative color separation is on the order of 1% between the bunches. From [34, CC0].

tocathode. Initially, these two bunches have a time delay of a few picoseconds, however, two magnetic chicanes compress the electron bunches in the time and intensity domain such that a time delay on the ten femtosecond timescale is achieved. The electron bunches then travel through one undulator section and both pulses saturate in their lasing process. At 8.3k eV, both pulses combined can reach pulse energies of $1.2mJ$, the color separation is 100 eV and the time separation ranges from $\Delta t_{min} = 0fs$ to $\Delta t_{max} = 100fs$. At hard X-rays, this method requires the pump pulse to have a higher photon energy than the probe pulse, although their respective intensities may vary. However, this method is not restricted to hard X-rays and can be utilized at soft X-rays. In the soft X-rays wavelength regime, where the slotted spoiler foil can be used. This allows a further control to tune the time delay of the electron bunches and enables scanning across time zero with both pulses.

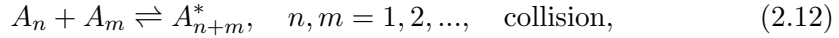
2.2 Rare gas clusters

Clusters have a long history to study light-matter interaction for a few reasons. Their characteristics are well known, they can form interesting states and often it has practical purposes [40]. Generally speaking, clusters are an aggregation of atoms or molecules and

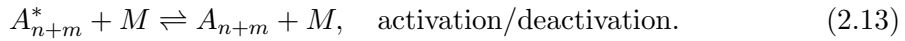
vary in size. Their size ranges from a few atoms to mesoscopic sizes such that one can classify a cluster as a bulk material. Even though clusters can form exotic materials that are interesting to study, they can be simulated with computer models. Besides these testbed characteristics, clusters can be created comparably easily and are tunable in size. Rare gas clusters are a subclass of clusters and they are bound by van der Waals forces, thus are normally neutral-charged. Single van der Waals cluster typically form in an icosahedral⁹ shape when they are sufficiently small (up to nanometer sized) [41] and have mostly a fcc-crystal¹⁰ structure but exhibit also hcp-crystal¹¹ structures [42, 43]. In the present work, superfluid helium cluster (or droplets), solid xenon cluster and a mixture of both have been used as a sample. Therefore, we shall explore the creation of homogenous and heterogeneous rare gas clusters in the next sub-sections.

2.2.1 Creation of a homogenous cluster

Rare gas clusters, for example xenon clusters, can be generated in a variety of ways. Often, as in the described experiment, rare-gas clusters are created by releasing gas from a reservoir into a vacuum. Here, a nozzle connects the gas reservoir with the vacuum system and while the gas is expanding through the nozzle, many collisions take place. So, the cluster formation process can be explained intuitively through a kinetic model [44]. In other words, clusters grow through collisions with monomer, dimer and other clusters. We can express a collision mathematically through the following reaction formula



with n, m denoting the number of monomer assembling body $A_{n,m}$. A body A_n collides with another body A_m and form a metastable state A_{n+m}^* that will dissociate if not a subsequent collision deactivates it



M is a chaperone that can be any kind of third body that removes energy from the system. Note that a chaperone M can also activate the state again. The binding force behind rare-gas clusters is the Van der Waals force, hence these clusters are called Van der Waals cluster sometimes.

⁹An icosahedron is a polyhedron with 20 faces, i.e. a dice with 20 faces.

¹⁰fcc is short for face-centered cubic. A very common crystal structure.

¹¹hcp stands for hexagonal close-packed and is also a crystal structure.

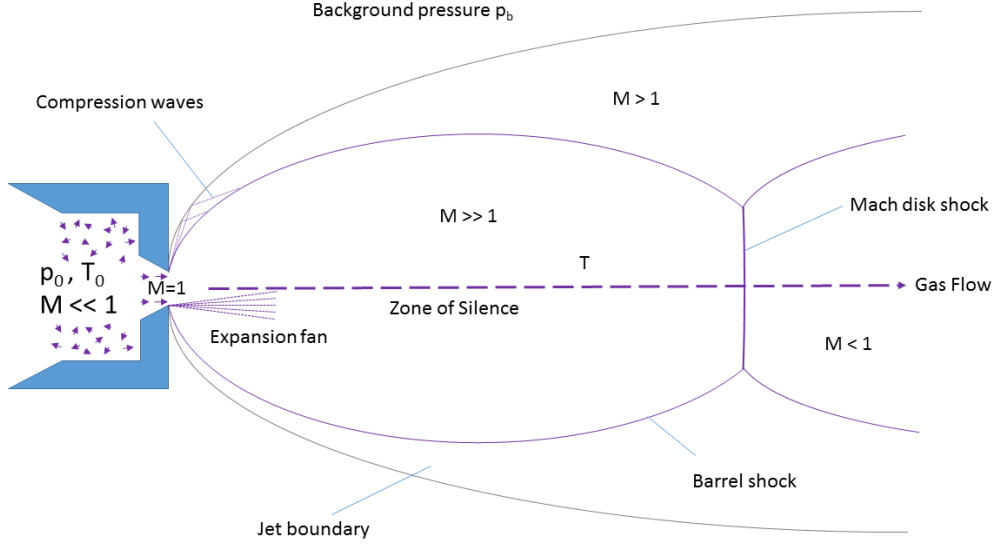


Figure 2.8: Schematic of a supersonic gas expansion into the vacuum. Gas is stored in a reservoir at pressure p_0 , temperature t_0 and speed of the gas is thermal distributed ($M \ll 1$). As the gas enters the nozzle area, it is accelerated to the speed of sound ($M = 1$) and as the gas expands, the temperature T drops altering the speed of sound such that the gas now travels supersonic ($M \gg 1$). In this expansion, clusters are generated in the nozzle region, where $M = 1$ (see text for details). After [47]

While the early stage of the cluster growth is driven by the monomer addition, cluster-cluster coagulation start to dominate the later growth processes [45, 46]. This is due to the quantitative increase in small clusters in the generation process that then start to collide, similar to above kinetic model. From empirical evidence, we know that clusters solely generated through monomer addition have a size distribution of an exponential decay, whereas larger clusters that grew through coagulation follow a log-normal distribution. So through coagulation, the density of smaller clusters (and monomers and dimers) decreases because of the cluster-cluster coagulation and larger clusters are formed. The most probable size of a cluster, i.e. the maximum of the log-normal distribution, is given by the parameters of the (supersonic) gas expansion, which is what we will discuss next.

Supersonic jet setups typically store gas in a reservoir at a certain stagnation pressure p_0 and temperature T_0 . The gas expands through a nozzle into a vacuum and figure 2.8 shows a schematic drawing of this process. Typical values for p_0 are 10 bars, where the mean free path of the atoms is much smaller than the nozzle diameter D . This is why

many collisions occur during the expansion in the nozzle and the above described kinetic theory explains the cluster formation. However, this holds not true in the supersonic molecular flow region, where no further cluster growth happens. To understand the expansion process in detail, we assume to work with an ideal gas and to describe the gas expansion itself, we further assume that no clusters are formed and that turbulence and effects of heat conduction are unimportant [40, 48].

To begin, the velocity distribution of the gas is thermally distributed at a set temperature T_0 . The movement direction of each atom is randomly orientated. For an ideal gas, we can define the enthalpy H_0 in the stagnation chamber

$$H_0 = c_p T_0, \quad (2.14)$$

with the specific heat c_p for atoms

$$c_p = \frac{5}{2} k_B, \quad (2.15)$$

where is the Boltzman constant k_B . The expansion of the gas through the nozzle is driven by the pressure difference p_{vac}/p_0 . In the nozzle, the (steady) gas flow becomes directed and the enthalpy H_0 is converted into kinetic energy $\frac{1}{2}mv^2$ and a rest enthalpy H . So, in the expansion process, we can use the conservation of energy, and equation (2.15) we can write down

$$H_0 = H + \frac{1}{2}m_{gas}v^2 = c_p T + \frac{1}{2}m_{gas}v^2, \quad (2.16)$$

with T being the local temperature along the gas flow and m_{gas} the atomic mass of the gas. To look at this in greater detail, let us define the Mach number M as the ratio of the stream velocity v and the local speed of sound c_s

$$c_s = \sqrt{\frac{\gamma k_B T}{m_{gas}}}. \quad (2.17)$$

With the ratio of specific heats $\gamma = \frac{c_p}{c_v}$ at constant pressure and volume, they can be regarded as independent of temperature for atomic gases, we can rearrange equation 2.16 to

$$T = T_0 \left(1 + \frac{1}{2}(\gamma - 1)M^2 \right)^{-1}. \quad (2.18)$$

2 Fundamental Concepts

Here the interplay between the Mach number M^2 and the local temperature T give insight into the directed mass flow versus the remaining thermal energy in the system. As indicated in figure 2.8, M increases dramatically along the expansion axis and that is due to decrease in speed of sound c_s that is proportional to \sqrt{T} as indicated in equation (2.17)¹². Finally, this attribute has given the name to supersonic jets.

Let us describe the appearance of the jet stream (see figure 2.8) next. Upon exiting the nozzle, the Mach number increases by a wide margin ($M \gg 1$), that means that the gas travels faster than information in this medium. Here, a *zone of silence* is formed, where the gas flow is not influenced by other particles, thus uninterrupted. As the supersonic flow is exiting the nozzle it has to turn around the edge of the nozzle to further expand and the supersonic flow turns by actually creating smaller Mach waves. At the borders of the *zone of silence*, M decreases drastically resulting in dense regions that are called *barrel shock* to the sides and *Mach disk* downstream the gas flow. For an unhindered transport of the gas and clusters to the interaction region, the interaction region needs to be within the *zone of silence*. We can express the distance from the nozzle to the Mach disk x_{MD} through

$$\frac{x_{MD}}{d} = 0.67 \sqrt{\frac{p_0}{p_b}}, \quad (2.19)$$

with the nozzle diameter d . So the competing stagnation pressure p_0 and the background pressure p_b define the distance of the otherwise static parameters. p_b needs to be low enough to drive the Mach disk downstream of the interaction region. By using skimmers and thereby physically separating the jet expansion into separately pumped compartments, the background pressure p_b can be reduced, hence x_{MD} increased.

While we have described a cooling gas in the expansion process it should be noted that the clusters are comparably hot. Through the kinetic process described above, they are efficiently heated. The two processes to lose energy are, one, collisions with a chaperone M that deactivates the cluster, or two, evaporation of monomers from the cluster. The evaporation process makes the temperature size-independent, after the clusters have reached a certain minimum size [49]. Typically, the jet reaches temperatures of a few Kelvin and the cluster temperature is heavily dependent on their material, particularly the dissociation energy. For this study relevant are mostly the temperature of Xenon cluster that is 75K¹³ and the fact xenon clusters are solid as their melting temperature

¹²In other words, the gas is expanding and quickly reaches the terminal velocity $v_\infty = \sqrt{\frac{2R}{m_{gas}} \left(\frac{\gamma}{\gamma-1} \right) T_0}$, with R being the universal gas constant, while the speed of sound is decreasing. This can be abused to calculate flight times $t_{\text{flight}} = \frac{d}{v_\infty}$, if the distance d from nozzle to interaction point is known.

¹³To put this temperature in perspective, krypton clusters are 50K and argon cluster 40K [49, 50]. Note that in this study the cluster size was $\bar{N} > 800$, hence above the minimum value to be size

Helium	Neon	Argon	Krypton	Xenon
3.85	185	1646	2980	5554

Table 2.1: Parameter K_{gas} values for rare gases [51].

is higher [50]. For similar reasons, helium clusters are liquid, which is why they are often called (helium-)droplets. If helium droplets are produced using a cryogenic jet even superfluid helium-droplets can be observed.

At the current point of the discussion, it should shine out that the average cluster size is very much depended on the gas type, stagnation temperature T_0 , stagnation pressure p_0 and the nozzle type. Indeed, an empirically found scaling law named after Hagena [52–54], can be written down as

$$\Gamma^* = K_{\text{gas}} \cdot T_0^{0.25q-1.5} \cdot p_0 \cdot d_{eq}^q, \quad (2.20)$$

with the gas specific parameter K_{gas} that can be found in table 2.1 for some rare gases, the gas specific parameter q that varies between 0.5 and 1 and is 0.85 for all rare-gases, and the equivalent nozzle opening d_{eq} that is $d_{eq} = d$ for pinhole sources and for conical nozzles d_{eq} reads

$$d_{eq} = d \frac{\tan(\Phi_0)}{\tan(\Phi)} \quad (2.21)$$

with the half opening angle of the nozzle Φ and the half opening of the free gas expansion Φ_0 . The Hagena scaling parameter Γ^* allows us to estimate the mean cluster size, i.e. amount of accumulated particles per cluster $\langle N \rangle$, as follows

- $\Gamma^* < 350$, no cluster formation observed.
- $350 < \Gamma^* < 1800$, in this region $\langle N \rangle$ reads

$$\langle N \rangle = 38.4 \left(\frac{\Gamma^*}{1000} \right)^{1.64} \quad (2.22)$$

- $1800 < \Gamma^*$, in this region $\langle N \rangle$ reads

$$\langle N \rangle = 33.0 \left(\frac{\Gamma^*}{1000} \right)^{2.35} \quad (2.23)$$

Supersonic jets generally create clusters of different sizes. This size distribution is cen-

independent. For the evaporative cooling process to settle at a given temperature, a certain flight distance (in the cited study 6.5cm) should also be taken into account.

2 Fundamental Concepts

tered around $< N >$ and for solid rare gas clusters this distribution is a log-normal distribution. The size distribution can be an experimental challenge, especially when size dependent effects are investigated. Historically, electron diffraction [49, 55] has been used to determine the mean cluster size, mean temperature and mean geometry. Today, free electron laser allow the determination of the size of a single cluster through a diffraction image and by measuring enough single clusters, one can reproduce size distributions of a supersonic jet as shown in figure 5.1.

Experiments using supersonic jets for cluster generation are typically performed with pulsed valves to decrease cost and gas load in the overall system. Upon opening and closing of the valve, the gas density varies. This mostly affects the cluster size and one would expect to see smaller clusters. This remains true in the beginning of the pulse but in the *afterpulse* one finds giant clusters that exceed the above described scaling laws due to the effects when closing the valve [56].

2.2.2 Creation of a heterogeneous cluster

A possibilities to create heterogeneous clusters is through the principle of picking-up atoms or molecules [40, 57]. Figure 2.9 illustrates pickup regions that are typically used in an experiment. Mainly, there are two different pickup places, one, monomers are added to the cluster in region A of figure 2.9 that represents the nozzle of a supersonic source, or two, they can be picked up by a cluster in region B for example through an increased background pressure p_{b2} with the dopant material. If clusters pick up atoms or molecules in the nozzle region A, they can become part of the cluster formation and can be found inside of solid clusters. If atoms or molecules are picked up in region B, they stick to the surface of solid clusters. If a (super-)liquid cluster picks up a dopant, it may move within the droplet. Since the traversing cluster is much larger and heavier than a colliding monomer the trajectory is not affected significantly. Already pressures of $p_{b2} = 10^{-11}$ bars over a pickup length of a few centimeters can dope the cluster in significant form. At these low pressures, picking up atoms or molecules in region B requires less gas load on the system but is also less efficient than picking up in region B. To increase the pickup levels in region B, a gas cell can be used as much higher pressures can be achieved within the gas cell without putting too much gas-load on the overall system.

The collision with the cluster and a dopant does add energy to the cluster just as the cluster growth process itself. This is why the initial cluster will loose particles through evaporation upon pick up of a dopant [58]. The loss of particles through evaporative cooling is dependent on the ratio of dissociation energies of the two materials and can

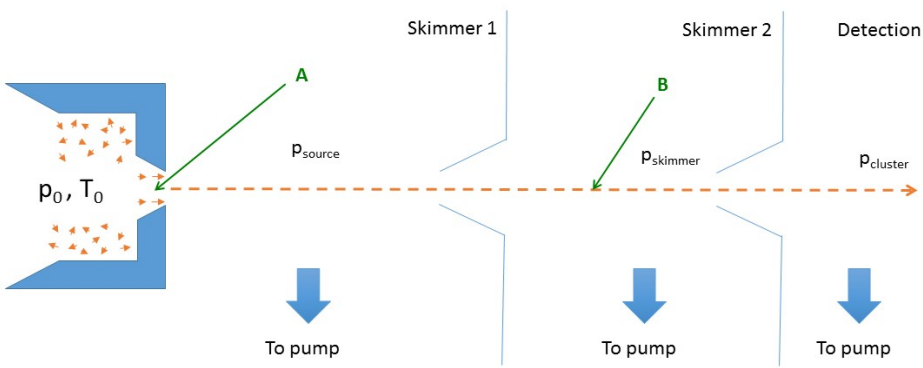


Figure 2.9: Schematic setup to generate heterogeneous clusters through pickup. Thereby is a first cluster generated via a supersonic gas expansion, which is doped at regions marked A or B. In region A, the dopant gas is mixed in the nozzle such that it becomes part of the nucleus. In region B, the cluster condenses atoms on its surface and commonly gas cells are used to regulate the pressure p_{skimmer} effectively. p_{source} is the pressure in the source chamber. The cluster can be detected upon evaporation, i.e. by contact with the chamber, through the pressure p_{cluster} and the cluster doping can be determined through partial pressures (see text for details). After [40, 57].

2 Fundamental Concepts

be written down as

$$N_{\text{Evaporated from cluster}} \approx \frac{\epsilon_{\text{cluster}}}{\epsilon_{\text{dopant}}}, \quad (2.24)$$

with the dissociation energy of the cluster $\epsilon_{\text{cluster}}$ and of the dopant ϵ_{dopant} . In the case, where a helium droplet is doped with xenon atoms, we may use the dissociation energies of helium $\epsilon_{He} = 0.6 \cdot 10^{-3}$ eV and xenon $\epsilon_{Xe} = 0.6 \cdot 10^{-3}$ eV [58, 59], such that approximately 250 helium atoms evaporate by picking up 1 xenon atom.

We can extend this idea to estimate the amount of picked-up atoms, if we were to know the amount of atoms in the cluster before and after the pickup area. An estimate of the initial cluster size $\langle N_{\text{cluster}} \rangle$ can be reached through the scaling laws¹⁴ as discussed in section 2.2.1. A measure to estimate the cluster size after the pickup can be established through measuring the partial pressure of the cluster material p_{cluster} of helium¹⁵, when the particle jet hits a wall and evaporates (see figure 2.9). The partial pressure p_{cluster} then scales linearly with the initial cluster size $\langle N_{\text{cluster}} \rangle$, such that

$$\langle N_{\text{dopant}} \rangle \approx \frac{\epsilon_{\text{cluster}}}{\epsilon_{\text{dopant}}} \cdot \frac{\Delta p_{\text{cluster}} \langle N_{\text{cluster}} \rangle}{p_{\text{cluster}}}, \quad (2.25)$$

where $\Delta p_{\text{cluster}}$ denotes the partial pressure difference with pickup and without.

2.3 Light-matter interaction

A full description of light-matter interaction is mathematically challenging and not the purpose of this thesis. In the following subsections, we will break down the light-matter interaction into its components. The components of the interaction of photons with matter can be split into five categories, 1) coherent-elastic scattering (see sub-section 2.3.1), 2) inelastic processes (absorption, see sub-section 2.3.2), 3) incoherent scattering (Compton effect) and high-energy physics effects of 4) pair production and 5) absorption effects with the nucleus. As it already shines through, the effects are dependent on the wavelength and the cross-sections for 3-5 can be neglected in the soft X-ray regime. We will therefore concentrate the discussion on points 1-2 and restrict ourselves to the for the experiment necessary theory.

¹⁴As already established the actual cluster size produced with a supersonic jet will vary, hence the average cluster size $\langle N_{\text{cluster}} \rangle$.

¹⁵For example with a residual gas analyzer.

2.3.1 Small angle X-ray scattering

We can describe a linear polarized, electric field of a continuous electromagnetic wave via the following expression [7]

$$\vec{E}(\vec{r}, t) = \vec{\epsilon} E_0 e^{i\vec{k} \cdot \vec{r}}, \quad (2.26)$$

with $\vec{E}(\vec{r}, t)$ being the electromagnetic field of the wave, the wave vector \vec{k} , the Cartesian coordinate vector \vec{r} , the complex amplitude if the electric field is then $E_0 \exp^{i\vec{k} \cdot \vec{r}}$ and because of the polarization we use $\vec{\epsilon}$ such that $\vec{\epsilon} \cdot \vec{k} = \vec{k} \cdot \vec{E} = \vec{k} \cdot \vec{H} = 0$. Through a relative comparison, of the incoming intensity I_0 and the scattered intensity I_{sc} , we can phenomenologically establish the differential cross-section over a certain solid angle $\Delta\Omega$ as

$$\left(\frac{d\sigma}{d\Omega} \right) = \frac{(\text{Number of X-rays scattered per second into } \Delta\Omega)}{(\text{Incident flux}) (\Delta\Omega)} = \frac{I_{sc}}{(I_0/A_0) \Delta\Omega}, \quad (2.27)$$

with A_0 being the covered area of the incident beam. If an electro-magnetic wave encounters an electron, we can describe the scattering semi-classical by imagining how an electron starts to oscillate once it sees an incoming electric wave. The electron then functions as a dipole antenna eventually radiating the wave into a certain solid angle $\Delta\Omega$. Depending on the polarization of the incident beam we can reduce equation 2.27 to [7]

$$\left(\frac{d\sigma}{d\Omega} \right) = r_0^2 P, \quad (2.28)$$

with the classical electron radius $r_0 = 2.82 \cdot 10^{-5} \text{ Å}$ and the polarization factor P

$$P = \begin{cases} 1 & \text{vertical scattering plane,} \\ \cos^2(\Psi) & \text{horizontal scattering plane,} \\ \frac{1}{2}(1 + \cos^2(\Psi)) & \text{unpolarized source.} \end{cases} \quad (2.29)$$

We can now move on and use this knowledge for atoms, where we have Z electrons. To describe electrons in an atom, let us proceed by introducing the electron density $\rho_e(\vec{r})$ that describes the probability density of electrons in an atom. Figure 2.10 illustrates the scattering process in one atom. An incident beam with wave number \vec{k} is elastically scattered at a point \vec{r} into a wave with \vec{k}' such that $|\vec{k}| = |\vec{k}'|$. In this wave picture, the scattering process must be seen as a superposition of waves and it is particular illustrated how the wave scattered at the origin of the atom is scattered as well. As both

2 Fundamental Concepts

waves are scattered at different points, they have an optical path difference 2δ . This difference in path length results in a phase difference to each other and eventually leads to interference between the waves. So, we can describe the phase difference $\Delta\Phi(\vec{r})$ of the waves scattered at \vec{r} and the origin by

$$\Delta\Phi(\vec{r}) = (\vec{k} - \vec{k}') \cdot \vec{r} = \vec{Q} \cdot \vec{r}, \quad (2.30)$$

with \vec{Q} being denoted as the *wave vector transfer*. Through trigonometry, we can establish the more common denotation of the wave-vector \vec{Q}

$$\vec{Q} = 2 |\vec{k}| \sin\left(\frac{\Theta}{2}\right) = \frac{4\pi}{\lambda} \sin\left(\frac{\Theta}{2}\right), \quad (2.31)$$

with the wavelength of the light λ and the scattering angle Θ .

A volume element $d\vec{r}$ at \vec{r} will now scatter depending on its electron density, namely by $-r_0\rho(\vec{r})d\vec{r}$. At scattering angle $\Theta = 0$, i.e. $\vec{Q} = 0$ the atomic scattering factor f^0 is

$$f^0(\vec{Q} \rightarrow 0) = Z, \quad (2.32)$$

because all scatterer are in phase. As we increase the scattering angle Θ , the phase difference $\Delta\Phi(\vec{r})$ leads to interference, which we can describe by multiplying a phase factor $e^{i\vec{Q}\cdot\vec{r}}$ to the electron density $-r_0\rho(\vec{r})d\vec{r}$. In the limit of $\vec{Q} \rightarrow \infty$, the atomic scattering factor then is $f^0(\vec{Q} \rightarrow \infty) = 0$. We can integrate over the total scattering length, and write down

$$-r_0 f^0(\vec{Q}) = -r_0 \int \rho_e(\vec{r}) e^{i\vec{Q}\cdot\vec{r}} d\vec{r}. \quad (2.33)$$

This important result is called the atomic scattering factor in units of $-r_0$ and it can be understood as a Fourier transform of the electron density of an atom. We can also remember from optics the light scatter of an object can be inverse Fourier transformed and projects an image of the object again.

Let us continue with the scattering of a molecule or cluster that consist of multiple atoms. We can label the atoms in such an object by

$$F^{object}(\vec{Q}) = \sum_j f_j^O(\vec{Q}) e^{i\vec{Q}\cdot\vec{r}}, \quad (2.34)$$

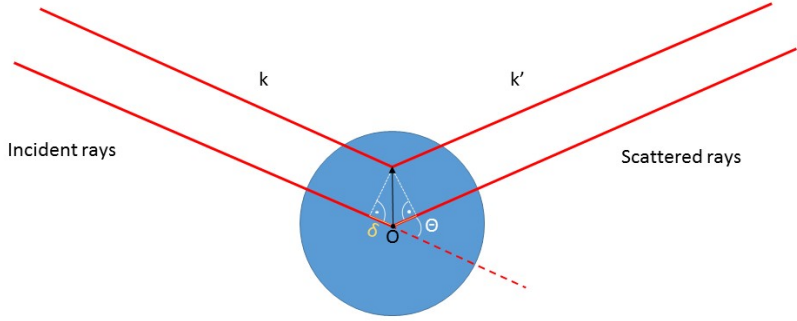


Figure 2.10: Principle of scattering rays of an atom. After [7, 60].

with the atomic scattering factors $f_j^0(\vec{Q})$ for the j 'th atom and call $-r_0 F^{object}$ the scattering length of the object. Strictly speaking and as defined in (2.34), $F^{object}(\vec{Q})$ and $f_j^Q(\vec{Q})$ is \vec{Q} depended. As this is inconvenient, let us consider the following evidence in order to neglect this dependency. In the angular range of \vec{Q} , where $F^{Object}(\vec{Q})$ is not 0, f_j^Q can be considered constant [see 60, p. 6-7]. In human hemoglobin, the range in which the molecule scattering length $F^{Object}(\vec{Q})$ is not 0, the carbon atomic form factors change less than 0.4%. Neglecting this \vec{Q} dependency in f_j^Q allows us to describe the scattering length of extended objects $F^{Object}(\vec{Q})$ via one continuous electron density $\rho_e(\vec{r})$, where certain volume elements $d\vec{r}$ scatter proportional to their electron density $\rho_e(\vec{r})$. Let us write down the more convinient expression for the scattering length of an object

$$-r_0 F^O = -r_0 \int \rho(\vec{r}) e^{i\vec{Q}\cdot\vec{r}} d\vec{r}, \quad (2.35)$$

and we can see that it is mostly the phase factor that yields information about the structure of the object as it is the phase factor that constitutes the diffraction pattern.

2 Fundamental Concepts

The total scattered intensity $I(\vec{Q})$ in a diffraction pattern can be expressed through

$$I(\vec{Q}) = |A|^2 = I_0 \left| F^0(\vec{Q}) \right|^2, \quad (2.36)$$

where an incident beam with intensity I_0 with a complex amplitude A performs an operation that can be interpreted as a Fourier transform of the objects electron density. The process of measuring the scattered light, for example through a detector, merely measures the modulo of an amplitude $|A|^2$, which eliminates the phase factor $e^{i\Delta\Phi(\vec{r})}$. $e^{-i\Delta\Phi(\vec{r})} = 1$. In order to reconstruct the object that scattered in realspace, e.g. to understand its shape or to study its function, we need to recover the most important phase information. We will discuss iterative algorithms that can recover phase information in section 4.5.

Let us briefly address the scattering of a rare-gas cluster, as the cluster can be considered as a spherical symmetric object. That allows to express the electron density of a cluster with radius R as

$$\rho(\vec{r}) = \begin{cases} 1 & \text{for } R \geq \vec{r} \geq 0, \\ 0 & \text{for } R > \vec{r}. \end{cases} \quad (2.37)$$

Using equation (2.37), we can solve the integral in equation (2.35) by transforming into spherical coordinates

$$F_{\text{Sphere}}^O(\vec{Q}) = \int_0^\pi \int_0^{2\pi} \int_0^R r^2 \sin(\Theta) e^{i\vec{Q} \cdot \vec{r}} dr d\Theta d\Phi \quad (2.38)$$

$$= \frac{\sin(\vec{Q}R) - \vec{Q}R \cos(\vec{Q}R)}{\vec{Q}^3 R^3} = \frac{J_1(\vec{Q}R)}{\vec{Q}R}, \quad (2.39)$$

with J_1 being the Bessel function of first kind. Formula (2.39) can be easily abused to determine the size of a spherical particle using local minima in the diffraction pattern¹⁶ or through a numerical fit of the resulting curve.

2.3.2 Ionization of matter

Let us quickly remember the atomic scattering factor $f^0(\vec{Q})$ that were introduced in the last section by neglecting a variety of (wavelength depended) effects through Fourier

¹⁶Equation (2.39) can be solved numerically for the distance between the first two minima, where $\Delta\vec{Q}R = 3.24$, such that $R = \frac{3.24}{\vec{Q}_{\min n+1} - \vec{Q}_{\min n}}$

transforming the electron density of an atom. As we established, we can compare the photon-electron interaction to the analogue of the forced harmonic oscillator, where an electric field drives a (bound) electron. However, it is not only the light field that drives the electron, also the electron has an effect to the light field. As the wave propagates through a medium, the phase velocity of light v_{phase} is slower than the speed of light in vacuum c due to interacting with electrons. We can describe this effect via the refractive index $n \equiv c/v_{\text{phase}}$. Another aspect to consider is a reduction of the amplitude of the incoming electro-magnetic wave (absorption), when the energy of the photons is higher than the binding energies of electrons [7, 61]. These two effects are connected to the atomic scattering factors $f^0(\vec{Q})$ and are called dispersion corrections. Let us include these corrections to the atomic scattering factor and define the atomic form factor

$$f(\vec{Q}, \hbar\omega) = f^0(Q) + f'(\hbar\omega) + i f''(\hbar\omega), \quad (2.40)$$

where $f'(\hbar\omega)$ corrects for the phase velocity and the wave amplitude correction/absorption $f''(\hbar\omega)$. In the limit of high photon energies $\hbar\omega$, bound electrons can be largely seen as free, as the binding energies become a little factor, therefore $f'(\hbar\omega) \rightarrow 0$ and $f''(\hbar\omega) \rightarrow 0$. As the photon energies $\hbar\omega$ are closer to the atomic level, which is the case at soft X-rays for many materials, $f'(\hbar\omega)$ and $f''(\hbar\omega)$ can become large factors.

We shall not derive this topic in its full extend as it can be found in [see 61, p. 55ff], but we shall qualitatively compare the equation for the complex refractive index $n(\omega)$ to forced harmonic oscillator. For simplicity, we reduce the following considerations to the case of forward scattering, where $\vec{Q} = \Theta = 0$.

Let us start by imagining a electromagnetic wave propagating in a medium. The wave propagating in a medium along the axis z can be written as

$$e^{inkz} = \underbrace{e^{i(1-\delta)kz}}_{\text{phase shift absorption}} \underbrace{e^{-\beta z}}_{\text{absorption}}, \quad (2.41)$$

where n is the complex refractive index, δ the real dispersion correction resulting in a phase shift of the wave and β being the imaginary dispersion correction resulting in a decline in amplitude of the wave¹⁷. The relation between the complex refractive index n , β and δ is explicitly given by

$$n \equiv \frac{c}{v_{\text{phase}}} = 1 - \delta + i\beta. \quad (2.42)$$

¹⁷We jump between wave and particle picture as it pleases us. Here, a decline in amplitude in the wave picture can be read as absorption in the particle picture.

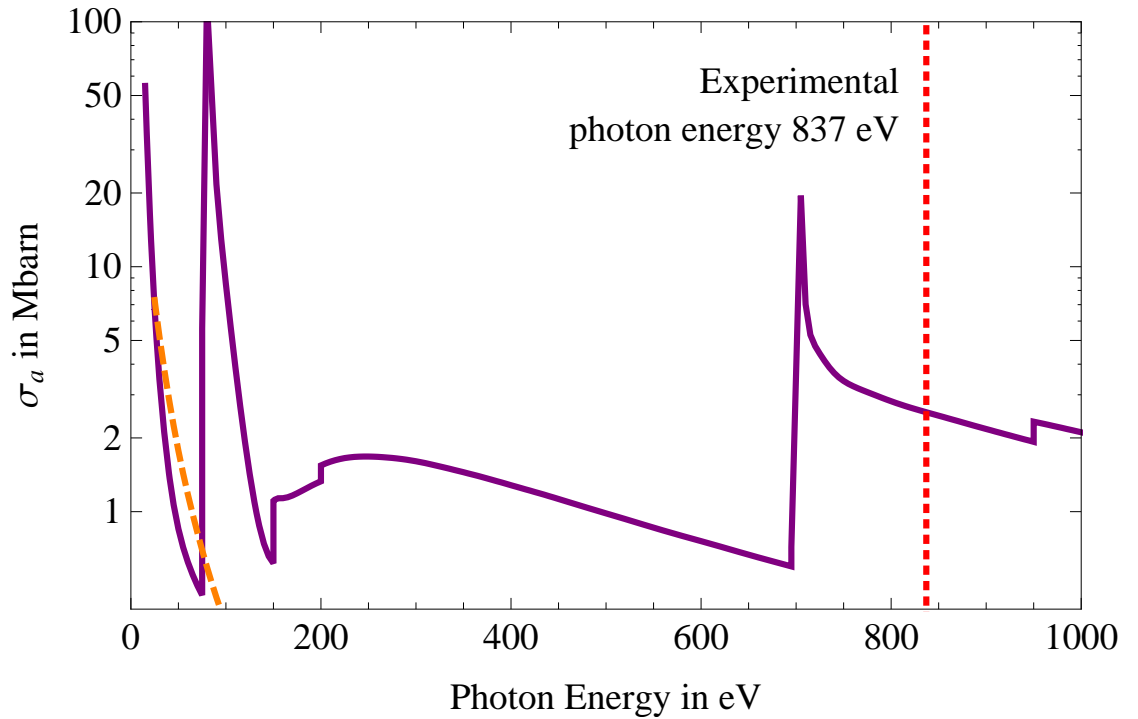


Figure 2.11: Total absorption crosssections σ_a in megabarn for xenon and helium. The purple curve represents the total cross-section of xenon. The orange dashed curve represents the total cross-section of helium. The red dashed line represents the photon energy used at the experiment described in the present work. Data points from [62–64]

We can compare this equation (2.42) to equation (2.40) and realize that we are allowed to define this dispersion relation through the atomic form factor as [see 7, p. 76]

$$n \equiv 1 - \frac{2\pi\rho_{atom}r_0}{k^2} \left(f^0(\vec{Q}=0) + f'(\hbar\omega) + if''(\hbar\omega) \right), \quad (2.43)$$

with the atomic number density ρ_{atom} and we identify

$$\delta = \frac{2\pi\rho_{atom}r_0}{k^2} \left(f^0(\vec{Q}=0) + f'(\hbar\omega) \right), \quad \text{and} \quad (2.44)$$

$$\beta = - \left(\frac{2\pi\rho_{atom}r_0}{k^2} \right) f''(\hbar\omega). \quad (2.45)$$

We have already established in equation (2.41) that β reduces the amplitude of the incoming wave through absorption. Using this insight about absorption, we can rewrite equation (2.45) and define $f''(\hbar\omega)$ in terms of being proportional to an absorption cross section σ_a , which reads

$$f''(\hbar\omega) = - \left(\frac{k}{4\pi r_0} \right) \sigma_a. \quad (2.46)$$

Figure 2.11 shows the total absorption cross-sections σ_a for xenon, helium at which a bound electron absorbs a photon and excited into the continuum, thus the atom is ionized. To get a better understanding of the fundamental absorption related details about xenon and helium, table 2.2 and 2.3 show the differential photo-absorption cross sections and ionization potentials for various energy levels and ionization configurations at the photon energy 837 eV. The calculations were performed with the Los Alamos Atomic Physics code based on [65]. It appears that certain energy levels, or here subshells if one disregards the hyperfine structure¹⁸, tend to have a higher absorption cross-section than others. This brings us back to the picture of the forced harmonic oscillator, where an electron is driven by a light field. If the frequency of the light field is close to the eigenfrequency of the bound electron, in other words, if the energy of a photon is close to the energy level of a bound electron, the system is in resonance and absorption is highly likely. As the photon energy and electron level energy differ, the system is off resonance and it is less likely to absorb a photon. As energy levels in atoms are discrete, electrons can only be excited from one energy level to another or need a certain (minimal) ionization energy to ionize an atom and excite an electron into the continuum. Therefore, the likelihood of a core-electron that is strongly bound being ionized is by far the most probable using X-rays. When a core electron gets ionized, the electronic structure changes and particular ionization energies and (absorption) cross-sections change. To

¹⁸A shift in energy levels due to interaction of electrons with the nucleus [see 66, p 166 ff.].

Shell	Subshell	Cross-section in Mb	subshell ionization potential in eV
K	1s	-	34630.0
L	2s	-	5466.4
	2p	-	4899.1
M	3s	-	1153.3
	3p	-	965.4
	3d	2.2505	682.7
N	4s	0.0305	223.7
	4p	0.1247	161.8
	4d	0.2587	68.2
O	5s	0.0040	27.3
	5p	0.0120	12.5

Table 2.2: Differential absorption cross-sections and ionization potentials for certain electronic configurations of xenon at 837eV. Calculations based on [65].

El. Configuration, and ionized subshell	Ionization of subshell	Cross-section σ_a in Mbarn	subshell ionization potential in eV
$\text{He}^{+0}, 1s2$	1s2	0.0007	24.4
$\text{He}^{+1}, 1s1$	1s1	0.0005	54.4
$\text{Xe}^{+0}, 5p6$	3d10	2.2505	682.7
$\text{Xe}^{+1}, 3d9$	3d9	2.1487	733.6
$\text{Xe}^{+1}, 5p5$	3d10	2.2443	693.7
$\text{Xe}^{+2}, 5p4$	3d10	2.2390	705.9

Table 2.3: Absorption cross-sections σ_a and ionization potentials for certain electronic configurations, including certain ionization profiles. Calculations based on [65].

El. Configuration, and ionized subshell	Scattering factor f^0 in barn
He^{+0} , 1s2	2.5539
He^{+1} , 1s1	0.649465
Xe^{+0} , 5p6	1874.36
Xe^{+1} , 3d9	1813.56
Xe^{+1} , 5p5	1814.68
Xe^{+2} , 5p4	1754.08

Table 2.4: Atomic scattering factor f^0 for certain electron configurations. Calculations based on equation (2.33). From [67]

discuss the parameters that are most applicable to this thesis, a comparison of the most probable transition at the photon energy 837eV is given for helium and xenon in table 2.3. The ionization energies change drastically, whether a core electron or a less tight bound electron is ionized. As per absorption cross-sections, helium can be considered transparent and xenon atoms have a much larger absorption cross-section. The amount of ionization configurations can become rather complex and the table shall give the reader merely a broad understanding of some likely configurations.

The total atomic scattering factors f^0 for neutral and ionized, helium and xenon can be found in table 2.4. It is interesting to see that although a xenon atom has only 27 times more electrons than a helium atom the scattering factor f^0 of neutral xenon is over 900 times stronger than helium. Upon ionization, the absolute changes in f^0 of helium are therefore smaller compared to xenon. The relative change in helium of f^0 after one electron is ionized is 75%, thus (ionized) helium barely scatters. As xenon has multiple occupied subshells, the scattering factors of different ionized subshells are shown in table 2.4. As discussed, it is most likely to ionize the xenon 3d subshell, however, within a few femtoseconds subsequent relaxation processes¹⁹ lead to different ionization configurations, for example a double ionized 5p subshell. For the scattering factor, there is little change whether the 3d or 5p subshell becomes ionized and the change in f^0 is only 0.05%. As xenon has 54 electrons, the relative change upon ionization of one electron in f^0 is only 3%. Xenon is therefore a much stronger scatterer than helium and xenon still scatters well upon ionization of inner or outer shell electrons. In the experiment described in the following chapters, the photon energy is explicitly chosen to have a comparably high absorption cross-section for xenon but is off absorption resonance, a comparably low absorption cross-section for helium and a wavelength short enough to

¹⁹See the following section 2.3.3.

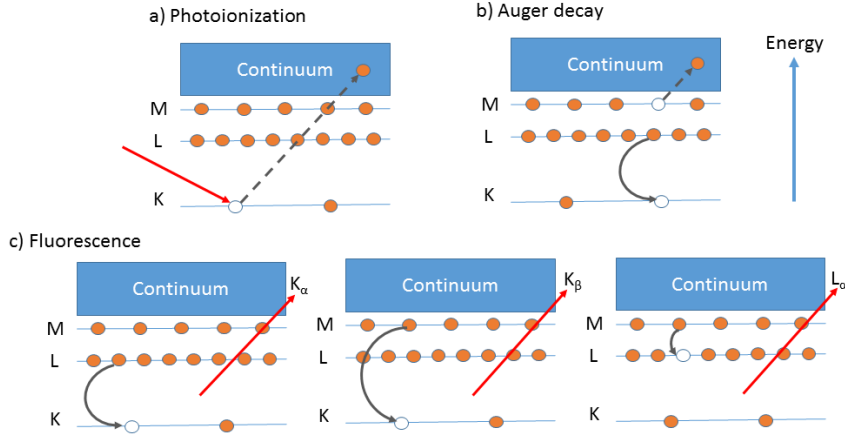


Figure 2.12: Schematic illustration of common charge transfer processes. a) describes a direct emission of an K-shell electron after absorbing a X-ray photon. Process b) shows a secondary relaxation process called Auger decay, where a K-shell hole is filled with an electron from the L-shell and the remaining energy is released through emission of an electron in an outer shell, here M-shell, into the continuum. Process c) illustrates fluorescence, where an electron hole is filled with an electron from an outer shell and the remaining energy is released through photons. Process a) has a distinct spectra depending on the ionized element and the wavelength of the absorbed photon, the released particles in b-c) show an element specific spectra. After [7, p. 19]

receive high resolution images through coherent diffraction imaging. In such a setting xenon is most likely to absorb X-rays and helium can be considered as transparent. Furthermore, xenon acts as the strong scatterer and we are most interested in how the scattering changes when xenon and helium cluster are in a combined environment.

2.3.3 Charge migration

After an atom has been (core-)ionized due to absorption of a photon as depicted in figure 2.12a, the atom is not in its most energetically favorable state. In order to emit energy and transition into its new ground state, the atom can emit particles according to the schematics in figure 2.12b-c. In a fluorescence decay (2.12c), the electron hole in

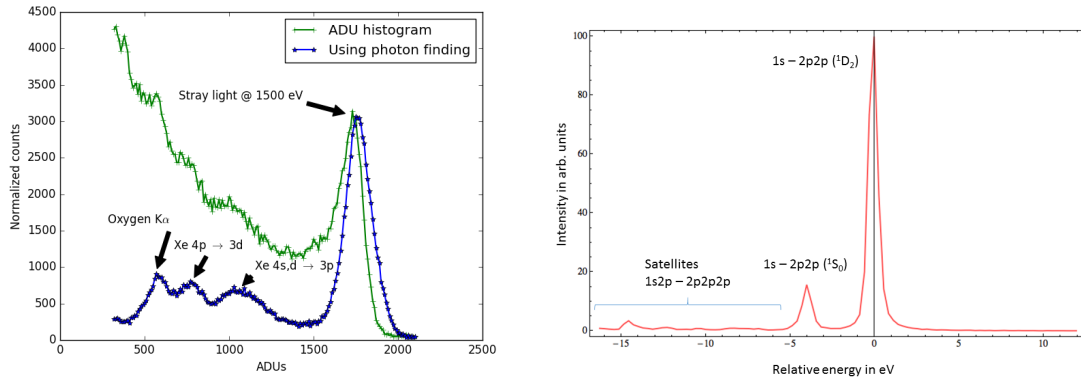


Figure 2.13: Left spectra shows fluorescence peaks from xenon and oxygen illuminated with 1.5keV photons from the LCLS and detected with pnCCD detectors [68, 69]. The green curve is a ADU histogram of the pnCCD detector and the blue curve uses a coalescent photon finder as described in section 4.2. Right, selection of the K-LL Auger spectrum with rel. energy 0 corresponding to 804.5eV. The ionization starts in the K shell, i.e. a 1s hole, and the Auger relaxation process ends up with two holes, e.g. in the L-shell denoted as LL or 2p2p. As electrons energy levels arrange due to their quantum numbers, multiple peaks appear for similar hole configurations, e.g. 2p2p [23, 70].

the (K-)shell is filled by an electron in an energetically higher shell, here L or M shell, and thereby emits a photon of the discrete energy difference between the transitioning levels. If one spectrally resolves the discrete peaks are element specific and modern photoemission spectroscopy can yield insight into for example element identification, excitation dynamics or chemical bonds. Figure 2.13 left shows measured fluorescence lines of oxygen and xenon. In this measurement, xenon atoms and residual oxygen atoms have been illuminated with 1500 eV photons from the Linac Coherent Light Source and the fluorescence photons have been measured with the LAMP pnCCD detectors that are described in section 3.4. The green curve is a ADU histogram of the pixel-detector using the detector calibrations described in section 4.2. The blue curve additionally uses a photon-finding algorithm as the signal from just one fluorescence photon splits up into multiple pixel. The coalescent-photon finding algorithm looks for pixel above a certain threshold and includes neighboring pixel above a certain threshold, thus correcting the measured signal to yield a proper ADU count per photon.

The Auger decay is another possibility for the atom to emit absorbed energy is through a 2-step process. First, an outer shell electron is emitted into the continuum, the so

2 Fundamental Concepts

called Auger-electron²⁰. Secondly, simultaneously to the first process another electron fills the electron-hole. An Auger decay occurs typically on the few femtosecond timescale [70]. Emitted Auger-electrons have discrete energies depending on the combination of electrons involved in the process. Similar to Fluorescence spectroscopy, one can use this attribute to, for example, identify elements or calibrate energies. Figure 2.13 right shows a partial K-LL²¹ Auger spectrum from neon illuminated by 1050 eV photons from the LCLS and measured with a hemispherical analyzer as described in [23]. In this example, neon is ionized in the K-shell and an electron-hole in 1s is created. An electron from the L-shell fill the 1s hole and another electron from the L-shell, the Auger electron, is emitted into the continuum. As there is a variety of electronic configurations that can be involved in this process multiple peaks appear for similar occupation configurations, e.g. 1s - 2p2p. More complex structures, called satellites, appear when the atom is initially ionized, for example an additional hole in the L-shell and then an absorption that creates a hole in the K-shell will lead to KL-LLL satellites.

Similar to the Auger decay, where electrons from an outer shell are involved in the relaxation process, the transition can also be of the same shell and is then called a Coster-Kronig transition. Relevant transitions are for example the N-NN Coster-Kronig transitions in xenon [71].

So far we have looked at X-ray induced processes from atoms. Extended objects, whether a bio-molecule or a cluster, will respond differently than just the atoms they consist of. Nanometer-sized objects will develop a distinct character due to their electronic bond with other particles. This includes rare-gas clusters that are weakly bound Van der Waals forces. We shall explore this behavior in the next section 2.4.

2.4 Ionization of clusters in intense X-ray pulses

Cluster have a long history as a testbed sample to investigate light-matter interaction. The response of a cluster upon irradiation with light often differs from just the atomic response. Collective effects change the microscopic (sample) environment and it is now the collective of atoms that generate a response to the interacting light. Clusters provide therefore a testbed environment to study collective effects ranging from atomic, to molecular and to bulk material attributes. While we went over some benefits of using clusters in section 2.2, it shall also be said that they provide an ideal testbed sample to control light-driven many-particle processes [72]. In this section, we study how rare-gas

²⁰Named after the french physicist Pierre Auger.

²¹This nomenclature means a single hole in the K-shell is followed by a two holes in the L shell after the Auger decay.

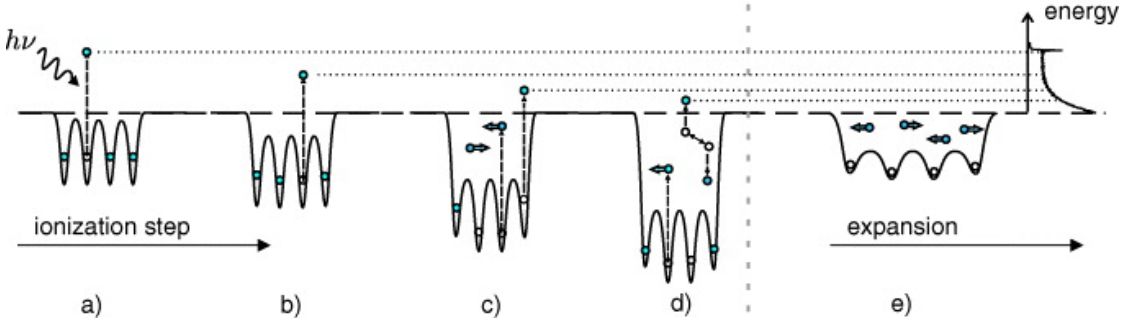


Figure 2.14: Schematic of the nanoplasma creation and expansion. In step a) X-ray photons ionize electrons from a cluster. b) subsequent *multistep ionization* try to relax the electronically excited system, deepening the Coulomb potential of the cluster. Step c) shows a deepened Coulomb potential of the cluster, due to which the multistep ionization becomes (partially) frustrated and electrons are trapped in the potential. In step d) trapped electrons collide and start to thermalize. Collisions can lead to emission of trapped electrons. e) The superheated nanoplasma starts to expand. From [73,]

cluster respond to femtosecond long, high intense X-ray pulses, which is particularly interesting as it allows us to study radiation damage processes, which are similar to the sample damage bio-molecules exhibit upon interaction with (intense) X-ray radiation.

2.4.1 Formation and expansion of a nanoplasma

Let us begin by recapture the elastic, coherent scattering part of the response that has been discussed in sub-section 2.3.1. Equation (2.34) indicates how the scattering length of a cluster can be calculated and, even though we neglect inelastic processes, this response is close to actual measured scattering patterns. If, however, we consider the inelastic effects discussed in section 2.3.2, it should be clear that the elastic scattering length $-r_0 F^{Object}$ is reduced due to the (atomic) dispersion corrections $f'(\omega)$ and $f''(\omega)$ that reduce the scattering length $-r_0 f^0(Q)$ of a single atom. On the one hand, the dominating change in scattering length is driven by the absorption process that we introduced via the imaginary dispersion correction $if''(\omega)$ but we know from table 2.4 that the changes in scattering cross-section are relatively small, on the other hand, there are X-ray induced effects that change the scattering behavior of clusters. We know from previous experiments that these changes are related to the nanoplasma expansion. Let us follow figure 2.14 and [73, 74] in the next five steps. Step a) of the nanoplasma

2 Fundamental Concepts

transition, the cluster gets ionized due to intense radiation²². Step b), further ionization through emission of photo electrons and Auger electrons lead to a so called *multistep ionization* that steepens the Coulomb potential [75–77]. Step c), the multistep ionization is suppressed (or frustrated) because the Coulomb potential depth is larger than the atomic excess energy of photo- and Auger electrons. The emitted electrons are now trapped in the cluster potential and are *quasi-free*. Upon increasing *inner ionization*, the nanometer sized object undergoes a phase transition to a nanoplasma²³. Step d), the temperature of the nanoplasma is initially defined by the atomic excess energies (a rather discrete spectrum) but collisions with other particles lead a (kinetic) energy distribution of the electrons that is similar to thermal distributions and can be measured via the spectra of evaporated electrons [78, 79]. Step e) Hydrodynamic and Coulomb forces drive an expansion of the cluster and the cluster will ultimately disintegrate. The hydrodynamic portion of the force is due to the increasing hot plasma and the resulting increase outward pressure, whereas the Coulomb portion comes from the repelling force of same charges. Both these forces reasonably describe the expansion process, are not mutually exclusive and depend mostly on sample size and irradiation technique. Regarding the sample size, large clusters efficiently trap electrons in their Coulomb potentials such that the quasi-free electrons thermalize and subsequently heat the nucleus. The hot nanoplasma system then tries to expand due to the increase in internal pressure. Electrons thermalize on the attosecond timescale and simulations show that the energy transfer to the ions can be as fast as 50 fs [80]. Small clusters trap photo and Auger electrons less efficiently and electrons are free such that the heating process is suppressed. In the case of small clusters, the ions see the repelling force due to Coulomb interaction of same charges with each other [81].

The nanoplasma expansion is also wavelength dependent. At optical to UV wavelengths strong field ionization can lead to ionization of clusters and a subsequent nanoplasma expansion [82]. At VUV, XUV and soft X-rays, direct photoionization becomes the main driver of the nanoplasma expansion and depending on the wavelength, certain multistep ionization cascades are enabled [73]. It remains to discuss the radiation intensity, which affects the ultimately achieved charge-state combination. The more intense the radiation is, the more energy is absorbed by the cluster. For the nanoplasma expansion, this determines the speed of the nanoplasma phase-transition and the expansion.

²²The wavelength of radiation must be above the ionization threshold of at least one subshell, however, it must not be X-rays with a wavelength on the nanometer length scale.

²³Plasma is another state of matter, similar to solid, liquid and gaseous, where molecular bonds dissociate and positive and negative particles are present in increasing numbers.

2.4.2 Imaging of transient states

The nanoplasma transition is so interesting is because every matter irradiated by a free-electron laser will undergo a nanoplasma transition and finally disintegrate. This is a challenge for structural biology and called radiation damage or sample damage[84]. Sample damage changes the structure of a biomolecule and it is particularly the structure many scientists want to investigate. In order to prevent falsified measurements, one needs to understand the nanoplasma transition as it occurs while the pulse is propagating through the sample. First attempts to perform a combined spectroscopic and imaging technique revealed correlations between the complex refractive index [85] and the diffraction patterns but also correlations of the ion spectroscopic data and the diffraction patterns intensity [86]. More recently, simulations on diffraction patterns could show the expanding electron density [83] as it is also shown in figure 2.15. In this particular study, an infra-red laser was used start (pump) a nanoplasma transition in a xenon cluster and subsequently image (probe) this state with a XFEL pulse. As the time delay between pump and probe pulse is varied, the resulting diffraction patterns of the 15-20 nm Xe-cluster show declining intensities at larger scattering angles with increasing time delay $\Delta t > 100fs$. The loss in signal could be explained through an expanding electron density [87, 88]. The electron density thereby expands increasingly over time due to the Coulomb and Hydrodynamic forces and, first the outer layers expand and at larger time delay also the inner atomic layers. In this study, an electron temperature of 200eV could be measured by comparing plasma simulations to the ion spectroscopy signal. The possible spatial resolution out of the diffraction patterns has been estimated to be 8 nm but through assuming a shape the electron density model is sensitive below this resolution.

In another study with shorter time delays of $\Delta t < 100fs$, xenon cluster compress in size [36]. Since clusters form as a crystal²⁴, one can determine their structure through crystallographic approaches as it is explained in full detail in [7, chapter 5]²⁵. Figure 2.16a is showing Bragg peaks under certain conditions over the scattering vector \vec{Q} . The signal moves to larger scattering vectors \vec{Q} and, as $\vec{Q} = \frac{2\pi}{a}$, the unit cell length a is shrinking over the time delay $\Delta t = \{0, \dots, 100\}$. This unintuitive and contradictory result is attributed to the changes in electronic configuration upon ionization. Electrons

²⁴See section 2.2.1.

²⁵In short, crystals scatter light and create Bragg spots at large \vec{Q} -values. These Bragg spots occur when the so called Bragg-law is fulfilled. Bragg's law reads $m\lambda = 2d\sin(\frac{\Theta}{2})$, with m being an integer, λ being the wavelength of the scattered light, d the distance between crystalline layers and Θ the scattering angle. When Bragg's condition is fulfilled, the rays interfere constructively and the location of the Bragg peaks gives insight to the crystalline structure.

2 Fundamental Concepts

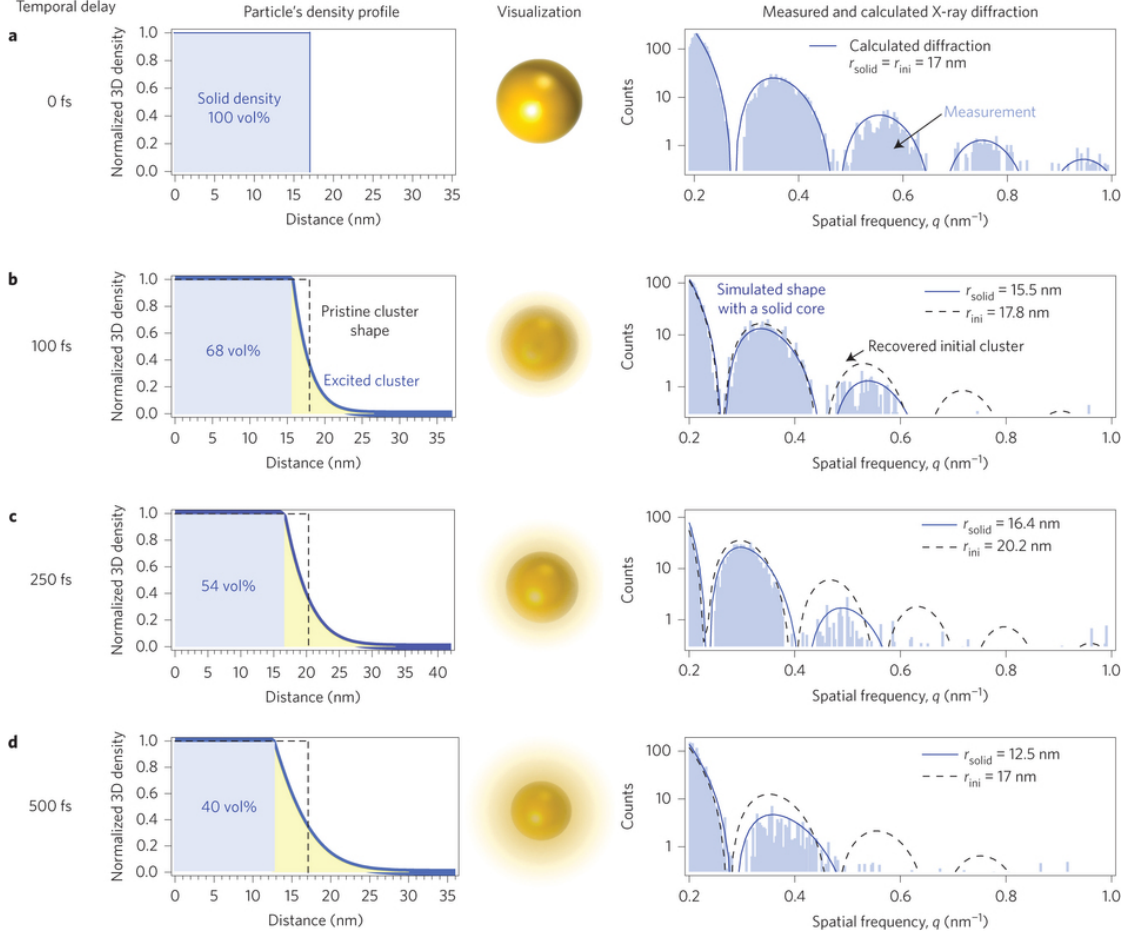


Figure 2.15: Left series, simulation of of diffraction patterns. Right series, measured diffraction patterns of (spherical) xenon clusters pumped with an NIR laser pulse and probed a certain time delay with an LCLS pulse. The diffraction pattern show a decrease in intensity at larger q values, which can be explained through an expanding electron densities, i.e. a nanoplasma expansion. Electron density simulations are performed in 1D and the densities Fourier transform is fitted to the measurement for a solid sphere (dashed line) and an expanding sphere (solid line). From [83]. Reprinted with permission from Nature Publishing Group.

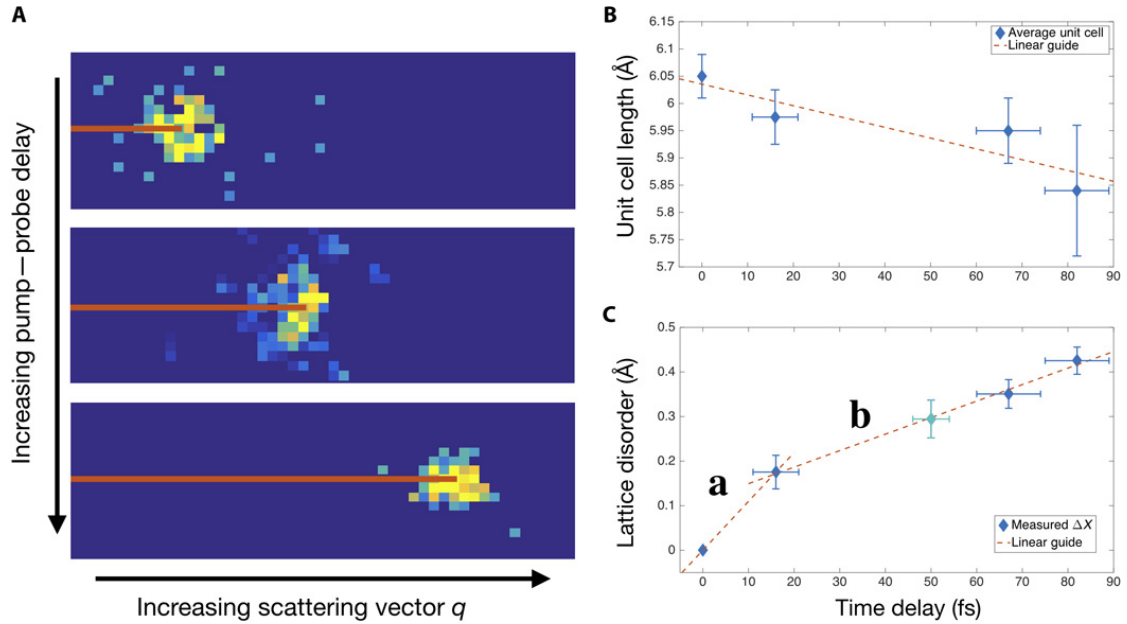


Figure 2.16: X-ray pump – X-ray probe scattering experiment on Xe-cluster that shows an early evolution of the nanoplasma transition. A, single-shot Bragg peaks at varying time delays. The scattering vector q increases over time delay. B, unit cell length over time delay. The unit cell length decreases, therefore the cluster shrinks in size. C, Lattice disorder over time delay. The measured fcc lattice is becoming disordered after being pumped with a X-ray pulse. From [36]. Reprinted with permission from AAAS.

2 Fundamental Concepts

that are trapped in the cluster Coulomb potential have an increased mobility and are able to contribute comparable to valence electrons and therefore change the chemical bonding character of the Van der Waals cluster. As a result, the unit cell changes on the Ångstrom length scale and the lattice becomes increasingly disordered (see figure 2.16c). These two studies allow us to conclude that the nanoplasma transition is a multistep process. First, the initial ionization occurs, followed by an increased Coulomb potential that traps electrons, which then change the structure of the nanosample, e.g. compression of a lattice. Eventually, the system becomes strongly ionized and hot such that Coulomb and hydrodynamic forces start an expansion of the system until eventually the forces disintegrate the sample into its atomic components.

2.4.3 Tampered layers to inhibit the nanoplasma expansion

To overcome radiation damage, the most common method is to *outrun* radiation damage processes using very short pulses [84]. Pulses from the XFEL must be shorter than the lifetime of Auger processes, thus on few femtosecond long, to fully outrun the multistep ionization. However, by limiting the XFEL pulse duration, one inevitably limits the pulse energy as current pulse compression methods typically generate much less fluence. This means that currently, many coherent diffractive imaging experiments are performed with pulse widths of 40fs or more to generate enough scattered intensity. But even if these technical limitations can be overcome, outrunning radiation damage does not circumvent photoionization and it is therefore expected that also few femtosecond long pulses only reach a certain spatial resolution [89]. To be more precise, it is an open question, whether electron densities and here particular bonding configuration are obtainable by solely outrunning radiation damage. As radiation damage is unavoidable it can be mitigated in several ways. As the underlying processes are well understood, one way to mitigate for the radiation damage would be to simulate the effects, however, this can only be done for small particles. Another way to fundamentally increase resolution in single particle imaging is due to prior alignment of particles such that their orientation is known while the image is taken. Molecule alignment has seen some success for small molecules [90] but it is currently unknown, whether this works for larger molecules as the strong light fields, which are needed to align the molecules, may change their structure. Here it should be noted that recent advances with CDI algorithms made it possible to computationally determine the orientation of a particle at the time of imaging [91, 92] without prior knowledge if at least a few hundred diffraction images are provided. Anyway. In this thesis, we shall discuss a method to reduce effects of radiation damage through artificial tampered layers. Artificial shells around a sample supply it with electrons and function as

2.4 Ionization of clusters in intense X-ray pulses

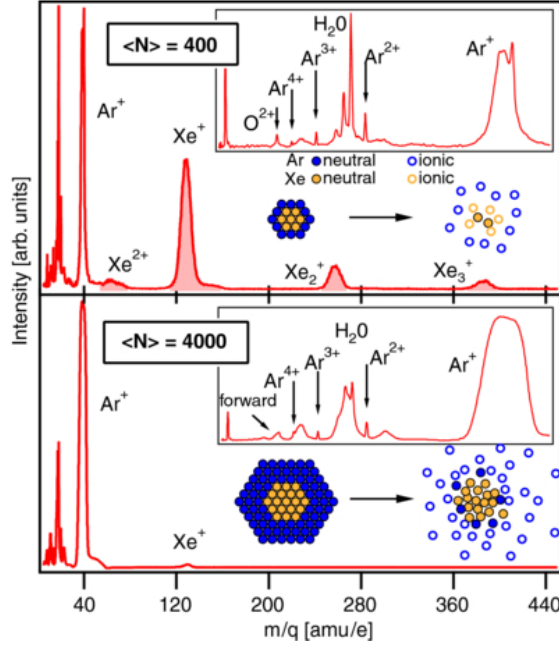


Figure 2.17: Time of flight (TOF) traces of argon and xenon core shell systems irradiated with 93eV X-ray pulses from FLASH. At this energy, mostly Xe is ionized and the ionized atoms create a steep Coulomb potential that traps electrons towards the center of the cluster. The top panel shows smaller clusters with 400 particles, in which the trapping is inefficient, few electron-ion recombinations occur, thus Xe and Ar ions are detected in the TOF detector. The bottom panel shows large clusters with 4000 particles and a thicker argon shell. Here, Xe-ions recombine in the center and the TOF shows mostly Ar ions as the neutral Xe remains undetected. From [94,].

sacrificial layer that protects the sample [93]. For aerosol particles, this method has also only been investigated through ion spectroscopy [94, 95]. In the study shown in figure 2.17 a core-shell system of argon and xenon was constructed and here xenon compares to the sample and argon compares to the sacrificial layer around the particle (see figure). The heterogeneous cluster were irradiated with 93eV photons from *FLASH*²⁶ at which mostly xenon atoms are ionized. As described in the nanoplasma creation process (see section 2.4.1), the increasing ionized cluster creates a steep Coulomb potential trapping electrons. Trapped electrons are available for recombination with the ionized atoms. In the small core-shell system of Ar-Xe with 400 particles (figure 2.17 top-panel), the time of flight mass spectroscopy data shows Xe and Ar ions meaning that the charge

²⁶Short for **F**ree electron **L**ASer in **H**amburg. An extreme ultra violet (XUV) free electron laser in Hamburg, Germany.

2 Fundamental Concepts

recombination is suppressed and the cluster disintegrates upon irradiation. In the large Ar-Xe cluster system with 4000 particles (bottom-panel), mostly Ar ions are in the TOF data meaning the Xe ions in the center of the cluster recombine with the electrons that were attracted to the center by the steep Coulomb potential of the large cluster. The neutral Xe is not detected by the TOF detector. The Ar ions in the outer layers contributed electrons to the center of the cluster due to the attractive potential but were shed off the cluster. It is also evident that the argon atoms in the large cluster case release more kinetic energy than in the small cluster case, which is likely an effect that cools the intact cluster core.

3 Experimental Setup

The experiment described in the present thesis has been performed using the LAMP end-station in the Atomic, Optical and Molecular Physics instrument of the Linac Coherent Light Source, which is located at SLAC National Accelerator Laboratory. SLAC National Accelerator Laboratory (SLAC) is funded by the Department of Energy (DOE) and operated by Stanford University. SLAC was founded in 1962 as Stanford Linear Accelerator Center. The accelerator was mainly used for high-energy physics experiments and resulted in three Nobel Prizes in Physics [96–98] and many other accomplishments [14, 99]. SLAC’s research topics broadened in the 70’s and with the Stanford Synchrotron Radiation Project SLAC has become a X-ray user facility in 1974. The synchrotron source was modernized and is now known as the Stanford Synchrotron Radiation Lightsource (SSRL). The linear accelerator has been repurposed to function as the world’s first hard X-ray free electron laser (XFEL) and it is now known as the Linac Coherent Light Source (LCLS). LCLS began operations in April 2009 [14] and the AMO hutch started user October 2009 [100]. AMO started have the HFP and then CAMP end-station, however, the LAMP end-station was commissioned in September 2013 and the described experiment was performed in January 2014¹.

This chapter is organized as follows, section 3.1 goes over the the details of the AMO instrument. Section 3.2 focuses on the specifics of the LAMP end-station. Section 3.3, which centers around relevant sample delivery. The chapter ends with section 3.4 and 3.5 that describe important detectors, namely the pnCCD and time-of-flight (TOF) detectors, for the LAMP end-station.

3.1 The atomic, molecular and optical physics instrument and front end enclosure at the LCLS

The atomic, molecular and optical physics (AMO) instrument is located closest to the undulators of the LCLS at hutch 1. The AMO instrument is designed for soft X-ray photons in the energy range from 280eV - 2000eV [1, 101], where the beam divergence

¹Experimental identifier at SLAC: AMOA1214

3 Experimental Setup

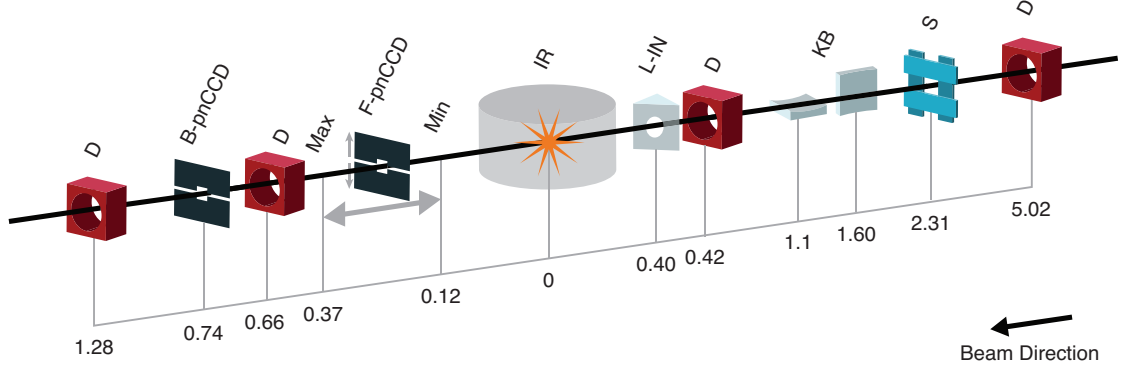


Figure 3.1: Schematic overview of the AMO beamline instrumentation in the LAMP configuration. The indicated distances below the schematic items are in meters from the interaction region. As the X-ray beam enters the instrument, it can be visualized on a YAG crystal diagnostics (D). A set of 2 slits (S) cuts the beam in the vertical and horizontal to reduce straylight from the Kirkpatrick-Baez (KB) optics. The differential pumping section of the LAMP end-station houses another YAG crystal diagnostics (D) and an option couple in an optical laser (L-IN) on-axis with the X-rays. The front and back pnCCD (F/B-pnCCD) are located downstream of the IR with further beam viewing options (D). From [1].

is a limiting factor for lower energies and the B4C-coating on some mirrors leads to absorption above 2000eV. After the X-ray pulse generation in the undulators of the LCLS the beam is transported to the Front End Enclosure (FEE) [102], where the electron beam is deflected using magnets and subsequently dumped in a beam stop such that only X-rays continue. Optionally, the XTCAV² can be used to give insight into the kinetic energy and pulse duration of the electron beam. In the FEE, the X-rays can be attenuated with either a gas or a solid attenuation scheme. A X-ray pulse energy monitor, often referred to as gas detector, measures the pulse energy of a single shot before and after the attenuation [103]. Eventually, the X-ray beam is deflected through a mirror system into the desired hutch. To direct the beam to the AMO hutch, the soft X-ray offset mirrors (SOMS) are being used. SOMS are a set of three mirrors, where the first two are shared to steer the beam into hutch 2 or the Soft X-ray (SXR) instrument [104–106]. The AMO instrument is very versatile in it’s configuration and can use three different end-stations. From the time of first comissioning, end-station 1) is the High-Field Physics (HFP) end-station [100, 101], 2) the CFEL-ASG Multi-Purpose (CAMP) end-station [107] and 3) the LAMP instrument [1, 68]. As the experiment described in

²More information about the XTCAV can be found in appendix ??

3.1 The atomic, molecular and optical physics instrument and front end enclosure at the LCLS

the present work has been performed with the LAMP end-station, we shall focus on that configuration from here on. A schematic overview of the AMO beamline instrumentation in the LAMP configuration can be found in figure 3.1. As the X-ray beam travels from the FEE to the AMO beamline, it can be projected onto a YAG crystal diagnostics (D). Here the shape and position of the beam can be well determined as it is several meters downstream of the SOMS such that a difference the SOMS angle and position can be determined with sub-millimeter precision. The projection also reveals the alignment of the beam to several differential pumping apertures that are located in the FEE [108]. In the described experiment, the X-ray beam became unstable and the pointing of the electron beam was jumping. The most upstream YAG crystal of the AMO instrument was able to detect this jitter. A beamline alignment laser (typical HeNe-laser with low beam divergence) can be coupled into the beamline shortly downstream of the YAG screen³ such that it co-propagates with the X-rays. Beamline alignment laser are invaluable tools to pre-align a system before X-rays are taken. For the described experiment, it was necessary to align the particle jet of the pristine Xe-cluster and the particle jet of the HeXe-cluster to be perpendicular to the X-ray beam (see 3.7). In order to perform this alignment, a beamline alignment laser that co-propagates with the X-rays is useful if not required.

The X-ray beam then travels through a set of 4 blades (S) that can be moved independently to cut into the beam to reduce effects of straylight on the detectors, especially straylight originating from the Kirkpatrick-Baez (KB) optics [109]. In collaboration with the Single-Particle Initiative, it was investigated how the 4-blades reduce unwanted scattering from and it was found that the blades should not cut into the main intensity profile of the beam, but rather conservatively cut into the halo of the beam [110]. This still sufficiently reduces straylight but does not reduce the peak intensity of the X-ray pulse (compare green and blue curve in figure 3.2). The KB optics focus the X-ray beam into the interaction region. The optics consist of two 400 mm long silicon (Si) substrates that are coated with boron carbide (B4C). They reflect the X-rays in grazing incidence at 13.85 mrad and are sometimes called KB mirrors. One mirror reflects the beam in the horizontal and the other reflects the beam in the vertical. As the mirrors are located at different positions, the mirrors are designed to have a focal length of 1600 mm in the horizontal and 1100 mm in the vertical. Additionally, the mirrors are bent to change their focusing position along the Z-axis⁴ and through 1) the study of time-of-flight (TOF)

³Not shown in figure 3.1

⁴The LCLS uses a right-handed coordinate system, where the index finger (Y-axis) points up and the middle finger (Z-axis) points parallel to the X-ray beam.

3 Experimental Setup

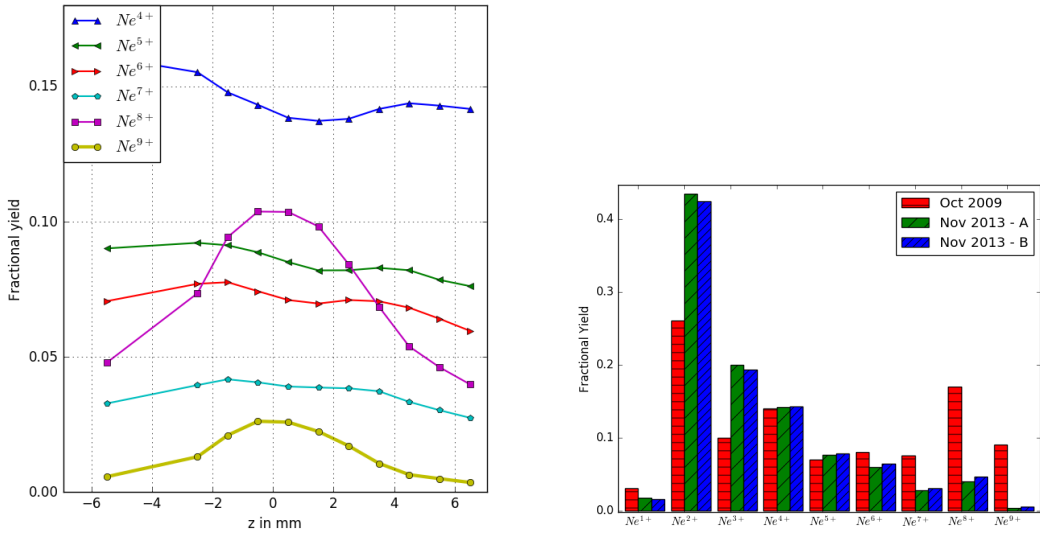


Figure 3.2: Left graph: Atomic neon charge state yield from time-of-flight mass spectroscopy as a function of Z , relative to optimal focus position $Z = 0$. $Z = 0 \pm 1$ is a favorable length for sample injection. Right diagram: Comparison of atomic neon charge state yield from time-of-flight mass spectroscopy for different cases. Red: Experimental data from October 2009 with (S) opened. Green: Experimental data from November 2013 with (S) closed. Blue: Experimental data from November 2013 with (S) opened.

3.1 The atomic, molecular and optical physics instrument and front end enclosure at the LCLS

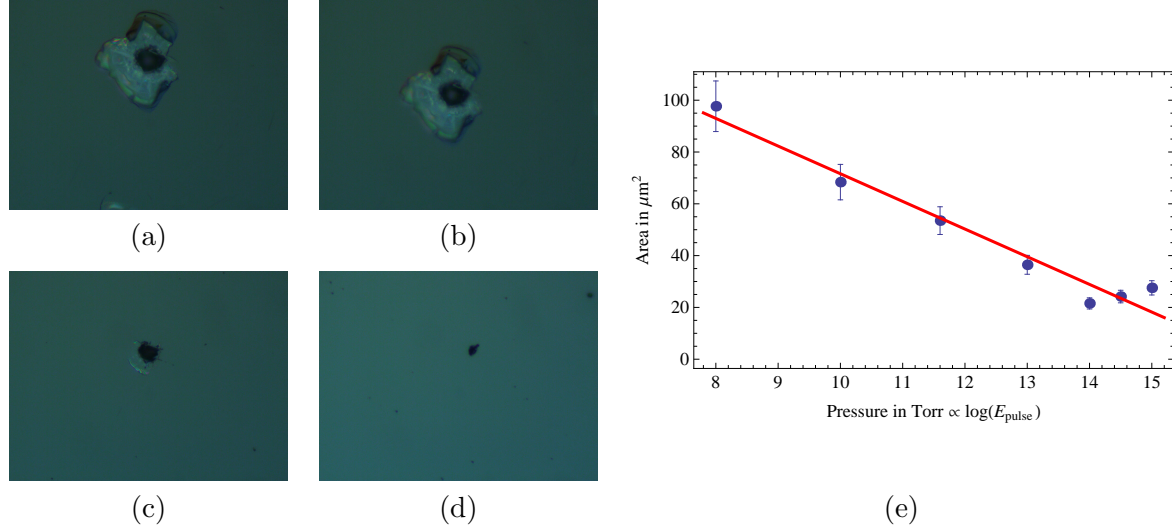


Figure 3.3: a)-d), ex-situ microscope imprint study of a lead tungstate (PbWO_4) sample that was irradiated with single LCLS pulses at 1600eV at different gas attenuation using the LCLS gas attenuator. e) crater area as a function of the gas attenuation. The slope of the curve could be used to determine the focal spot size to be TBD.

mass-spectroscopy [68] or 2) imprint analysis [111, 112] the focus can be characterized. A study and manipulation of the X-ray focus is necessary to achieve small X-ray focii increase the fluence of the sample interaction region, which is desired in coherent diffractive imaging as thus more photons scatter from the sample and, ideally, to understand the coherent wavefront that creates an image of the particle better. To characterization method 1) Figure 3.2 left shows a focus characterization along the Z-axis using a TOF spectrometer. The fractional neon ion yield per charge state is summed and plotted as a function of Z-position. An area of 2mm around $Z = 0\text{mm}$ could be determined as useful operating condition. Figure 3.2 right, compares fractional neon ion yield at optimal focus position from November 2013 [68] to October 2009 [113]. The comparison reveals that high charge states of neon, for example Ne^{8+} and Ne^{9+} , are less frequent due to deteriorated beamline optics. 2) Figure 3.3 left shows images from a microscope of how a LCLS X-ray pulse at 1600eV interacts with a lead tungstate (PbWO_4) sample at different gas attenuation. The gas attenuation was set with the LCLS gas attenuator that is located in the FEE. The crater area can be measured after calibration of a microscope and it is shown in [114] that the crater growth over pulse energies E_{pulse} is dependent on the beam radius. The slope of the curve gives insight into the focal size. For the described experiment in this thesis, the X-ray beam focal size in FWHM was

3 Experimental Setup

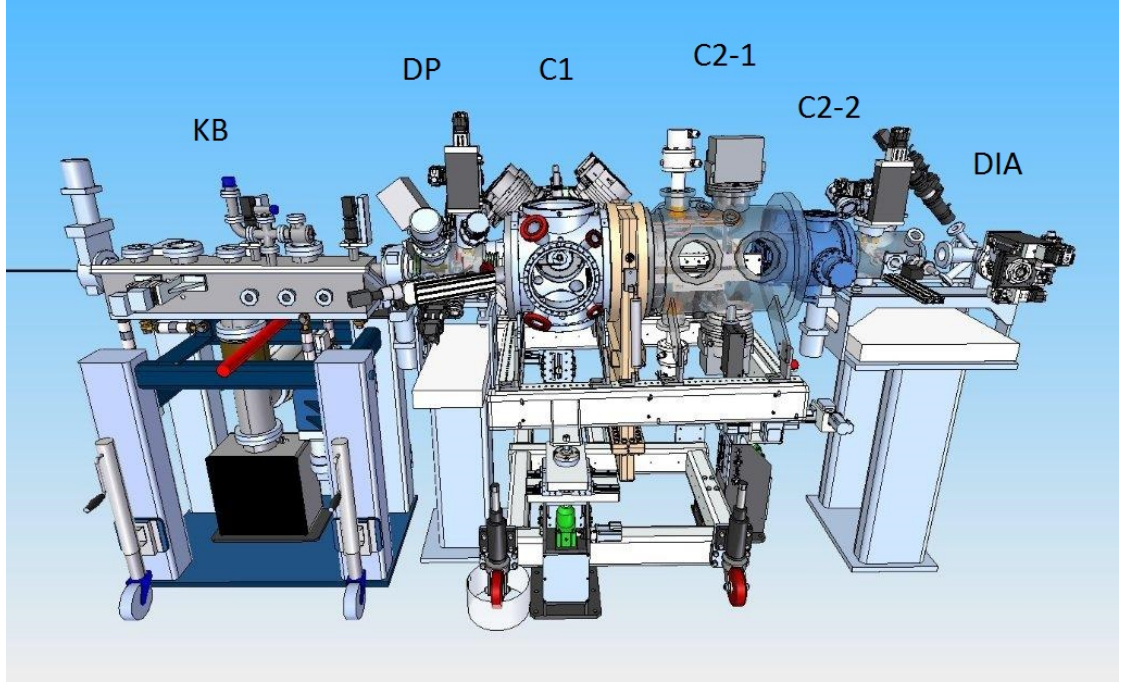


Figure 3.4: Overview of the AMO instrument in the LAMP end-station configuration. From left to right, the beam propagates through the Kirkpatrick-Baez (KB) optics, the differential pumping (DP) section, the interaction chamber (C1), the front pnCCD chamber (C2-1), the rear pnCCD chamber (C2-2) and finally the diagnostics (DIA) system. The C1 chamber has the AMO rare-gas cluster jet installed at the most distant conflat vacuum flange. For scale, the large, open conflat flanges on the C1 chamber are 12 inch.

determined to be $1.5\mu\text{m}$, with an effective area a $5 \mu\text{m}^2$.

3.2 The LAMP end-station at AMO

Still following the beamline layout in figure 3.1, the X-ray beam enters the LAMP end-station after the KB mirrors (see also the overview in figure 3.4). LAMP begins with a differential pumping (DP) section that separates the interaction (C1) and detector chambers (C2-1, C2-2) from the KB optics and other upstream beamline instrumentation. The differential pumping section consists of two small chambers that are pumped via turbo-molecular pumps and are interconnected to the LAMP chamber system via 5 mm, 8 mm, or 10 mm diameter differential pumping apertures (indicated in figure 3.5). The differential pumping stage is able to maintain up to 4 orders of magnitude pressure difference, for example $1e^{-10}$ bar in the KB-optics vacuum tank and $1e^{-6}$ bar

3.2 The LAMP end-station at AMO

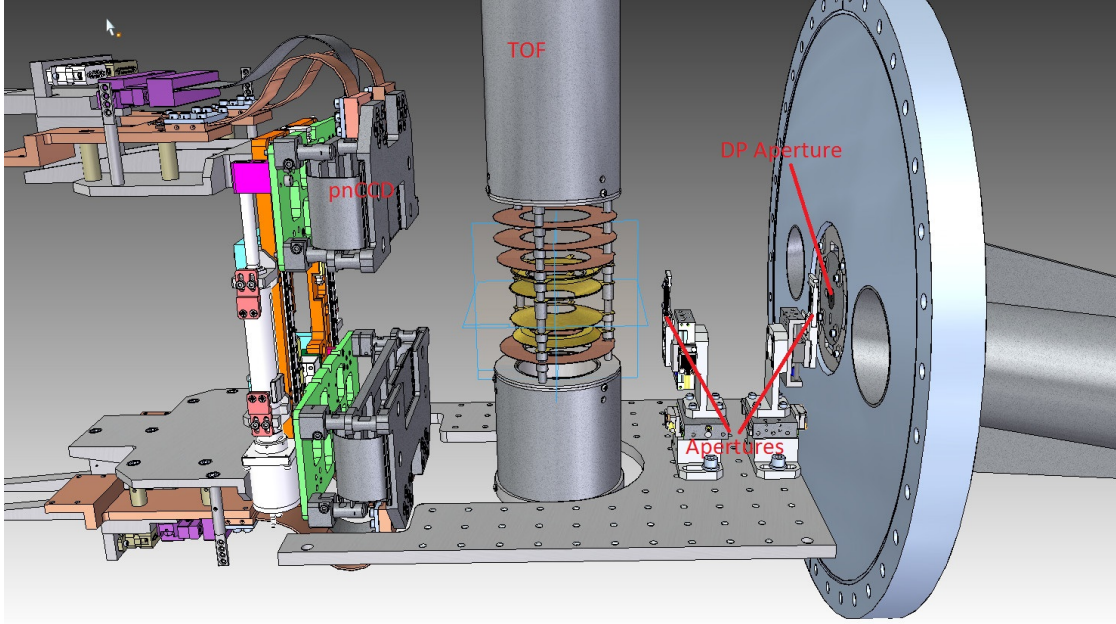


Figure 3.5: Inside view of the C1 chamber showcasing the interaction region.

in the interaction region. The first differential pumping stage holds a YAG crystal to examine the X-ray beam after the KB optics. The second stage holds optionally a laser in-coupling mirror to overlap X-rays with an optical laser or a straylight aperture to prevent scattering from the differential pumping apertures and upstream elements.

The beam then travels into the C1 chamber that encloses the interaction region. Before reaching the sample interaction region, the beam is cut by apertures, further reducing straylight (see figure 3.5). The apertures are mounted on encoded piezo stages with sub-micron movement precision. The used aperture material is silicon nitride (Si_3N_4) with tapered edge windows to allow the X-rays to traverse. The windows can be either fit to the size of the X-ray beam diameter, which can be estimated using geometric optics, or by using one corner of the window on the first aperture stage and the opposite corner on the second stage. As straylight is a concern in CDI type experiments, an improved aperture system was designed using blades with tapered edges. This allows full control over the aperture from each direction and was commissioned in collaboration with the Single Particle Imaging initiative [110].

In the center of C1, where sample and X-rays interact, a time-of-flight spectrometer is located (see figure 3.5) that we will describe in the section 3.5. The beam then passes the front pnCCD, which is mounted on a moveable stage. Another in-vacuum manifold allows the use of another YAG crystal (D), an optical filter and a B4C beam stop just

3 Experimental Setup

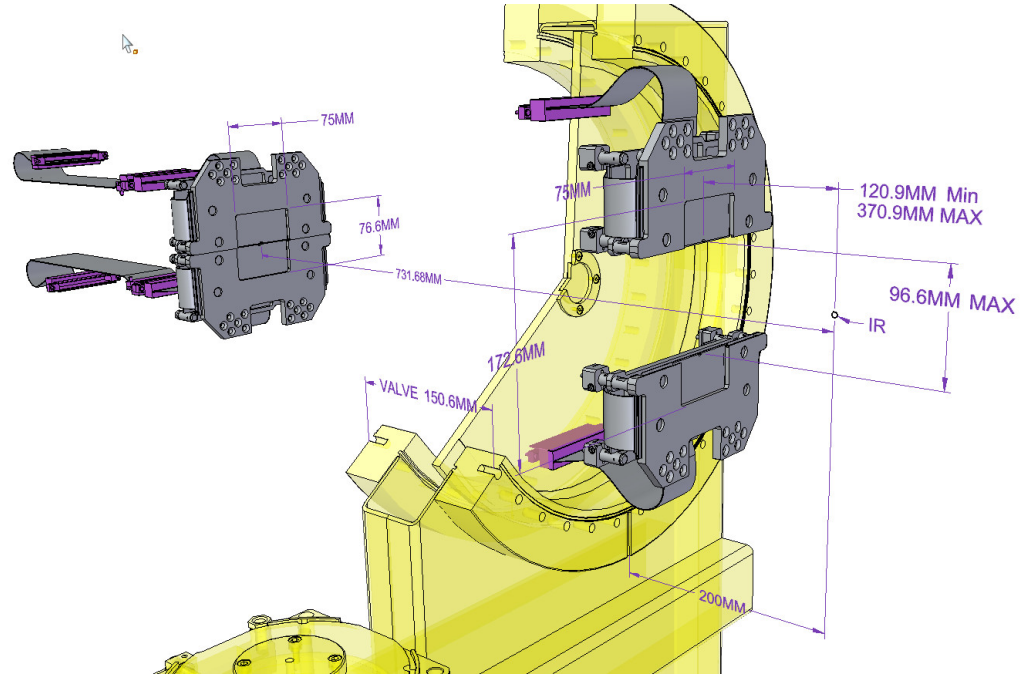


Figure 3.6: Side view of the rear and front pnCCD detector in C1, C2-1 and C2-2. The interaction region (IR) is in the center of C1. The beam propagates along the Z-axis where the rear pnCCD is placed 731.68 mm away from the IR (original engineering distances). The half detector height is 38.3 mm and results in a half scattering angle of 4.26° . With the gate-valve installed, the front pnCCDs are able to travel along the z-axis from 370.9 mm to 120.9 mm downstream of the IR. The front pnCCDs position along the y-axis is adjustable and they can detect photons up to 86.3 mm from the beam axis. At maximum extension, the pnCCDs are thus able to detect photons up to a half scattering angle of $\frac{\Theta}{2} = 38.84^\circ$. TBD

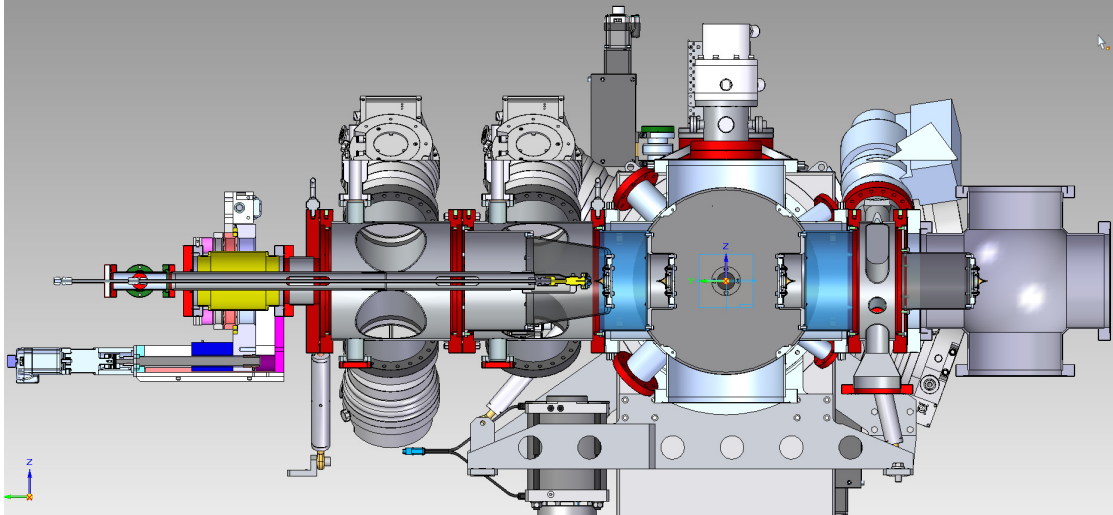


Figure 3.7: caption TBD

before the rear pnCCD. Figure 3.6 shows relevant engineering design distances of the pnCCD detectors inside the LAMP instrument. In the following, we consider the instrument to have the gate valve mounted and that the FEL focus position is in the center of the C-1 chamber. The distance from the focus to the bottom rear pnCCD detector module is 731.68 mm and the top, rear pnCCD module is 3.15 mm closer to the C-1 chamber⁵. As mentioned, the front pnCCD module can be moved along the Z-axis. The distance from the front-bottom pnCCD module to the focus can be set between 117.75 mm - 367.75 mm. The front-top pnCCD module is again 3.15 mm closer to the center of C-1. The front detectors can also be moved along the Y-axis and the maximum extent is 48.3 mm from the beam to the onset of the detector. The manufacturing size of the gate-valve along the z-axis is 150.6 mm. In the experiment, the front pnCCD have been in the most rear position.

3.3 Sample delivery

Two gas sources are used in order to create single rare-gas clusters. Single xenon and helium cluster are produced using the principle of the supersonic gas expansion into a vacuum that is described in section 2.2.1. Helium cluster doped with xenon are produced through the pickup principle as described in section 2.2.2. Given the time constraint

⁵These design distances are offset by +5mm along the Z-axis due to customization during the initial setup.

3 Experimental Setup

Chamber	Turbomolecular pump	Roughing pump
Xenon source	4x Leybold 361 Classics (361 l/s)	Pfeiffer Adixen ACG600 with roots blower (
Xenon skimmer	1x Maglev 300s (300 l/s)	
Helium source	a	a
Helium skimmer	a	Edwards 300 (5 l/s)
C1	a	Adixen 2
C2-1	4x Pfeiffer	

Table 3.1: caption TBD.

of performing experiments at the LCLS, both sources are installed in one setup and operate independently, allowing a quick sample change. A schematic setup can be found in figure 3.7 and a list of used vacuum pumps can be found in table 3.1.

The AMO cluster source, that produces single xenon cluster, consists of a Parker-Hannifin Series 99⁶ - pulsed valve using a solenoid with a custom manufactured conical copper nozzle, two vacuum chambers to mount two skimmers, a third adjustable piezo-slit skimmer and several vacuum pumps. It is a well characterized source that has been used extensively in the past [1, 36, 56, 83, 86]. The pulsed solenoid valve (see figure 3.8) is controlled and operated by a Parker-Hannifin Iota One pulsed valve driver. The valve driver applies a current to the solenoid, a magnetic cylinder actuates and the attached poppet opens and closes again after a set TTL signal from driver. The valve's opening time is set to 1 ms and repetition rates of up to 30 hz can be set at a xenon reservoir pressure of $p_0 = 1 - 20$ bar. The pulsed valve heats up substantially during operations and due to material deterioration, the vespel poppet is replaced every 60h of operating time, or as needed, to prevent a leaking gas source. The nozzle has a 200 μm diameter opening and an opening half angle of 4°. It is clamped to the Parker valve using an indium gasket to seal. Two skimmer with an opening of 1mm diameter and an adjustable piezo-skimmer have been installed to define the gas jet. The piezo skimmer allows fine control over the slit opening formed by two razor blades. The blades can be closed by applying a voltage $U = \{0, \dots, 12V\}$. At $U = 8V$, the cluster source operates in the single cluster regime. The background pressure $p_{\text{source}}, p_{\text{skimmer}}$ is handled through the pumps installed on the source and skimmer vacuum chambers, see table 3.1. Ultimately, the skimmer stages lowers the gas pressure in the interaction region $p_{\text{IR}} \leq 10^{-5}$.

Helium droplets were produced in a free gas expansion using an electron microscope diaphragm as nozzle (Plano A0200P) that has a 5 μm orifice and a orifice channel length of 2 μm [58]. The nozzle is cooled to cryogenic temperatures $T = 5.8$ K using a Sumitomo

⁶Series 99 is at the time of writing not produced/advertised as a straight, in-line pulsed valve anymore.

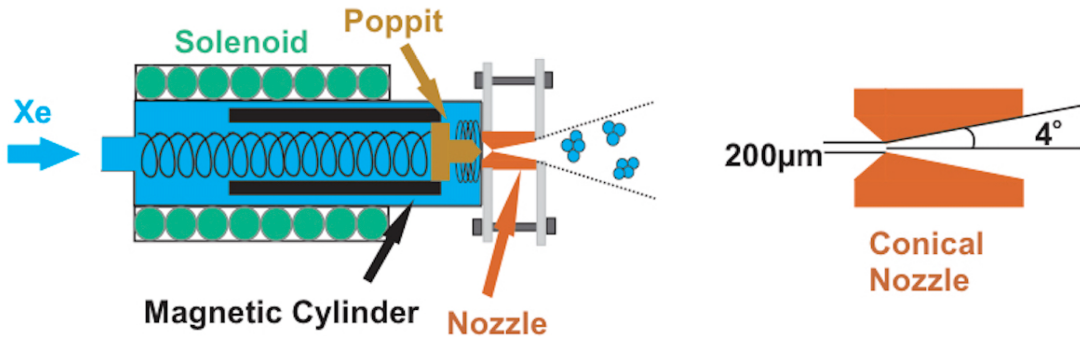


Figure 3.8: Schematic of the Parker-Hannifin Series 99 pulsed in-line valve and custom copper nozzle. The nozzle is clamped to the pulsed valve using an indium gasket to seal. The vespel poppet is attached to the magnetic cylinder and opens or closes the valve. If a current is run through the solenoid, the magnetic cylinder and thus the valve actuated. From [2]

cold-head. The particle beam is defined by a first 0.5mm and a second 1mm diameter skimmer. As explained above, a third piezo-skimmer allows to define the gas jet to single helium droplets. A doping unit is installed in the skimmer chamber of the helium source. The doping unit is a separate smaller chamber in the skimmer chamber, where He-cluster can traverse through. The gas cell allows locally increasing the background pressure of the cell with xenon to $p_{du} \leq 2.3 \cdot 10^{-3}$ Torr. The pressure is manually controlled using a leak valve. Since the gas load is confined in the doping unit, the vacuum system is not overloaded. As shown in figure 2.9, the partial helium pressure is determined with a residual gas analyzer (RGA) in the source chamber of the AMO cluster source, which can then be used to determine the depletion of the helium cluster through the pickup of xenon atoms. A thorough alignment of the sources is necessary to overlap the particle beams such they traverse through all skimmers. A summary of the alignment with a telescope and alignment laser is condensed in appendix 8.1.

3.4 The large area pn-CCD detectors

Diffraction patterns are recorded with pnCCD detectors in LAMP's C2-1 and C2-2 chambers. A pnCCD is a versatile device and has found usage in astronomy and material science. pnCCDs have been used previously at LCLS, namely in the CAMP instrument. At LCLS, detectors are mostly used for coherent diffractive imaging applications but have also spectroscopically capabilities, which were demonstrated in the left figure 2.13.

3 Experimental Setup

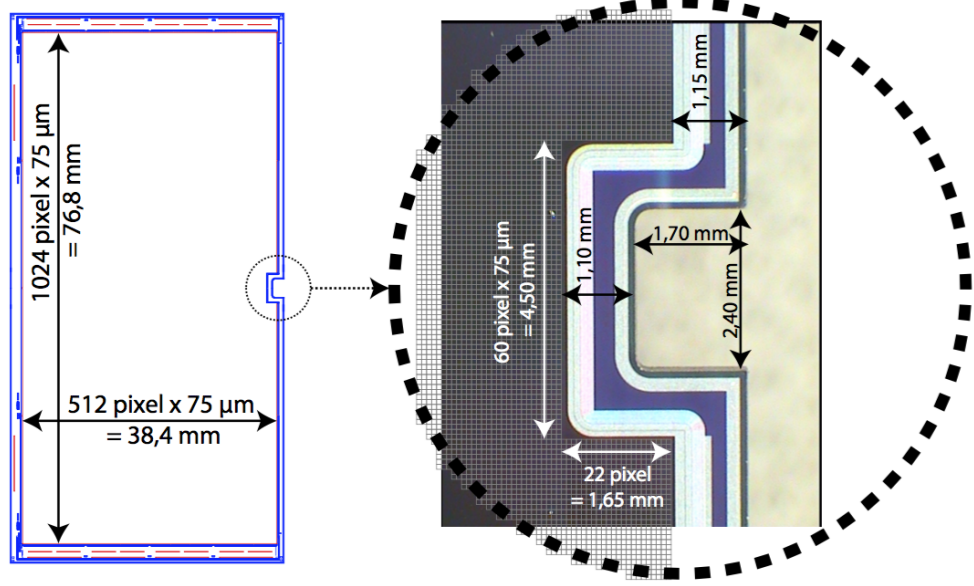


Figure 3.9: Geometry of a single pnCCD module with a detailed view of the beam conveying hole. A single module consists of 1024×512 pixel. Each pixel is $75\mu\text{m}$ which results in an active area of $76.8 \times 38.4\text{mm}^2$. The chip is surrounded by a non-active edges, which are 1.15mm wide on beam facing edges. The hole reduces the active area on one module by 60×22 pixel, or $4.5 \times 1.65\text{ mm}$ and allows the beam to propagate through a $2.4 \times 1.7\text{mm}^2$ hole.

The pnCCDs are attractive photon area detectors because of the following 4 reasons. First, their high quantum efficiency (QE) and good signal to noise ratio. Second, their read-out rate is very high (up to 200hz) and enables us to use the full repetition rate of LCLS (120hz). Third, their large, consecutive active areas cover wide scattering angles, and lastly, the detectors are almost defect free after applying the usual image corrections. These points are explained in detail in the following [68].

Let us begin describing their chip geometry. Each pnCCD detector (front or rear) is made out of two modules. Figure 3.9 shows the layout of a single pnCCD module. The chip consists of 512×1024 pixel. Each pixel has a size of $75 \times 75\mu\text{m}^2$, so the area that the detector covers is $38.4 \times 76.8\text{mm}^2$. To allow the FEL beam to travel through the instrument, each module has a rectangular region cut out. On a single module this area is $4.5 \times 1.65\text{mm}^2$ and for the whole detector this 'hole' has the dimensions $4.5 \times 4.5\text{mm}^2$. The size of this hole has been chosen to slightly oversize the diverging FEL beam at the rear pnCCD position (assuming a focus in the C1 chamber). The borders of each module are insensitive to photons and are $1.10 - 1.15$ mm thick. To minimize the overall detector area that is insensitive to photons, the two pnCCD modules are mounted such

3.4 The large area pn-CCD detectors

Key	relative gain	approx. ADU/keV	max. photons per pixel
1	1/256	5	1100
2	1/128	10	640
3	1/64	20	320
4	1/16	79	80
5	1/4	316	20
6	1	1250	5

Table 3.2: Typical generated ADU values and dynamic range using 1k eV photons at all pnCCD gain settings. It is a valid approximation to linearly extrapolate to other photon energies.

that the not sensitive areas overlap. As a result from that, each top module is 3.15 mm closer to the interaction region than each bottom module. The effective gap that is seen in the laboratory frame images between each top and bottom module measures 16 pixel, i.e. 1.2 mm.

The pnCCD chip is read out with a specifically for the pnCCDs designed CMOS multi-channel Analog MultiplEXer (CAMEX). The CAMEX pre-amplifies the charges through a set of gain amplifiers and enables a parallel read-out of 128 pixel rows simultaneously. Each CAMEX converts the signal to an analog output, enabling to read out all pnCCD rows at once, thus allowing the high read-out speed of up to 200hz. The analog signal is converted to a digital signal and the image information is stored by the LCLS Data Acquisition (DAQ) in the LCLS psana network, where it is accessible for analysis.

The pnCCD can be operated in different gain modes to be more sensitive to photons (high gains) or to have more dynamic range (lower gains) as shown in table 3.2. The different gain amplifications are applied through the CAMEX. Gain $\frac{1}{1}$ is the highest gain and $\frac{1}{256}$ is the lowest gain. As you step from highest to lower relative gains (e.g. from 1 to 1/64), the ADU value creation per photon goes as well with that fraction. Hence, going to lower gains reduces the signal-to-noise ratio but increases the dynamic range. Note, that the table shows typical operating values using $1keV$ photons and that the ADU value creation is dispersive. The thin and unstructured radiation entrance windows, have a high quantum-efficiency from the infra-red (IR) to soft X-ray regime and in order to avoid unwanted scattering, the photon entrance windows (located at the back of the detector) are coated with 50 nm aluminum to reduce their sensitivity from infra-red and optical light. This aluminum coating does attenuate the soft x-rays at AMO only slightly but the detectors maintain a QE of 90%. At AMO it is thus possible and handy to linearly extrapolate the generated ADU values to other photon energies,

3 Experimental Setup

for example a 1.5k eV photon will generate approximately 1750 ADU in highest gain (compare figure 2.13). There is also an optical aluminum filter mounted from the front of the chip to drastically reduce wrongly directed scattering and straylight.

3.5 Time of flight mass-spectrometer

An ion time of flight spectrometer was used in the interaction region to detect xenon and helium ions. A time of flight spectrometer uses electric fields to accelerate ions from the interaction region (IR) towards a detector. The detector unit often consists of a micro-channel plate (MCP) that allows a position sensitive detection of the particle signal.

In the first stage, the ions are accelerated from the IR towards the detector. Here, the electric potential energy is converted into kinetic energy

$$qU = \frac{1}{2}m \left(\frac{d_1}{t_1} \right)^2, \quad (3.1)$$

$$t_1 = \sqrt{\frac{m}{2qU}} \cdot d_1, \quad (3.2)$$

with q being the elementary charge of the ion, U the Voltage difference- and d_1 the distance between the IR and spectrometer, m is the mass of the ion and t_1 is the time of flight in the acceleration stage. The ions then travel through a drift tube of length d_2 that is fieldless. As the velocity remains constant, we can write down

$$t_2 = \sqrt{\frac{m}{2qU}} \cdot d_2, \quad (3.3)$$

with t_2 being the time of flight in the drift tube. The total flight time can then be written as

$$t_{\text{time of flight}} = t_1 + t_2 = \sqrt{\frac{m}{2qU}} (d_1 + d_2), \quad (3.4)$$

$$t_{\text{time of flight}} \propto \sqrt{\frac{m}{q}}. \quad (3.5)$$

Typically, in an experiment all other constants can be considered constant. As the spectrometer is a cylindrical system, the time of flight denotes the final position on the detector and vice versa. Therefore the position sensitive MCP yields insight into the $t_{\text{time of flight}} \propto \sqrt{\frac{m}{q}}$ of the ensemble of ions in the IR upon interaction with an X-ray pulse. Usually, ions start with a kinetic energy $E_{kin} \neq 0$ such that the flight times are

3.5 Time of flight mass-spectrometer

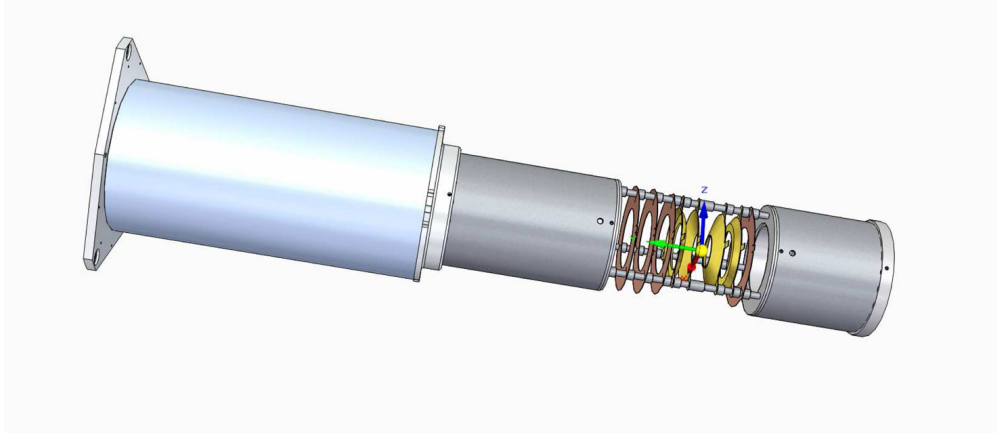


Figure 3.10: Drawing of the time of flight spectrometer.

altered. This results in a distribution of the ion signal instead of a strict peak structure. Atomic ion time of flight data typically exhibits a distinct peak structure while signal from clusters is strongly broadened due to kinetic energy from the nanoplasma expansion. Using this information, element specific data up to insights in the ionization cascades can be gained [115].

The in the experiment used time of flight spectrometer is depicted in figure 3.10. It consists of an electron and a longer ion side. With ± 5 keV power supplies, ions can be detected up to kinetic energies of 50 eV with a time of flight resolution of 100 ps [1]. If only the ion side is used, ions with kinetic energies of up to 100 eV can be detected. The use of ± 10 keV power supplies allows a detection of kinetic energies up to 150 eV. Electrons can be measured up to kinetic energies of 150 eV using ± 5 keV power supplies, 300 eV if only the electron side is used and 400 eV using ± 10 keV power supplies. Ions and electrons can be detected whether they are emitted in direction, in other words the spectrometer has a 4π solid angle collection [3]. A side view of the spectrometer can be found in figure 3.11. Ion, electron and photon trajectories upon interaction with a LCLS pulse have been simulated using SIMION by [3]. An conical lens stack avoids casting a shadow on the pnCCD detectors (top of image). The applied voltages in the experiment can be found in table 3.3. Here, the electron side is powered to have unperturbed electric fields across the interaction region.

3 Experimental Setup

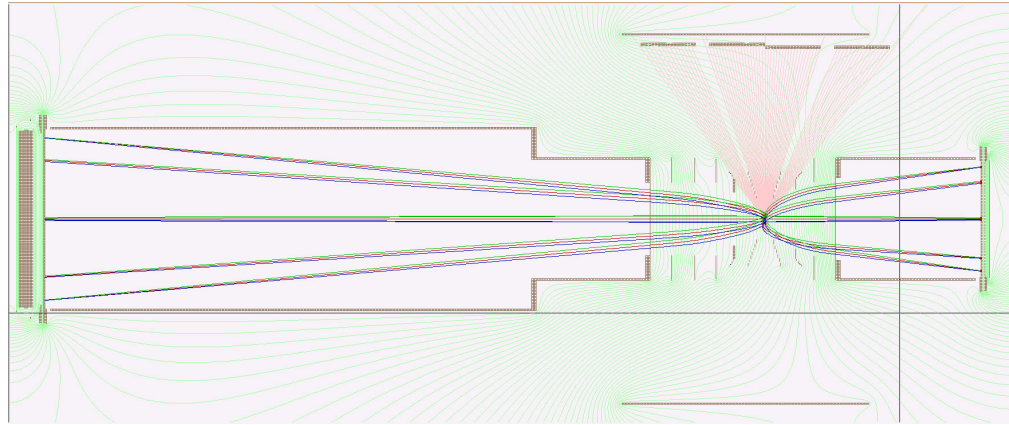


Figure 3.11: Sideview of the spectrometer showing ion, electron and photon trajectories upon interaction with LCLS. The image was created with SIMION. From [3]

Ion-side Connection	Voltage in V	El. Side Connection	Voltage in V
MCP Front	-2600	MCP Front	200
MCP Back	5	MCP Back	2200
Holder	200	Phosphor	3000
Conical lens 70deg	-923	Holder	6000
Conical lens 53deg	-1393	Conical lens 70 deg	500
Flat lens #1	-1490	Conical lens 53 deg	1370
Flat lens #2	-1564	Flat lens	1940
Flat lens #3	-1639	Flight tube	2736
Flight tube	-1714	-	-

Table 3.3: Set voltages to the time of flight spectrometer. Ion side use only.

4 Methods

Let us continue by conservatively estimating how much data is produced when using the LAMP end-station with both pnCCD detectors in use at a 120hz. Each pnCCD produces 120 images per second, each image is in a 32 bit per pixel format such that an image is vaguely 4 megabyte in size. So, every minute the front & rear pnCCD produce approximately 60 gigabyte of data. To analyze these vasts amount of data an extensive set of methods and optimized algorithms is required. This chapter is devoted to illuminate the analysis methods used in the present thesis.

The chapter is organized as follows, section 4.1 describes the general LCLS computing environment to establish an overview of the hard- and software capabilities. Section 4.2 discusses corrections that are applied to the raw pnCCD images. In section 4.4, several hitfinding methods are being evaluated. Section 4.5 goes over used phase-retrieval algorithms. Finally, section 4.6 discusses simulations of 2D projections of spheres and corresponding diffraction patterns.

4.1 The computing environment at LCLS

As estimated above, the vast amounts of data generated by many detectors are unhandy to handle by a single group of scientists that perform experiments at LCLS. For this reason the LCLS data acquisition (DAQ) group has incorporated many detectors, for example the the pnCCD and Aqciris digitizer, into their framework. All data taken at LCLS is stored in the LCLS computing environment, where the data can also be analyzed. As indicated in figure 4.1, DAQ readout nodes send the data traffic via Ethernet to a short-term cache and fast feedback (FFB) layer. While the data is being transferred, online monitoring nodes are able to 'see' a fraction of the live (online) data and run analysis. With a delay of a few ten seconds, the FFB nodes can be used to run analysis on the full data stream using parallelization, thereby having 'online' and 'offline' data access. Eventually the data is being moved to the 'offline' layer, where the data is managed by an integrated Rule-Oriented Data System (iRODS). The data is stored in .XTC file containers and it can also be accessed from outside SLAC (Router & ESNET).

4 Methods

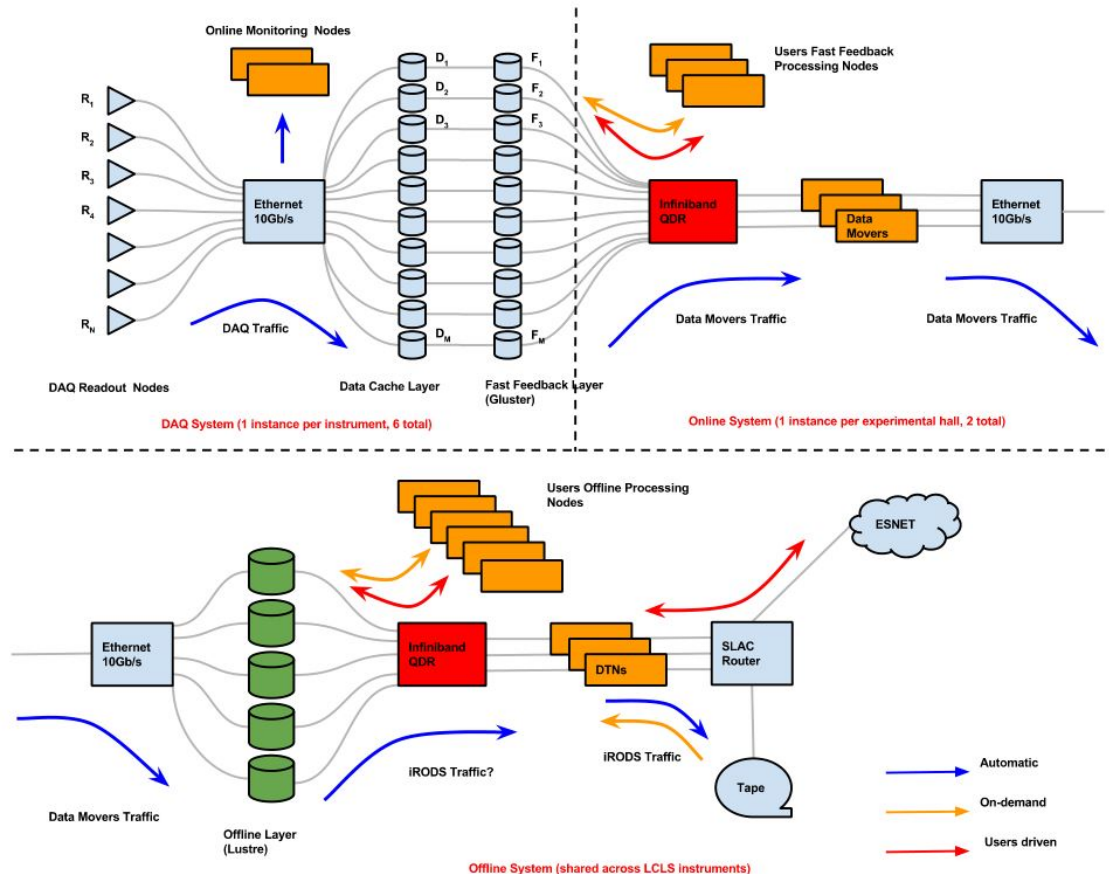


Figure 4.1: Diagram of the computing environment at LCLS and DAQ traffic. The recorded data is exchanged through Ethernet and after digitization, is stored on a cache and FFB cluster, where psana computer have access to the online environment during the experiment. Eventually, the data is moved to the more permanent offline environment, where data can be analyzed on psana computers or through a load sharing facility. See more in text. From [4]

The stored data has certain storage quotas and times. In brief, there is a 6 months short-term storage without quota limitations and a two-year medium-term storage with a storage quota of 10000 Giga-Byte. After that, the data is automatically stored for at least 10 years on magnetic tape (long-term storage) and can be restored upon request. A web interface is provided by the DAQ group to simplify and automate the data-handling and logging process. The short- and medium term storage solutions can also be used to analyze the data using the psana-framework to access data and to perform computations on the psana computer cluster with over 1000 CPU cores. A load sharing facility (LSF) allows the scheduling of (parallelized) batch jobs. The psana-framework can be interacted with python 2.7. The interacting python script calls functions within the psana-framework that are programmed in C(++)¹, for example detector calibrations. Psana allows parallelization via MPI and it is therefore possible to analyze many events (LCLS pulses) simultaneously. Also complex analysis is able process at the rate of the incoming data using MPI, when the FFB is used. Python scripts can be written for 'online' or 'offline' analysis and are of similar syntax.

For LCLS-II [4], the analysis and data-access scheme is designed to be similar to figure 4.1 with the exception of the online monitoring nodes. It is therefore recommended to build analysis schemes that are based on psana and use the FFB for online analysis, which can then be adapted easily for offline analysis as well. A quick introduction on how to use psana can be found in the appendix 8.2, where a few examples from the LCLS DAQ group are condensed.

4.2 **pnCCD photon detectors**

Before the pnCCD detectors can be used to take data, it is good practice to apply corrections to the raw detector image in order to cope with electronic noise. Since these corrections are used often, the LCLS detector and DAQ group has implemented a calibration manager tool¹ that provides the necessary algorithms and helps with the procedure of applying image corrections and more. We discuss the two most often used corrections next. One, corrects for the electronic noise pedestals (levels) of each pixel, and two, accounts for common modes, e.g. artifacts from the read-out electronics that appear for the pnCCD in columns.

The effects of applying these corrections are illustrated in figure 4.2 through a set of histograms. The histogram bins are showing ADU values from dark pnCCD images in

¹The calibration manager tool 'calibman' can be found in the 'psana' software package. More information under <https://confluence.slac.stanford.edu/display/PSDM/Calibration+Management+Tool> (Oct 2016)

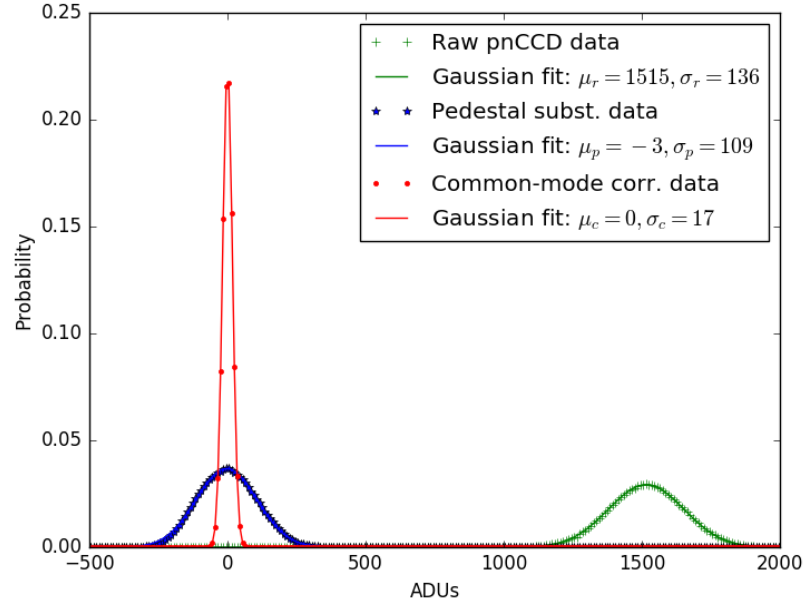


Figure 4.2: ADU histograms from electronic noise of not illuminated pnCCDs in highest gain mode. The green, plus symbols reflect a histogram of ADU values from raw electronic noise of pnCCD pixel. One can see that the noise is set off zero at $\mu_r = 1515$ ADU and has a standard deviation $\sigma_r = 136$. The same data shifts to the blue stars after applying the pedestal subtraction. The noise is centered around $\mu_p = -3$ and it's standard deviation is reduced to $\sigma_p = 109$. For the red data points, the common-mode corrections have additionally been applied. Now, the noise is well-centered at $\mu_c = 0$ ADU and σ_c is significantly reduced to 17. Note again, that this is an ADU histogram of purely electronic noise in highest-gain imaging mode.

highest gain. The green curve shows the ADU values of a raw detector image where no corrections have been applied, i.e. the electronic noise response from the chip has a standard deviation of $\sigma_r = 136$. Note, that there is also a significant offset of the distribution from 0 to $\mu_r = 1515$ ADU. The blue curve shows the same data but is using the pedestal corrections found in 'calibman'. The pedestal corrections reduce the noise slightly to $\sigma_p = 109$ ADU, and as expected, the pedestal corrections drastically move the normal distribution to be centered around $\mu_p = -3$. Finally, the red curve is also the same data than the green curve but includes pedestal and common-mode corrections. The corrected read-out modes drastically improve the standard deviation to $\sigma_c = 17$ and slightly move the mean to $\mu_c = 0$.

As a guideline, the pedestal corrections should be always used to account for the mean offset. The common-mode calibration, however, should be tested before applying. The algorithm that determines common-modes needs to find a baseline and therefore needs pixel with no signal in each row and column. In single-particle imaging the detector is illuminated in (almost) every pixel. Then the common-mode correction algorithm may treat real signal as noise and fail to find a common baseline.

In the present thesis, pedestal and common-mode correction has always been applied on the front detectors, as these pixel hold mostly signal from single photons. The rear pnCCD uses the pedestal correction but corrects common-modes only above a certain, conservative threshold. See figure 4.3 for the visible effect on front detector (large, top/bottom arrays) and rear detector (small, centered array).

4.2.1 Combining multiple pnCCD detectors

In order to maximize resolution, it is most useful to combine multiple pnCCD detector modules into one image. While this is a simple task on itself, it becomes more complex, when the combined images need to undergo a phase-retrieval process that use fast Fourier transformations (FFTs). In fact, it has not yet been shown in single-particle imaging that it is possible to retrieve a real space image from multiple detectors in different planes. The reason for this is that thus far there was little incentive of merging multiple detectors. Until recently, typical samples were on the order of several hundred nanometers in diameter such that little signal could be detected at large scattering angles. With the intensities provided by LCLS and the single-particle imaging capabilities of the LAMP end-station objects that are smaller than a hundred nanometer in diameter can be studied. Besides the ability to cover larger scattering angles, multiple detectors can be operated in different gains and still be combined efficiently. For the pnCCD, this

4 Methods

allows not only an increase in dynamic range but improves the signal-to-noise.

Let us now describe the process of combining diffraction images, while simultaneously preparing them for the inverse problem of phase-retrieval. The discussion now follows the code shown in appendix 8.5. The input for the following procedure are two pnCCD images. The images should be pedestal corrected and if possible common-mode corrected. Analysis of the electronic noise determines an cutoff or offset between signal-to-noise for each image (see left figure 2.13 and 4.2). At this step it is also convenient to account for different detector gain settings using the table 3.2 and normalize detector distances using, e.g., the following equation to correct the signal to the front pnCCD plane

$$\text{image}_{\text{normalized}} = \text{image} \cdot \frac{\text{gain}_{\text{front}}}{\text{gain}_{\text{rear}}} \cdot \frac{\text{distance}_{\text{rear}}^2}{\text{distance}_{\text{front}}^2} \quad (4.1)$$

The pnCCD front top and bottom module are placed in an enlarged array to reflect the real geometry in the plane of the front pnCCD. We can now translate this with pixel constructed geometry to use the more general scattering angle Θ

$$\Theta = \arctan \left(\frac{\sqrt{\text{pixel}_x^2 + \text{pixel}_y^2} \times a}{d} \right), \quad (4.2)$$

with pixel_x and pixel_y being the distance in units of pixel from the beam along the X- and Y-axis, respectively. We can use this information to further generalize the matter and attribute a scattering vector \vec{Q} to each pixel

$$\vec{Q} = 4\pi \frac{\sin(\frac{\Theta}{2})}{\lambda}, \quad (4.3)$$

with λ being the wavelength of the scattered photons. We can now add the signal from the rear pnCCD to the enlarged array, while using the generalized coordinates \vec{Q} . In this generalized downsampling process, the mean pixel is used, which is why a normalization factor needs to be carried. The downsampling into the enlarged array also preserves the pixel size of the front pnCCD (enlarged) array and allows Fast Fourier Transformation (FFT) algorithms to use the array. The usage of FFT algorithms is of great interest to reduce computing times in iterative phase-retrieval algorithms.

Figure 4.3a shows a diffraction pattern from a spherical xenon cluster of ~ 50 nm in radius. The front pnCCD detector was set to slightly overlap with the rear pnCCD detector along the Y-axis but the front detector was set ~ 365 mm closer to the interaction region along the Z-axis. All four of LAMP's pnCCD modules have been combined in

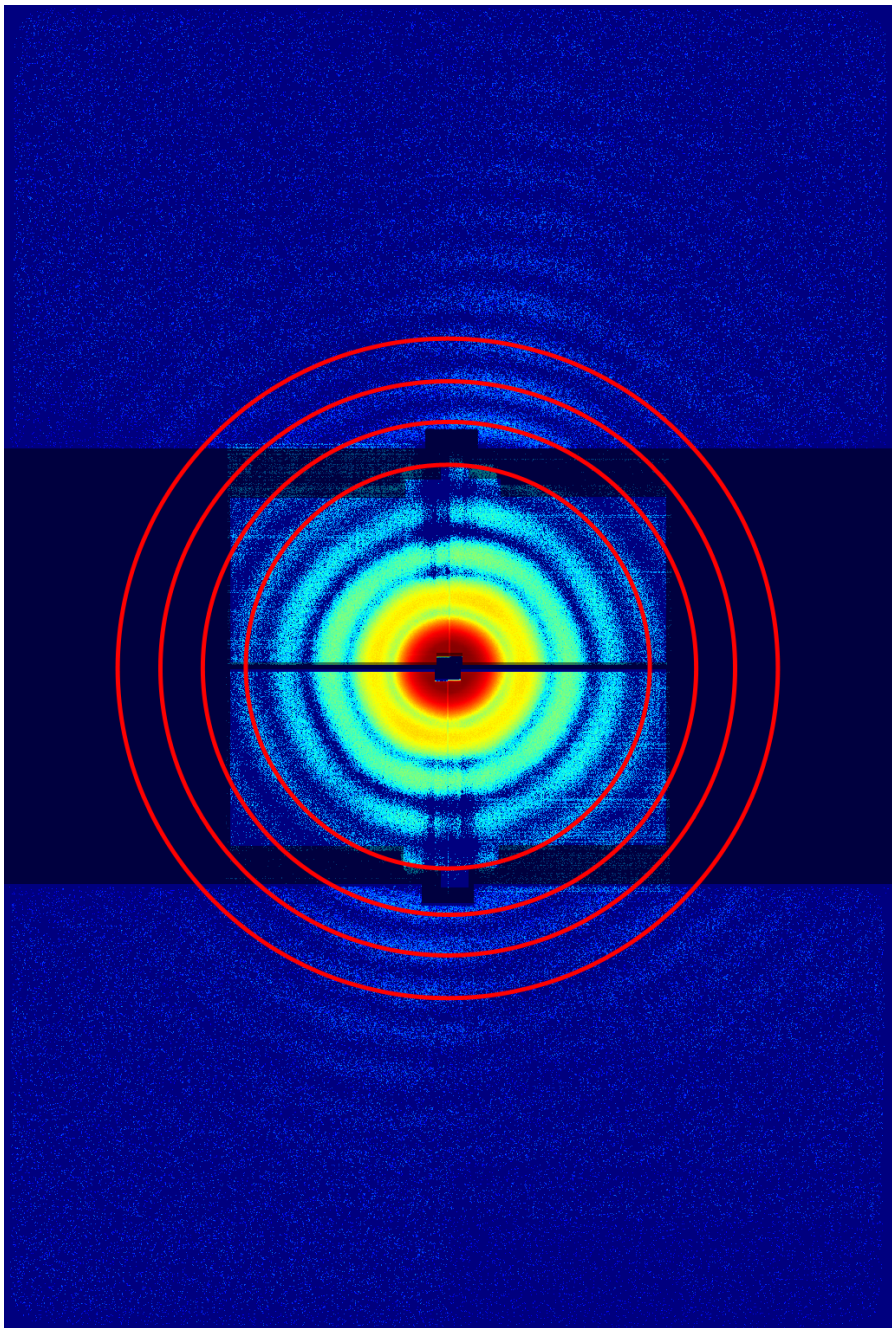


Figure 4.3: A combined pnCCD image using the full image of the front pnCCD and a down-sampled image of the rear pnCCD. The red circles in the image are drawn in to visualize the alignment of the detectors. As described in the text, the intensities in the image are normalized and corrected for different electronic gains and distance to specific detectors. The shaded areas are not covered by the pnCCDs and are therefore masked out.

4 Methods

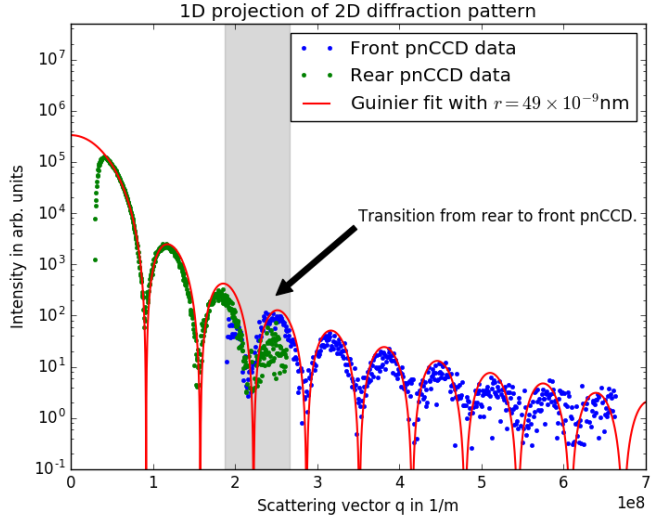


Figure 4.4: In this graph a 2D diffraction image was projected onto 1D assuming a spherical symmetry of the diffraction pattern. The green data points are gathered from the rear pnCCD and the front pnCCD data points are reflected by the blue data points. The red curve is a simulated scattering curve from an ideal sphere that has a radius of 49nm. The amplitude of the red curve has been fitted to the data points and it agrees well with the data over 8 diffraction rings. The gray shaded area shows the transition area from rear to front detector.

one image, and since the rear pnCCD is farther away from the interaction region it appears smaller on the combined image. The red circles are a help for the eye to align the modules and show how the diffraction pattern overlaps. In this case, the front pnCCD was operated in highest gain $\frac{1}{1}$ and the rear pnCCD was operated in lowest gain $\frac{1}{256}$.

The radial intensity profile yields valuable information about the geometric alignment and intensity normalization. Figure 4.4 shows the radial intensity profile of the spherical symmetric diffraction image over 5 orders of magnitude above the noise level. The red curve illustrates the expected scattering intensity of a spherical object with radius 49 nm and the amplitude was fitted onto the rear pnCCD data. The curve showcases the validity of the detected signal up to the edges of the front pnCCD, where little signal is present. There are also some discrepancies from the red curve on the transition from the rear to front pnCCD, which are due to the shade projected from the front onto the rear pnCCD and the resulting lack of signal.

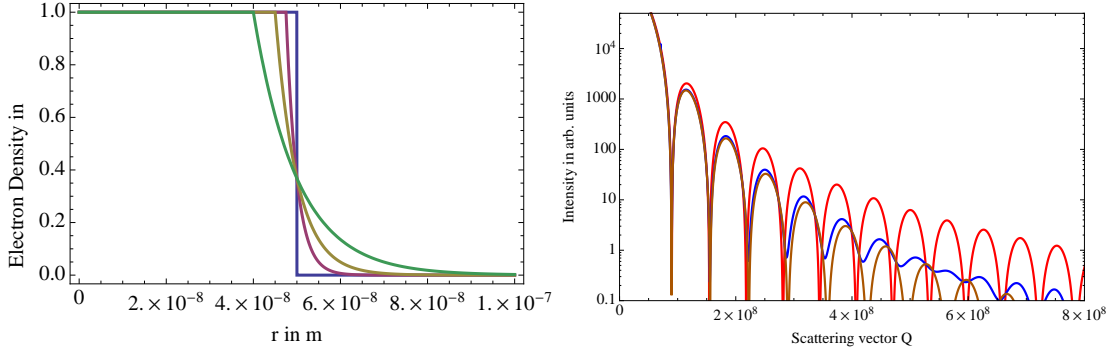


Figure 4.5: Left: electron density of an expanding spherical symmetric nanoplasma. Right: red line, scattering of an intact sphere. Brown, scattering of an expanding sphere with $k = 5\text{nm}$. Blue, combined scattering of an intact and expanding sphere that has been pumped with 10% and probed with 90% of the overall pulse energy. See more information in text.

4.2.2 Impact of X-ray pump – X-ray probe on diffraction pattern

In a coherent diffractive imaging X-ray pump – X-ray probe experiment, both pulses contribute to the scattering image. The pump pulse will project an image of the solid and intact cluster, while the probe pulse will propagate an image of the expanding, damaged cluster. In the present experiment, the pump pulse was set at $\sim 10\%$ of the overall pulse energy, while the probe pulse was set to $\sim 90\%$ of the overall pulse energy. In order to simulate the effects of the X-ray pump– X-ray probe setup, a 1D simulation is conducted using electron densities $\rho(r)$ of spheres. Although rare-gas cluster exhibit an icosahedral structure, at present resolution cluster can be well simulated using spheres. The spheres are allowed to expand after the model

$$\rho(r, k) = \begin{cases} 1 & \text{for } R - k \geq r \geq 0, \\ e^{\frac{(R-k)-r}{k}} & \text{for } R > r - k, \end{cases} \quad (4.4)$$

with R being the cluster radius and k an expansion coefficient such that

$$\int_0^\infty \rho(r, k) dr = R, \quad \text{if } 0 < k < R \quad (4.5)$$

4 Methods

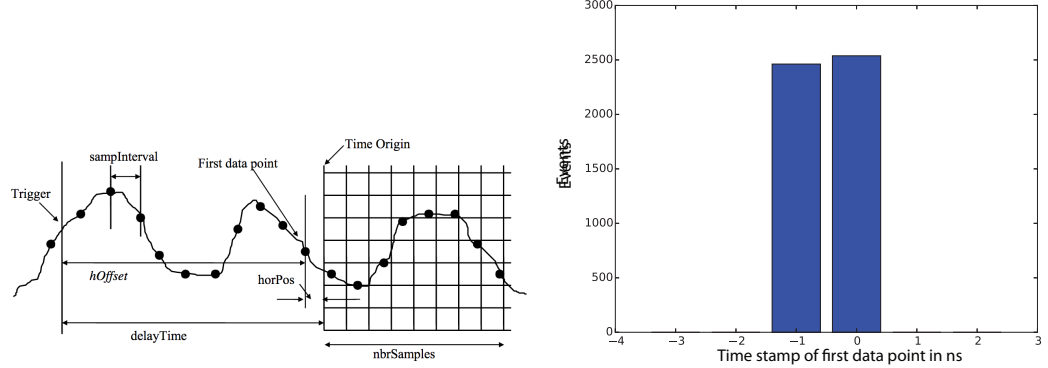


Figure 4.6: caption. Left image from [5]

The electron density can then be Fourier transformed into reciprocal space using the transformation [60]

$$F^2(Q) = A \left(\int_0^\infty \rho(r, k) \frac{\sin(Qr)}{Qr} 4\pi r^2 dr \right)^2, \quad (4.6)$$

with A being an intensity scaling factor. The electron densities for $R = 50$ nm and $k = \{0, 2.5, 5, 10\}$ nm are shown in figure 4.5 left. Figure 4.5 right showcases several cases of (expanding) spheres in reciprocal space. The red line is the scattering of a solid sphere F_{intact}^2 , with A being used to scale the intensity to typical experimental data. The brown curve is the scattering of an expanding sphere $F_{\text{expanding}}^2$ with $R = 50$ nm and $k = 5$ nm. Lastly, the blue curve corresponds to the case, where $A \cdot F^2 \rightarrow A \cdot 10\% F_{\text{intact}}^2 + A \cdot 90\% F_{\text{expanding}}^2$. Although the pump pulse influences the diffraction pattern visibly at high-Q values, the added signal remains in the noise level of $F^2(Q) < 1$ (compare figure 4.4).

4.3 Acqiris data sampling

An Acqiris digitizer has been used to read out the waveform signal from the time-of-flight spectrometer. For technical reasons, the Acqiris sampling and the electronic trigger to start the readout process is generally not in sync. The electronic trigger can occur between sample $\{0, 1, \dots, 10\}$. In other words, the Acqiris reads out 40,000 samples but the trigger for the clock comes between sample 0 and 10 and but that can be corrected. As it is illustrated in figure 4.6 left, the time difference between the first data point and the time origin is within the sampling interval, thus $\{-1\text{ns}, 0\text{ns}\}$, at the sampling rate at

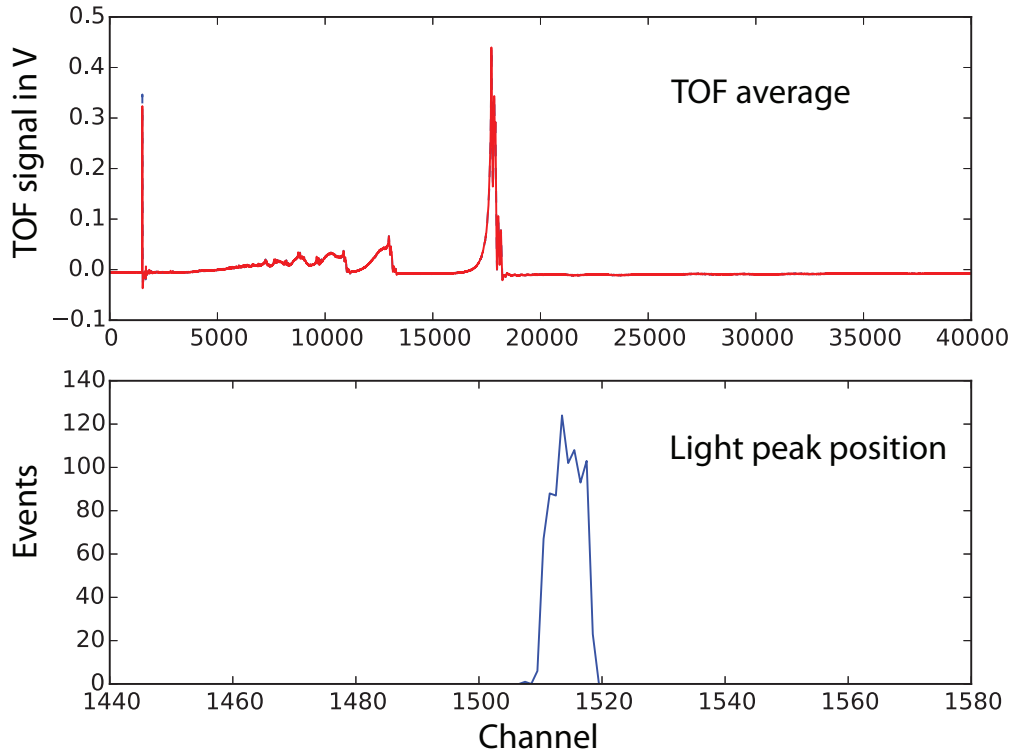


Figure 4.7: caption

40,000, which is 1 ns per channel [5]. Figure 4.6 right is an histogram of the First data point timestamp showing the evenly distributed discrepancy. As each read out sample would be different length $\{39990, 39991, \dots, 40000\}$, the LCLS DAQ group adds zeros to the end of each array to simplify the analysis of handling arrays of different lengths.

However, in an LCLS experiment, the origin of time is best defined by the light peak. The time of flight spectrometer will detect photons scattered off the sample as the pulse is traversing through the system. Figure 4.7 bottom shows an analysis of the light peak channel position. The lightpeak occurs within a ~ 10 ns window and is evenly distributed. This is a surprisingly large time-window that indicates that there is a $\sim \pm 5$ ns jitter around channel 1514 of the Acqiris trigger to the LCLS pulse. Figure 4.7 top shows a merely averaged TOF trace (blue curve) and a TOF trace that has been corrected for the light peak occurring at different position (red curve). Interestingly, the corrected average (red curve) has a lower average light peak signal than the uncorrected curve. This could be a result of low pulse energy LCLS pulses that would have been

4 Methods

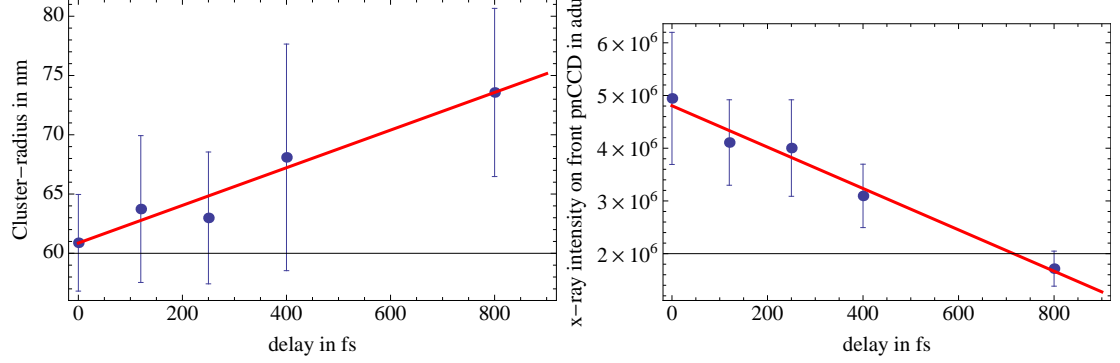


Figure 4.8: Left: Average Xenon cluster size of intense hits as a function of pump–probe delay Δt . Right: Average intensity on the front pnCCD of intense hits as a function of the pump–probe delay Δt .

at different times contribute to the light peak and therefore lower the average signal. And this would imply that lower pulse energy LCLS pulses can differ vastly from their anticipated time.

The time-of-flight analysis in this thesis accounts for both of these effects and additionally corrects for a common baseline.

4.4 Data filtering

As described in the above sections, LCLS produces large amounts of data. This data has to be filtered to a point, where it can be used for phase retrieval. The coincident detection of diffraction image and time of flight spectroscopy allow great freedom to filter on useful events. For the present work, a useful event is the interaction of X-ray pump – X-ray probe with a single cluster system. On the one hand, cluster produce the most intense signal on pnCCD and TOF detectors when they are in the center of the intensity profile of the LCLS beam [86]. On the other hand, as the time delay Δt of the X-ray pump – X-ray probe is increased, the nanoplasma expansion leads to a decrease in signal on the pnCCD (see figure 4.8). This can be extrapolated to an extreme, where cluster would not produce any signal on the front pnCCD. In order to filter on the full bandwidth of interesting hits, a series of filters have been applied. Filtering on ion time of flight high charge states has been successful in overall gathering images resolving pump–probe dynamics. In figure 4.8 left, the xenon pump–probe data has been automatically pre-filtered on xenon ion high-charge states, leaving several thousand events that were then semi-automatically reduced to over 350 single-hit

diffraction images. In this semi-automatic process it was determined, whether it was a single hit and the size of a cluster. The size determinations have been performed using the first maxima as described (see section 2.3.1). The remaining events indicate a linear average cluster radius increase of $\sim 15\%$ over the course of the first 800 fs at a given pump pulse energy. However, to perform phase retrieval and to solve the inverse problem, bright hits containing many photons are required. Therefore, an additional hitfinder on a snippet of the rear pnCCD detector has been implemented. This hitfinder determines the scattering intensity in single hits and brightest hits that show pump-probe dynamics have been selected undergo a phase retrieval to reveal their electron density. Events show dynamics, when the 1d reduction of the intensity profile differs from the scattering of an intact sphere, i.e. $F_{\text{intact}}^2/I \gg 1$.

4.5 Phase retrieval from a single diffraction pattern

As deducted in section 2.3.1, coherent diffractive imaging merely measures the intensity in reciprocal space and the phase information, i.e. complex fields, are lost. Iterative algorithms can retrieve this lost information because there are only limited sets of phases that uniquely reproduce the diffraction image [116, 117]. To fully recover the original function, i.e. real and complex values of the diffraction pattern, the diffraction image must be oversampled [118]. Here, the Nyquist-Shannon sampling theorem says that a Fourier transformed object of size X can be fully recovered if its sampling rate is at the Nyquist rate of $\frac{1}{2X}$. The Nyquist rate can be translated into a minimum (pnCCD) pixelsize in realspace using the following relation between a discrete Fourier transform and pixel length Δ_r [119]

$$\Delta_r = \frac{\lambda L}{2X}, \quad (4.7)$$

with the wavelength λ , the length to the detector L and the object length along one dimension X . For typical experimental values, the sampling pixel size must be $\Delta_r \geq 2.7$ mm to fully recover the particle's (projected) electron density. In the present experiment, the pnCCD pixel size of $75 \times 75 \mu\text{m}^2$ samples the object sufficiently enough.

4.5.1 Principle of phase retrieval

To recover the phase from an oversampled diffraction pattern and thus reconstruct an image of the object, iterative algorithms have been developed [120]. Figure 4.9 illustrates such an iterative algorithm, where the image of an object $g_k(x)$ is Fourier transformed to reciprocal space $G_k(x)$ and then back again resulting in $g_{k+1}(x)$, while sufficing certain

4 Methods

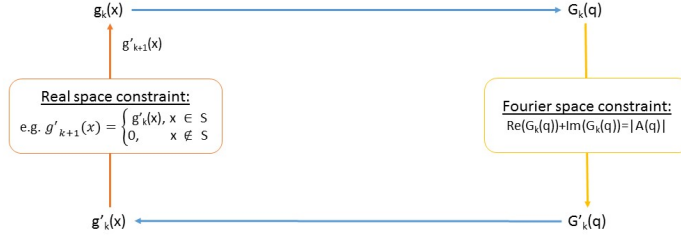


Figure 4.9: Principle of a phase retrieval algorithm. The real space object $g_k(x)$ is Fourier transformed to $G_k(q)$. The function $G_k(q)$ is altered to fit the constraints set in Fourier space, hence $G'_k(q)$. $G'_k(q)$ is inverse Fourier transformed to $g'_k(x)$. After fulfilling the real space constraints the iterative starts again using $g_{k+1}(x)$. From [120].

constraints.

The constraints are rather strict defined in the reciprocal space as they have to reproduce the actual measurement $I = A \cdot A^*$, which is sometimes called the modulo constraint. The criteria that need to be met in real space can be chosen more freely. Generally, the recovered object should be physical, i.e. should be of a certain (known) size. One can introduce a support structure S that meets the physical constraints and can therefore be used to, for example, zero outlying values. Throughout the iterations, the functions $g_k(x)$ evolve and eventually converge into a solution. If one uses the above criterion, one can show that the error between the reconstructions and the actual measurement continuously reduces, which is why it is commonly referred to as error-reduction algorithm [121].

4.5.2 2D reconstructions and limitations

Hawk program for 2D image phase retrieval

For all image reconstructions in 2D, the Hawk software package [122] has been used. Hawk is available under the GNU General Public License² and can be downloaded with installation instructions from <https://github.com/FXIhub/hawk>. In previous efforts

²Hawk copyright: <https://github.com/FXIhub/hawk/blob/master/Copyright>

Parameter	Setting
Starting Guess	random phases
Autocorrelation Selection	threshold
Autocorrelatlon Threshold	0.04
Phasing method beta	0.9
Beta range	0 - ∞
Enforce positivity	false
Enforce real	false
Perturb weak reflections	false
Phasing algorithm	raar
Blur	12 - 0.7
Blur range	0 - 12000
Center image	false
Object area	0.0022 - 0.0019
Object area range	0-8000
Support update algorithm	area

Table 4.1: Typical parameter used in the Hawk software package

to retrieve a real-space image from FEL based coherent diffractive imaging, Hawk has been used successfully in several reconstructions, ranging from viruses [92, 123] to other objects [124]. The usage of the program is straight forward in three steps. First, the diffraction images are transformed into the '.cxi' format [125]. Second, diffraction images are prepared in *Hawk's editor*, where particular effort has to be made to create a proper mask. The mask allows to forgo saturated, shadowed or otherwise faulty pixel. The software suite automatically interpolates between masked pixel. The successful edited '.cxi' file is then saved in Hawk's '.h5' format. Third, *Hawk's phaser* can be used to iteratively retrieve the phase from the '.h5' intensity file. Typical parameter for the phaser can be found in table 4.1. Here the *RAAR algorithm* [126] in combination with initially strong *blurs*, extension of the *phasing beta range* and a proper determination of the *object area* (support structur) resulted in useful reconstructions. Note, that the *object area* size differs from particle to particle, or intensity file to intensity file. After 10^5 to $1.5 \cdot 10^5$ iterations, the real space object typically converges.

Resolution enhancement through combination of rear and front pnCCD

While there is no consensus on how to define resolution in a coherent diffractive imaging pattern and the resulting reconstruction, there are various good estimates. A simple and conservative method to define resolution in a diffraction pattern is Abbe's criterion,

4 Methods

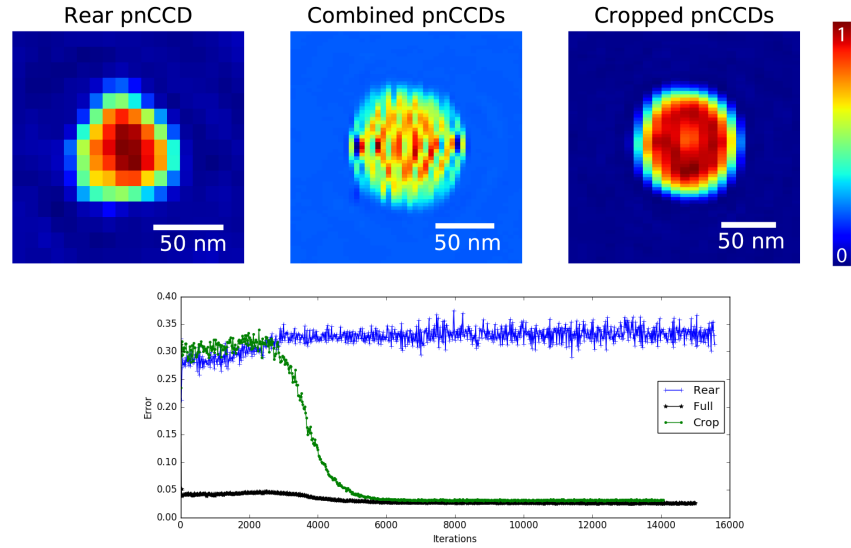


Figure 4.10: A set of reconstructions of Xe-cluster yielded from the diffraction pattern in figure 4.3 and the corresponding real-space error over number of iterations. The real space image gathered from the rear pnCCD uses no data from the front pnCCD. This reconstruction shows a not spherical object although the density distribution appears to be reasonable for a nano-particle. The real space image reconstructed from the full front and rear pnCCD data set appears to be a spherical object but the missing areas disturb the diffraction pattern and it has become unphysical. The Xe-cluster reconstructed without the dead areas has the expected spherical shape and the density distribution appears to be physical.

4.5 Phase retrieval from a single diffraction pattern

which comes from microscopy and calculates the minimal resolvable feature size in a diffraction pattern. The fundamental limit that the minimal resolvable feature size is depended on the wavelength has also given us the inspiration to build short-wavelength machines such as the free electron laser and synchrotron light sources.

First, we can verify that we are in the far field by fulfilling the following requirement [119]

$$\frac{d^2}{\lambda L} \ll 1 \quad (4.8)$$

with the wavelength of the X-rays λ , the distance to the detector L and the object size d .

In the far field, Abbe's criterion can be written down as

$$d = \frac{\lambda}{2n \sin(\frac{\Theta}{2})}, \quad (4.9)$$

with the minimal resolvable feature size d , the refractive index n and the half scattering angle $\frac{\Theta}{2}$. The scattering angle is restricted by either the active detector area, which goes back to the typical understanding of a numerical aperture, or the signal intensity up to certain angles. The latter is in interplay with the photon wavelength and object cross-sections. This interplay leads to the current assessment that very high energy photons, e.g. 8 keV photons that are commonly used for crystallographic purposes, scatter too little signal. Additionally, low- \vec{Q} scattering is often unresolvable due to straylight. As current results indicate, using 0.5 – 5 keV photons ultimately leads to higher resolution images than using 8 keV photons [89].

In the far field, we can use the following equation to investigate the pixel size [119]

$$\Delta_s = \frac{\lambda L}{N \Delta_d}, \quad (4.10)$$

with L being the length from the interaction region to the detector, Δ_i being the linear pixel size that is linked to each other through the discrete Fourier transformation and N being the side length of the discrete detector array.

Figure 4.10 top shows several reconstructions of xenon cluster at $\lambda = 1.0$ nm using different snippets of the diffraction pattern in figure 4.3. If just the rear pnCCD is used for reconstructions, a maximum scattering angle of $\Theta \approx 4.2^\circ$ is recorded, which results in a minimal resolvable feature size of $d \approx 14$ nm. However, in the present data a shadow is cast on the CCD reducing the maximum scattering angle in the image '**Rear pnCCD**' to $\Theta \approx 3.8^\circ$ and thus the resolution to $d \approx 15$ nm. The pixel size is $\sim 10\text{nm} \times \sim 12\text{nm}$.

4 Methods

The image '**Combined pnCCDs**' uses the whole data including the empty areas next to the rear pnCCD. The image shows an unphysical electron density distribution, which originates from the empty areas next to the rear pnCCD data. In these areas, the interpolation along the Y-axis/ extrapolation along the X-axis fails. The next image '**Cropped pnCCDs**' uses data in full extend along the Y-axis but crops the image along the X-axis such that the blank areas are excluded. The reconstruction converges into an object that appears physical. The maximum scattering angle here is $\Theta \approx 9.2^\circ$ and the resolution thus $d \approx 6$ nm. The pixel size here is $\sim 10\text{nm} \times \sim 3\text{nm}$.

This is a factor ~ 5 improvement over common cited studies in single particle imaging [123] and still a factor ~ 3 better than [127], where measured diffraction patterns have been 'computationally purified'. The resolution enhancement due to the combination of detectors can be abused further using EMC algorithms [91], where multiple images can be arranged due to their rotation and averaged, hence filling the missing areas next to the rear pnCCDs and allowing 3D reconstructions with (few³) nanometer resolution.

4.5.3 1D projections and phase reconstructions

To display many effects in diffraction pattern, they have sometimes been reduced from two dimensions to merely one. A 1D representation of the data allows easy to interpret comparison to analytical models. To reduce the 2D diffraction data to 1D the program shown in appendix 8.3 has been employed. It is based on Matlab to efficiently iterate through pixel arrays. The input for this program are pedestal calibrated diffraction images that have unwanted areas masked out and a true image center defined. Key elements of the algorithm are to iterate through every pixel, filtering signal from noise, determining the \vec{Q} -value of every pixel and sum signal over \vec{Q} , while normalizing the data over pixel. Additionally, an algorithm has been designed to perform phase retrieval on the 1D data. This program is based on python and can also be found in appendix 8.4. The input for this algorithm are mirrored, zero-frequency (inverse) shifted 1D diffraction arrays. The algorithm follows the fundamental scheme described in sub-section 4.5.1. In the iterative algorithm, the realspace function is forced to be real and positive, which is also the error criterion in real space. The difference to the measured data yields the error criterion in Fourier space. The algorithm allows monitoring of the Fourier- and realspace error, the phase and the actual Fourier and realspace images. The iterative algorithm is aborted based on the error criterion.

³Depending on the position of the front pnCCD.

4.6 2D electron density and diffraction image simulations

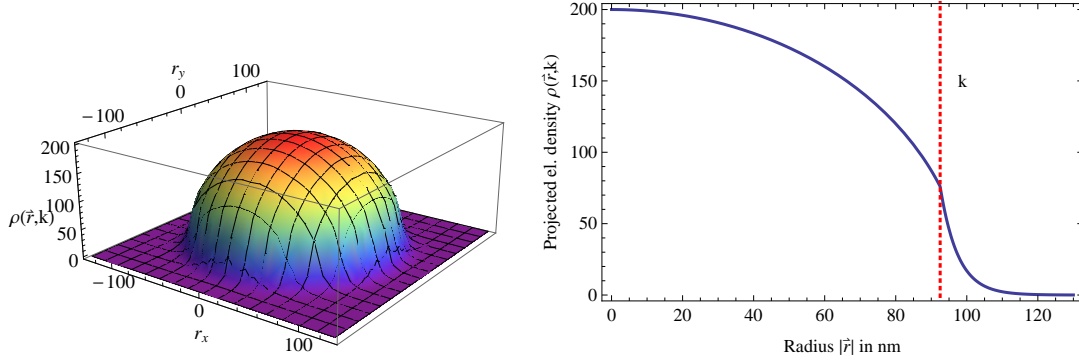


Figure 4.11: Left: Electron density of a $R \approx 100\text{nm}$ expanding sphere with $k = 5\text{ nm}$, projected onto a 2D plane. Right: Blue curve, spherical projection of the 2D projection to 1D. Red dashed line, point of expanding density at $k = 5\text{ nm}$.

4.6 2D electron density and diffraction image simulations

The interpretation of the helium cluster doped with xenon data requires a more thorough investigation than with 1D fits possible. Therefore two dimensional studies were performed to simulate electron densities of (doped) clusters. The electron density is then Fourier transformed to yield 2D diffraction images, which can be compared to the experimental data. The 2D simulations can then optionally be reduced to 1D using a spherical integration (see subsection 4.5.3) to be easily compared to the experimental data and other analytical models. The clusters are approximated using spheres, which is at the current resolution an acceptable estimation of the icosahedral cluster structure. In the simulated cluster, i.e. core-shell system, the shell consists of one large cluster with low electron density (helium) and the core comprises smaller dense spheres (xenon) at different locations within the shell. Furthermore, the spheres can expand to simulate the effect of a nanoplasma expansion. We can express such spheres using the formalism

$$\rho_i(\vec{r}, k) = \begin{cases} 2\sqrt{R^2 - |\vec{r}|^2} \cdot \rho_0 & \text{for } R - \frac{3k}{2} \geq |\vec{r}| \geq 0, \\ 2\sqrt{R^2 - |\vec{r}|^2} \cdot \rho_0 e^{\frac{(R - \frac{3k}{2}) - |\vec{r}|}{k}} & \text{for } R > |\vec{r}| - \frac{3k}{2}, \end{cases} \quad (4.11)$$

with ρ_0 being the density, R being the cluster radius and k an expansion coefficient such that

$$\int_0^\infty \rho(|\vec{r}|, k) d|\vec{r}| = R, \quad \text{if } 0 < k < R \quad (4.12)$$

4 Methods

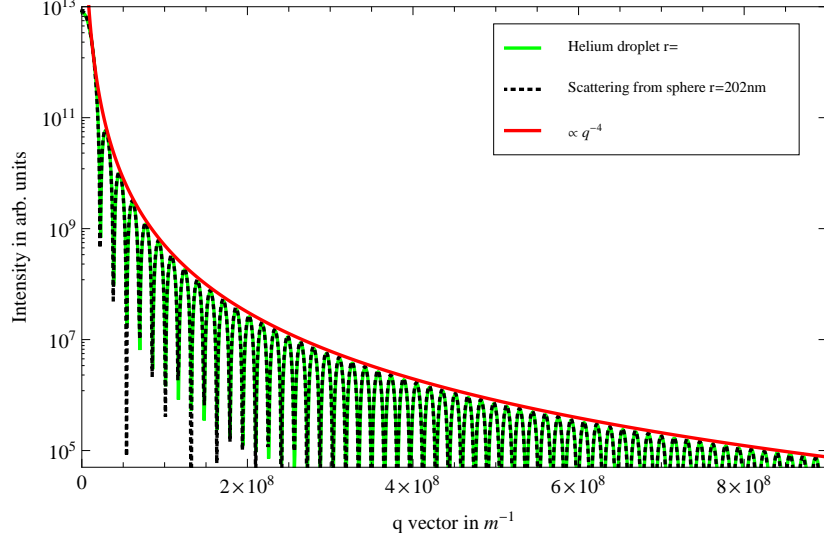


Figure 4.12: Comparison of analytical scattering from a sphere of radius $R = 202$ nm (black curve), equation 2.39, and scattering of a sphere of radius $R = 202$ nm from 2D simulations projected onto 1D (green, dashed curve). Envelope of scattering intensity, called Porod's law, which is $\propto q^{-4}$ (red curve). The analytical scattering and developed simulations agree well with each other.

Multiple spheres $\rho_i(\vec{r})$, with $i = 1, 2, 3, \dots$, can be positioned using $\vec{r} \rightarrow \vec{r} - \vec{r}_0$, with \vec{r}_0 being the center of mass of the sphere ρ_i . The density ρ_0 was set to $\rho_{0,\text{helium}} = 1$ for liquid helium and $\rho_{0,\text{xenon}} = \frac{3.640}{0.1412} \approx 25.8$ for xenon. The numerator of the fraction for $\rho_{0,\text{xenon}}$ is the density of bulk xenon in g/cm³ and the denominator is the density for liquid helium in g/cm³. Using equation (4.11), a large array of $\sim 1500 \times 1500$ is generated that is comparable to the combined pnCCD image array size. The array is then Fourier transformed using Matlab's *fft2* and the output is subsequently rearranged using *fftshift*.

Figure 4.12 shows a comparison of the analytical derived scattering of a sphere (see equation 2.39) with a radius of $r = 202\text{nm}$ (black, dashed line) and the scattering of the 2D simulations reduced to 1D (green, solid line). The red curve is the envelope of the functions, called Porod's law that scales with $\propto q^{-4}$. The developed simulation agrees well with the analytical scattering.

5 Results and discussion

This chapter explains the experimental data using the methods introduced in the previous chapter. For the X-ray pump– X-ray probe study, data on heterogeneous clusters, i.e. helium droplets doped with xenon, have been taken at different time delays Δt . To complement the data, pristine data, i.e. helium droplets and xenon droplets individually, have been recorded at different time delays Δt and the static case.

The chapter is organized as follows. Section 5.1 discusses the pristine xenon data and section 5.2 covers the pristine helium data. Section 5.3 shows the proof of principle that tampered layers mitigate radiation damage effects of an enclosed aerosol sample object.

5.1 Pristine xenon pump–probe data

5.1.1 iToF traces with xenon as sample

- Xe iToF dynamics
- Slightly more of Xe higher charge-states present at longer delays.

5.1.2 Xenon diffraction images

- Present study of 1D condensed diffraction images.
- Work out similarities to Tais radiation damage

5.1.3 Reconstructions of xenon cluster single shot images

- Present Xe - cluster reconstructions
- Show 1D reconstructions and 'damage process'

5.1.4 pnCCD image pump – probe considerations

- Considerations of pump and probe pulse in one pnCCD image.

5 Results and discussion

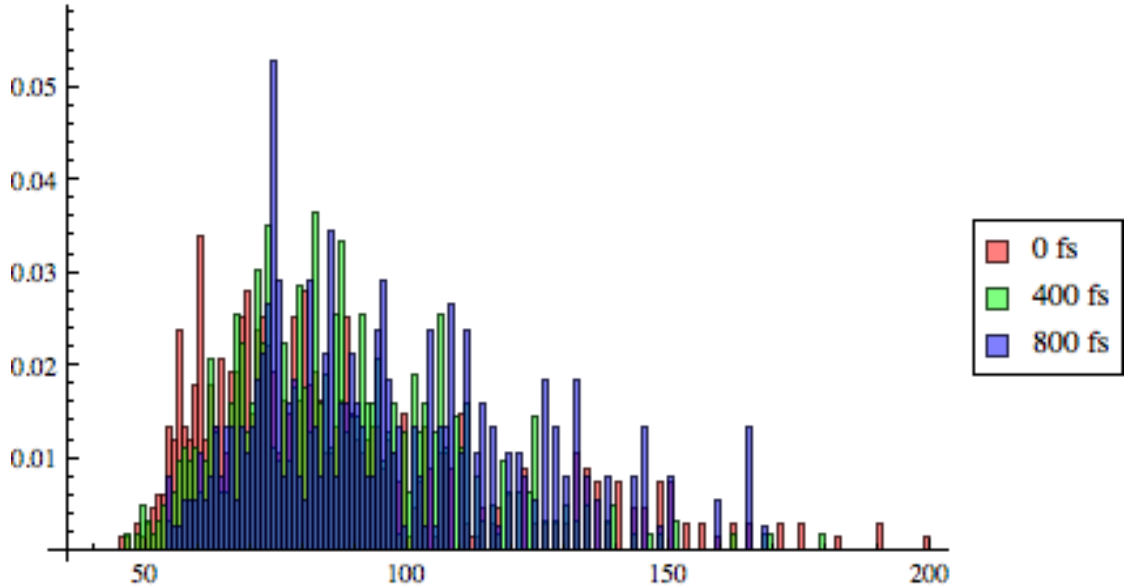


Figure 5.1: caption. MAKE IMAGE NICER

5.1.5 Time of flight data

5.2 Pristine helium cluster pump-probe data

- Presentation of He data

5.2.1 iTof data with helium as sample

- Subsection for iTof data, important to compare to HeXe data.

5.2.2 Diffraction images of helium cluster

- Work out radiation damage in 1D diffraction images.
- Introduce envelope to show the radiation damage effect - important to compare to HeXe data.
- Eventually subsection for reconstructions.

5.3 Helium-xenon core-shell systems and pump–probe data

- Presentation of HeXe data

5.3.1 Time-of-flight data of helium-xenon core-shell systems

- Show dynamics of XeHe data in tof trace.
- More hefty nanoplasma expansion in HeXe than in raw He.
- Complement with simulations from Phay.

5.3.2 Diffraction images of helium-xenon core shell systems

- Discuss diffraction images
- Show how scattering intensity drops from He signal but not from Xe signal.
- Eventually subsection for reconstructions.

5.3.3 Core-shell system considerations

5.4 Static data

-Include in other studies? Or appendix?

5.5 Conclusion of the X-ray pump – X-ray probe study

- Conclusion where the results are compared to each other
- This experiment shows that heterogeneous clusters, as in tampered layers, do inhibit radiation damage of the sample target while the sacrificial layer undergoes a rapid nanoplasma transition.

6 Summary and outlook

6.1 Summary

Summary here

6.2 Outlook

Outlook here

7 Bibliography

- [1] Ken R. Ferguson, Maximilian Bucher, John D. Bozek, Sebastian Carron, Jean-Charles Castagna, Ryan Coffee, G. Ivan Curiel, Michael Holmes, Jacek Krzywinski, Marc Messerschmidt, et al. The atomic, molecular and optical science instrument at the linac coherent light source. *J. Synchrotron Rad.*, 22(3):492–497, 2015.
- [2] Kenneth R. Ferguson. *Crystal Structure Determinations of Xenon Nanoparticles and X-ray Induced Transient Lattice Contraction in the Solid-to-Plasma Transition*. PhD thesis, Stanford University, Febuary 2016.
- [3] T. Osipov. personal communication, 2013.
- [4] Amadeo Perazzo. Lcls data analysis strategy. Technical report, SLAC National Accelerator Laboratory, Febuary 2016. URL https://portal.slac.stanford.edu/sites/lcls_public/Documents/LCLSDataAnalysisStrategy.pdf.
- [5] *Agilent Acqiris Programmer's guide*. Agilent Technologies, xz130 edition, June 2007. URL https://github.com/Maderthaner/Thesis/blob/master/manuals/U10xx_ProgrammersGuide.pdf. URL tested on October 13, 2016.
- [6] D. M. Mills, J. R. Helliwell, Å Kvick, T. Ohta, I. A. Robinson, and A. Authier. Report of the working group on synchrotron radiation nomenclature - Brightness, spectral brightness or brilliance? *Journal of Synchrotron Radiation*, 12(3):385, 2005. ISSN 09090495. doi: 10.1107/S090904950500796X.
- [7] Jens Als-Nielsen and Des McMorrow. *Elements of modern X-ray physics*. John Wiley & Sons, 2011.
- [8] SLAC National Accelerator Laboratory. Lcls aerial overlay, 2009. URL <https://www.flickr.com/photos/slaclab/8577624017/>. Downloaded from SLAC's Flickr.
- [9] Philip H. Bucksbaum, Ryan Coffee, and Nora Berrah. *Chapter 5 - The First Atomic and Molecular Experiments at the Linac Coherent Light Source*

7 Bibliography

- X-Ray Free Electron Laser*, volume Volume 60, pages 239–289. Academic Press, 2011. ISBN 1049-250X. doi: <http://dx.doi.org/10.1016/B978-0-12-385508-4.00005-X>. URL <http://www.sciencedirect.com/science/article/pii/B978012385508400005X>.
- [10] G J Williams. personal communication, 2016.
 - [11] Jeff Hecht. The history of the x-ray laser. *Optics and Photonics News*, 19(5): 26–33, 2008.
 - [12] A.M. Kondratenko and E. L. Saldin. Generation of coherent radiation by a relativistic electron beam in an undulator*. *Particle Accelerators*, 10:207–216, 1980. doi: 1003-0207.
 - [13] R. Bonifacio, C. Pellegrini, and L. M. Narducci. Collective instabilities and high-gain regime in a free electron laser. *Optics Communications*, 50(6):373–378, 1984. ISSN 00304018. doi: 10.1016/0030-4018(84)90105-6.
 - [14] P. Emma, R. Akre, J. Arthur, R. Bionta, C. Bostedt, J. Bozek, A. Brachmann, P. Bucksbaum, R. Coffee, F. J. Decker, et al. First lasing and operation of an ångstrom-wavelength free-electron laser. *Nat. Photonics*, 4(9):641–647, 2010. ISSN 1749-4885.
 - [15] L. Young, E. P. Kanter, B. Krassig, Y. Li, A. M. March, S. T. Pratt, R. Santra, S. H. Southworth, N. Rohringer, L. F. Dimauro, et al. Femtosecond electronic response of atoms to ultra-intense x-rays. *Nature*, 466(7302):56–61, 2010. ISSN 0028-0836. doi: 10.1038/nature09177.
 - [16] Bastian Holst and Arpad Horvath. Undulator, Jul 2005. URL <https://commons.wikimedia.org/wiki/File:undulator.png>.
 - [17] G. Brown, K. Halbach, J. Harris, and H. Winick. Wiggler and undulator magnets — A review. *Nuclear Instruments and Methods in Physics Research*, 208(1-3): 65–77, apr 1983. ISSN 01675087. doi: 10.1016/0167-5087(83)91105-5. URL <http://linkinghub.elsevier.com/retrieve/pii/0167508783911055>.
 - [18] Gwyn P Williams, editor. *X-ray data booklet*. Lawrence Berkeley National Laboratory, 2009. URL <http://cxro.lbl.gov/x-ray-data-booklet>.
 - [19] Kwang-Je Kim. Angular distribution of undulator power for an arbitrary deflection parameter K. *Nuclear Instruments and Methods in Physics Research Section A*:

- Accelerators, Spectrometers, Detectors and Associated Equipment*, 246(1-3):67–70, may 1986. ISSN 01689002. doi: 10.1016/0168-9002(86)90047-1. URL <http://linkinghub.elsevier.com/retrieve/pii/0168900286900471>.
- [20] Zhirong Huang and Kwang-Je Kim. Review of x-ray free-electron laser theory. *Phys. Rev. ST Accel. Beams*, 10:034801, Mar 2007. doi: 10.1103/PhysRevSTAB.10.034801. URL <http://link.aps.org/doi/10.1103/PhysRevSTAB.10.034801>.
 - [21] Daniela Rupp. *Ionization and plasma dynamics of single large xenon clusters in superintense XUV pulses*. Thesis, Technische Universität Berlin, 2013.
 - [22] Daniela Rupp. *Ionization and plasma dynamics of single large xenon clusters in superintense XUV pulses*. Springer, 2016.
 - [23] M. Bucher, K. R. Ferguson, Gorkhover T., and Bostedt C. A transmissive single-shot soft x-ray spectrometer. Unpublished study on feasibility of a spectrometer that is based on photoemission., 2014.
 - [24] Kwang-Je Kim, Yuri Shvyd'ko, and Sven Reiche. A proposal for an x-ray free-electron laser oscillator with an energy-recovery linac. *Phys. Rev. Lett.*, 100:244802, Jun 2008. doi: 10.1103/PhysRevLett.100.244802. URL <http://link.aps.org/doi/10.1103/PhysRevLett.100.244802>.
 - [25] L. B. Fletcher, H. J. Lee, T. Döppner, E. Galtier, B. Nagler, P. Heimann, C. Fortmann, S. LePape, T. Ma, M. Millot, et al. Ultrabright x-ray laser scattering for dynamic warm dense matter physics. *Nat. Photonics*, 2015. ISSN 1748-0221. doi: 10.1038/nphoton.2015.41.
 - [26] J. Amann, W. Berg, V. Blank, F. J. Decker, Y. Ding, P. Emma, Y. Feng, J. Frisch, D. Fritz, J. Hastings, et al. Demonstration of self-seeding in a hard-x-ray free-electron laser. *Nat. Photonics*, 6(10):693–698, 2012. ISSN 1749-4885. doi: 10.1038/NPHOTON.2012.180. URL <http://www.nature.com/nphoton/journal/v6/n10/pdf/nphoton.2012.180.pdf>.
 - [27] D. Ratner, R. Abela, J. Amann, C. Behrens, D. Bohler, G. Bouchard, C. Bostedt, M. Boyes, K. Chow, D. Cocco, F. J. Decker, Y. Ding, C. Eckman, P. Emma, D. Fairley, Y. Feng, C. Field, U. Flechsig, G. Gassner, J. Hastings, P. Heimann, Z. Huang, N. Kelez, J. Krzywinski, H. Loos, A. Lutman, A. Marinelli, G. Marcus, T. Maxwell, P. Montanez, S. Moeller, D. Morton, H. D. Nuhn, N. Rodes, W. Schlotter, S. Serkez, T. Stevens, J. Turner, D. Walz, J. Welch, and J. Wu.

7 Bibliography

- Experimental demonstration of a soft x-ray self-seeded free-electron laser. *Phys. Rev. Lett.*, 114:054801, Feb 2015. doi: 10.1103/PhysRevLett.114.054801. URL <http://link.aps.org/doi/10.1103/PhysRevLett.114.054801>.
- [28] E. Allaria, R. Appio, L. Badano, W. A. Barletta, S. Bassanese, S. G. Biedron, A. Borga, E. Busetto, D. Castronovo, P. Cinquegrana, et al. Highly coherent and stable pulses from the fermi seeded free-electron laser in the extreme ultraviolet. *Nat. Photonics*, 6(10):699–704, 2012. ISSN 1749-4885. doi: 10.1038/nphoton.2012.233. URL <Go to ISI>://WOS:000309523900018.
- [29] K. R. Ferguson, M. Bucher, T. Gorkhover, and Bostedt C. Absorption spectroscopy on co and CO_2 molecules. Unpublished study on CO and CO_2 molceules using an ion time of flight spectrometer that is proportional to the ion yield., 2014.
- [30] Victor Kimberg, Alvaro Sanchez-Gonzalez, Laurent Mercadier, Clemens Weninger, Alberto Lutman, Daniel Ratner, Ryan N Coffee, Maximilian Bucher, Melanie Mucke, Marcus Agaker, Conny Sathe, Christoph Bostedt, Joseph Nordgren, Jan-Erik Rubensson, and Nina Rohringer. Stimulated x-ray raman scattering - a critical assessment of the building block of nonlinear x-ray spectroscopy. *Faraday Discuss.*, pages –, 2016. doi: 10.1039/C6FD00103C. URL <http://dx.doi.org/10.1039/C6FD00103C>.
- [31] J. C. Castagna, B. Murphy, J. Bozek, and N. Berrah. X-ray split and delay system for soft x-rays at lcls. *J. Phys.: Conf. Ser.*, 425(15):152021, 2013. ISSN 1742-6596. doi: 10.1088/1742-6596/425/15/152021. URL <http://iopscience.iop.org/1742-6596/425/15/152021>.
- [32] Brendan F. Murphy, Jean-Charles Castagna, John D. Bozek, and Nora Berrah. Mirror-based soft x-ray split-and-delay system for femtosecond pump-probe experiments at lcls. In *X-Ray Free-Electron Lasers: Beam Diagnostics, Beamline Instrumentation, and Applications*, volume 8504, pages 850409–850409–7, 2012. doi: 10.1117/12.928538. URL <http://dx.doi.org/10.1117/12.928538>.
- [33] A. A. Lutman, R. Coffee, Y. Ding, Z. Huang, J. Krzywinski, T. Maxwell, M. Messerschmidt, and H. D. Nuhn. Experimental demonstration of femtosecond two-color x-ray free-electron lasers. *Phys. Rev. Lett.*, 110(13):134801, 2013. ISSN 0031-9007.
- [34] A Marinelli, D Ratner, AA Lutman, J Turner, J Welch, F-J Decker, H Loos,

- C Behrens, S Gilevich, AA Miahnahri, et al. High-intensity double-pulse x-ray free-electron laser. *Nature communications*, 6, 2015.
- [35] A. Picón, C. S. Lehmann, C. Bostedt, A. Rudenko, A. Marinelli, T. Osipov, D. Rolles, N. Berrah, C. Bomme, M. Bucher, G. Doumy, B. Erk, K. R. Ferguson, T. Gorkhover, P. J. Ho, E. P. Kanter, B. Krässig, J Krzywinski, A A Lutman, A M March, D Moonshiram, D Ray, L Young, S T Pratt, and S. H. Southworth. Hetero-site-specific X-ray pump-probe spectroscopy for femtosecond intramolecular dynamics. *Nature Communications*, 7(May):11652, 2016. ISSN 2041-1723. doi: 10.1038/ncomms11652. URL <http://www.nature.com/doifinder/10.1038/ncomms11652>.
- [36] Ken R. Ferguson, Maximilian Bucher, Tais Gorkhover, Sébastien Boutet, Hiromonobu Fukuzawa, Jason E. Koglin, Yoshiaki Kumagai, Alberto Lutman, Agostino Marinelli, Marc Messerschmidt, Kiyonobu Nagaya, Jim Turner, Kiyoshi Ueda, Garth J. Williams, Philip H. Bucksbaum, and Christoph Bostedt. Transient lattice contraction in the solid-to-plasma transition. *Science Advances*, 2(1), 2016. doi: 10.1126/sciadv.1500837. URL <http://advances.sciencemag.org/content/2/1/e1500837>.
- [37] Chelsea E Liekhush-Schmaltz, Ian Tenney, Timur Osipov, Alvaro Sanchez-Gonzalez, Nora Berrah, Rebecca Boll, Cedric Bomme, Christoph Bostedt, John D Bozek, Sebastian Carron, Ryan Coffee, Julien Devin, Benjamin Erk, Ken R Ferguson, Robert W Field, Lutz Foucar, Leszek J Frasinski, James M Glownia, Markus Gühr, Andrei Kamalov, Jacek Krzywinski, Heng Li, Jonathan P Marangos, Todd J Martinez, Brian K McFarland, Shungo Miyabe, Brendan Murphy, Adi Natan, Daniel Rolles, Artem Rudenko, Marco Siano, Emma R Simpson, Limor Spector, Michele Swiggers, Daniel Walke, Song Wang, Thorsten Weber, Philip H Bucksbaum, and Vladimir S Petrovic. Ultrafast isomerization initiated by X-ray core ionization. *Nature communications*, 6:8199, 2015. ISSN 2041-1723. doi: 10.1038/ncomms9199. URL <http://www.ncbi.nlm.nih.gov/pubmed/26354002>.
- [38] THE LINAC COHERENT LIGHT SOURCE-II PROJECT, 2014. URL <http://accelconf.web.cern.ch/AccelConf/IPAC2014/papers/tuoca01.pdf>.
- [39] P. Emma, K. Bane, M. Cornacchia, Z. Huang, H. Schlarb, G. Stupakov, and D. Walz. Femtosecond and subfemtosecond x-ray pulses from a self-amplified spontaneous-emission-based free-electron laser. *Phys. Rev. Lett.*, 92(7):074801, 2004.

7 Bibliography

- [40] H Haberland. *Clusters of atoms and Molecules I, vol. 52 of Springer Series in Chemical Physics*. Springer-Verlag, Berlin, 1994.
- [41] W Miehle, O Kandler, T Leisner, and O Echt. Mass spectrometric evidence for icosahedral structure in large rare gas clusters: Ar, kr, xe. *The Journal of chemical physics*, 91(10):5940–5952, 1989.
- [42] B W Vandewaal. Icosahedral, decahedral, fcc, and defect-fcc structural models for Ar-N clusters, $n \geq 500$ - how plausible are they? *J Chem Phys*, 98(6):4909–4919, 1993. ISSN 00219606. doi: 10.1063/1.464946.
- [43] Nina V. Krainyukova. 'The crystal structure problem' in noble gas nanoclusters. *Thin Solid Films*, 515(4):1658–1663, 2006. ISSN 00406090. doi: 10.1016/j.tsf.2006.05.041.
- [44] D. Lippmann, W. C. Schieve, and C. Canestaro. Clustering time dependence in molecular dynamics: A kinetic model. *The Journal of Chemical Physics*, 81(11):4969, 1984. ISSN 00219606. doi: 10.1063/1.447481. URL <http://link.aip.org/link/JCPA6/v81/i11/p4969/s1{&}Agg=doi>.
- [45] W.H. Zurek and W.C. Shieve. Multistep Clustering and Nucleation. *Journal of Physical Chemistry*, 84(12):1479–1482, 1980. ISSN 0022-3654. doi: 10.1021/j100449a010.
- [46] J. M. Soler, N. García, O. Echt, K. Sattler, and E. Recknagel. Microcluster growth: Transition from successive monomer addition to coagulation. *Phys. Rev. Lett.*, 49: 1857–1860, Dec 1982. doi: 10.1103/PhysRevLett.49.1857. URL <http://link.aps.org/doi/10.1103/PhysRevLett.49.1857>.
- [47] David R. Miller. Free jet sources. In Giacinto Scoles, editor, *Atomic and Molecular Beam Methods*, chapter 2, pages 14–53. Oxford University Press, Inc., 1988.
- [48] I. Yamada, J. Matsuo, N. Toyoda, and A. Kirkpatrick. Materials processing by gas cluster ion beams. *Materials Science and Engineering: R: Reports*, 34(6):231–295, 2001. ISSN 0927796X. doi: 10.1016/S0927-796X(01)00034-1. URL <http://www.sciencedirect.com/science/article/pii/S0927796X01000341>.
- [49] J. Farges, M. F. de Feraudy, B. Raoult, and G. Torchet. Structure and temperature of rare gas clusters in a supersonic expansion. *Surface Science*, 106(1-3):95–100, 1981. ISSN 00396028. doi: 10.1016/0039-6028(81)90186-2.

- [50] J Gspann. On the phase of metal clusters. In Frank Träger and Gisbert zu Putlitz, editors, *Metal Clusters*, pages 43–45, Berlin, Heidelberg, April 1986. Springer Berlin Heidelberg. ISBN 978-3-642-71571-6. URL http://dx.doi.org/10.1007/978-3-642-71571-6{_}7.
- [51] Sebastian Schorb. *Size-dependent ultrafast ionization dynamics of nanoscale samples in intense femtosecond x-ray free-electron laser pulses*. Thesis, Technische Universitat Berlin, 2012.
- [52] Otto F. Hagena. Cluster Formation in Expanding Supersonic Jets: Effect of Pressure, Temperature, Nozzle Size, and Test Gas. *The Journal of Chemical Physics*, 56(5):1793, 1972. ISSN 00219606. doi: 10.1063/1.1677455. URL <http://scitation.aip.org/content/aip/journal/jcp/56/5/10.1063/1.1677455>.
- [53] Otto F. Hagena. Nucleation and growth of clusters in expanding nozzle flows. *Surface Science*, 106(1-3):101–116, 1981. ISSN 00396028. doi: 10.1016/0039-6028(81)90187-4.
- [54] Otto F. Hagena. Condensation in free jets: Comparison of rare gases and metals. *Zeitschrift für Physik D Atoms, Molecules and Clusters*, 4(3):291–299, 1987. ISSN 01787683. doi: 10.1007/BF01436638.
- [55] Lawrence S Bartell. Diffraction studies of clusters generated in supersonic flow. *Chemical Reviews*, 86(3):491, 1986. ISSN 0009-2665. doi: 10.1021/cr00073a001.
- [56] Daniela Rupp, Marcus Adolph, Leonie Flückiger, Tais Gorkhover, Jan Philippe Müller, Maria Müller, Mario Sauppe, David Wolter, Sebastian Schorb, Rolf Treusch, Christoph Bostedt, and Thomas Möller. Generation and structure of extremely large clusters in pulsed jets. *Journal of Chemical Physics*, 141(4), 2014. ISSN 00219606. doi: 10.1063/1.4890323. URL <http://dx.doi.org/10.1063/1.4890323>.
- [57] T. E. Gough, M. Mengel, P. a. Rowntree, and G. Scoles. Infrared spectroscopy at the surface of clusters: SF₆ on Ar. *The Journal of Chemical Physics*, 83(10):4958, 1985. ISSN 00219606. doi: 10.1063/1.449757. URL <http://scitation.aip.org/content/aip/journal/jcp/83/10/10.1063/1.449757>.
- [58] Luis F. Gomez, Evgeny Loginov, Russell Sliter, and Andrey F. Vilesov. Sizes of large He droplets. *Journal of Chemical Physics*, 135(15), 2011. ISSN 00219606. doi: 10.1063/1.3650235.

7 Bibliography

- [59] Luis F. Gomez, Ken R. Ferguson, James P. Cryan, Camila Bacellar, Rico Mayro P. Tanyag, Curtis Jones, Sebastian Schorb, Denis Anielski, Ali Belkacem, Charles Bernando, et al. Shapes and vorticities of superfluid helium nanodroplets. *Science*, 345(6199):906–909, 2014.
- [60] André Guinier and Gérard Fournet. *Small-angle scattering of X-rays*. J. Wiley & Sons, New York, 1955.
- [61] David Attwood. *Soft x-rays and extreme ultraviolet radiation*. Cambridge university press, 2000. ISBN 0-521-65214-6.
- [62] Atomic calculation of photoionization cross-sections and asymmetry parameters, August 2016. URL <https://vuo.elettra.eu/services/elements/WebElements.html>.
- [63] JJ Yeh and I Lindau. Atomic subshell photoionization cross sections and asymmetry parameters: $1 \geq z \geq 103$. *Atomic data and nuclear data tables*, 32(1):1–155, 1985.
- [64] J-J Yeh. *Atomic calculation of photoionization cross-sections and asymmetry parameters*. Gordon & Breach Science Publ.; AT&T Bell Laboratories, 1993.
- [65] Robert D Cowan. *The theory of atomic structure and spectra*. University of California Press, 1981. URL <http://aphysics2.lanl.gov/tempweb/lanl/>.
- [66] Wolfgang Demtröder. *Experimentalphysik 3: Atome, Moleküle und Festkörper*. Springer Verlag, 2005.
- [67] Phay J. Ho. personal communication, August 2016.
- [68] M. Bucher, K. R. Ferguson, Gorkhover T., and Bostedt C. The lamp endstation in the amo instrument at the linac coherent light source. Unpublished study on the LAMP endstation with focus on the pnCCD detectors., 2016.
- [69] B. Rudek, S. K. Son, L. Foucar, S. W. Epp, B. Erk, R. Hartmann, M. Adolph, R. Andritschke, A. Aquila, N. Berrah, et al. Ultra-efficient ionization of heavy atoms by intense x-ray free-electron laser pulses. *Nat. Photonics*, 6(12):858–865, 2012. ISSN 1749-4885. doi: 10.1038/Nphoton.2012.261.
- [70] M.O. Krause, F.A. Stevie, L.J. Lewis, T.A. Carlson, and W.E. Moddeman. Multiple excitation of neon by photon and electron impact. *Physics Letters A*, 31

- (2):81–82, jan 1970. ISSN 03759601. doi: 10.1016/0375-9601(70)91039-X. URL <http://linkinghub.elsevier.com/retrieve/pii/037596017091039X>.
- [71] D. Coster and R. De L. Kronig. New type of auger effect and its influence on the x-ray spectrum. *Physica*, 2(1-12):13–24, jan 1935. ISSN 00318914. doi: 10.1016/S0031-8914(35)90060-X. URL <http://linkinghub.elsevier.com/retrieve/pii/S003189143590060X>.
 - [72] Th. Fennel, K.-H. Meiwes-Broer, J. Tiggesbaumker, P.-G. Reinhard, P. M. Dinh, and E. Suraud. Laser-driven nonlinear cluster dynamics. *Rev. Mod. Phys.*, 82: 1793–1842, 2010. doi: <http://dx.doi.org/10.1103/RevModPhys.82.1793>.
 - [73] Mathias Arbeiter and Thomas Fennel. Rare-gas clusters in intense vuv, xuv and soft x-ray pulses: signatures of the transition from nanoplasma-driven cluster expansion to coulomb explosion in ion and electron spectra. *New Journal of Physics*, 13(5):053022, 2011. doi: <http://dx.doi.org/10.1088/1367-2630/13/5/053022>.
 - [74] C Bostedt, M Adolph, E Eremina, M Hoener, D Rupp, S Schorb, H Thomas, A R B de Castro, and T Möller. Clusters in intense FLASH pulses: ultrafast ionization dynamics and electron emission studied with spectroscopic and scattering techniques. *Journal of Physics B: Atomic, Molecular and Optical Physics*, 43: 194011, 2010. ISSN 0953-4075. doi: 10.1088/0953-4075/43/19/194011.
 - [75] H Wabnitz, L Bittner, a R B de Castro, R Döhrmann, P Gürtler, T Laarmann, W Laasch, J Schulz, A Swiderski, K von Haeften, T Möller, B Faatz, A Fateev, J Feldhaus, C Gerth, U Hahn, E Saldin, E Schneidmiller, K Sytchev, K Tiedtke, R Treusch, and M Yurkov. Multiple ionization of atom clusters by intense soft X-rays from a free-electron laser. *Nature*, 420(6915):482–5, 2002. ISSN 0028-0836. doi: 10.1038/nature01197. URL <http://www.ncbi.nlm.nih.gov/pubmed/12466837>.
 - [76] T. Laarmann, A. R B De Castro, P. Gürtler, W. Laasch, J. Schulz, H. Wabnitz, and T. Möller. Interaction of Argon clusters with intense VUV-laser radiation: The role of electronic structure in the energy-deposition process. *Physical Review Letters*, 92(14):143401–1, 2004. ISSN 00319007. doi: 10.1103/PhysRevLett.92.143401.
 - [77] C. Bostedt, H. Thomas, M. Hoener, E. Eremina, T. Fennel, K. H. Meiwes-Broer, H. Wabnitz, M. Kuhlmann, E. Plönjes, K. Tiedtke, R. Treusch, J. Feldhaus, A. R B

7 Bibliography

- De Castro, and T. Möller. Multistep ionization of argon clusters in intense femtosecond extreme ultraviolet pulses. *Physical Review Letters*, 100(13):12–14, 2008. ISSN 00319007. doi: 10.1103/PhysRevLett.100.133401.
- [78] T. Laarmann, M. Rusek, H. Wabnitz, J. Schulz, A. R B De Castro, P. Görtler, W. Laasch, and T. Möller. Emission of thermally activated electrons from rare gas clusters irradiated with intense VUV light pulses from a free electron laser. *Physical Review Letters*, 95(6):3–6, 2005. ISSN 00319007. doi: 10.1103/PhysRevLett.95.063402.
- [79] Christoph Bostedt, Heiko Thomas, Matthias Hoener, Thomas Möller, Ulf Saalmann, Ionut Georgescu, Christian Gnadtke, and Jan Michael Rost. Fast electrons from multi-electron dynamics in xenon clusters induced by inner-shell ionization. *New Journal of Physics*, 12, 2010. ISSN 13672630. doi: 10.1088/1367-2630/12/8/083004.
- [80] Matthias Arbeiter and Thomas Fennel. Ionization heating in rare-gas clusters under intense XUV laser pulses. *Physical Review A - Atomic, Molecular, and Optical Physics*, 82(1):1–7, 2010. ISSN 10502947. doi: 10.1103/PhysRevA.82.013201.
- [81] M. Lezius, S. Dobosz, D. Normand, and M. Schmidt. Explosion Dynamics of Rare Gas Clusters in Strong Laser Fields. *Physical Review Letters*, 80(2):261–264, 1998. ISSN 0031-9007. doi: 10.1103/PhysRevLett.80.261.
- [82] E. Springate, N. Hay, J. W. G. Tisch, M. B. Mason, T. Ditmire, M. H. R. Hutchinson, and J. P. Marangos. Explosion of atomic clusters irradiated by high-intensity laser pulses: Scaling of ion energies with cluster and laser parameters. *Phys. Rev. A*, 61:063201, May 2000. doi: 10.1103/PhysRevA.61.063201. URL <http://link.aps.org/doi/10.1103/PhysRevA.61.063201>.
- [83] Tais Gorkhover, Sebastian Schorb, Ryan Coffee, Marcus Adolph, Lutz Foucar, Daniela Rupp, Andrew Aquila, John D. Bozek, Sascha W. Epp, Benjamin Erk, Lars Gumprecht, Lotte Holmegaard, Andreas Hartmann, Robert Hartmann, Günter Hauser, Peter Holl, Andre Hörmke, Per Johnsson, Nils Kimmel, Kai-Uwe Kühnle, Marc Messerschmidt, Christian Reich, Arnaud Rouzée, Benedikt Rudek, Carlo Schmidt, Joachim Schulz, Heike Soltau, Stephan Stern, Georg Weidenspointner, Bill White, Jochen Küpper, Lothar Strüder, Ilme Schlichting, Joachim Ullrich, Daniel Rolles, Artem Rudenko, Thomas Möller, and Christoph Bostedt. Femtosecond and nanometre visualization of structural dynamics in super-

- heated nanoparticles. *Nature Photonics*, 10(2):93–97, 2016. ISSN 1749-4885. doi: 10.1038/nphoton.2015.264. URL <http://www.nature.com/doifinder/10.1038/nphoton.2015.264>.
- [84] R. Neutze, R. Wouts, D. van der Spoel, E. Weckert, and J. Hajdu. Potential for biomolecular imaging with femtosecond x-ray pulses. *Nature*, 406(6797):752–757, 2000. ISSN 0028-0836. doi: 10.1038/35021099.
- [85] C. Bostedt, E. Eremina, D. Rupp, M. Adolph, H. Thomas, M. Hoener, A. R. de Castro, J. Tiggesbaumker, K. H. Meiwes-Broer, T. Laarmann, et al. Ultrafast x-ray scattering of xenon nanoparticles: imaging transient states of matter. *Phys. Rev. Lett.*, 108(9):093401, 2012. ISSN 1079-7114. doi: 10.1103/PhysRevLett.108.093401. URL <http://journals.aps.org/prl/abstract/10.1103/PhysRevLett.108.093401>.
- [86] T. Gorkhover, M. Adolph, D. Rupp, S. Schorb, S. W. Epp, B. Erk, L. Foucar, R. Hartmann, N. Kimmel, K. U. Kuhnel, et al. Nanoplasma dynamics of single large xenon clusters irradiated with superintense x-ray pulses from the linac coherent light source free-electron laser. *Phys. Rev. Lett.*, 108(24):245005, 2012. ISSN 1079-7114. doi: 10.1103/PhysRevLett.108.245005.
- [87] Stefan P. Hau-Riege and Henry N. Chapman. Modeling of the damage dynamics of nanospheres exposed to x-ray free-electron-laser radiation. *Physical Review E - Statistical, Nonlinear, and Soft Matter Physics*, 77(4):1–4, 2008. ISSN 15393755. doi: 10.1103/PhysRevE.77.041902.
- [88] Christian Peltz, Charles Varin, Thomas Brabec, and Thomas Fennel. Time-resolved x-ray imaging of anisotropic nanoplasma expansion. *Physical Review Letters*, 113(3):1–6, 2014. ISSN 10797114. doi: 10.1103/PhysRevLett.113.133401.
- [89] A. Aquila, A. Barty, C. Bostedt, S. Boutet, G. Carini, D. dePonte, P. Drell, S. Doniach, K. H. Downing, T. Earnest, et al. The linac coherent light source single particle imaging road map. *Structural Dynamics*, 2(4):041701, 2015. doi: <http://dx.doi.org/10.1063/1.4918726>.
- [90] Jochen Küpper, Stephan Stern, Lotte Holmegaard, Frank Filsinger, Arnaud Rouzée, Artem Rudenko, Per Johnsson, Andrew V. Martin, Marcus Adolph, Andrew Aquila, et al. X-ray diffraction from isolated and strongly aligned gas-phase molecules with a free-electron laser. *Phys. Rev. Lett.*, 112(8):083002, 2014. URL <http://link.aps.org/doi/10.1103/PhysRevLett.112.083002>. PRL.

7 Bibliography

- [91] Ne Te Duane Loh and Veit Elser. Reconstruction algorithm for single-particle diffraction imaging experiments. *Physical Review E - Statistical, Nonlinear, and Soft Matter Physics*, 80(2):1–20, 2009. ISSN 15393755. doi: 10.1103/PhysRevE.80.026705.
- [92] Tomas Ekeberg, Martin Svenda, Chantal Abergel, Filipe R.N.C. Maia, Virginie Seltzer, Jean-Michel Claverie, Max Hantke, Olof Jonsson, Carl Nettelblad, Gijs van der Schot, et al. Three-dimensional reconstruction of the giant mimivirus particle with an x-ray free-electron laser. *Phys. Rev. Lett.*, 114:098102, Mar 2015. doi: 10.1103/PhysRevLett.114.098102.
- [93] Stefan P. Hau-Riege, Sébastien Boutet, Anton Barty, Saša Bajt, Michael J. Bogan, Matthias Frank, Jakob Andreasson, Bianca Iwan, M. Marvin Seibert, Janos Hajdu, Anne Sakdinawat, Joachim Schulz, Rolf Treusch, and Henry N. Chapman. Sacrificial tamper slows down sample explosion in FLASH dffraction eperiments. *Physical Review Letters*, 104(February):1–4, 2010. ISSN 00319007. doi: 10.1103/PhysRevLett.104.064801.
- [94] Matthias Hoener, Christoph Bostedt, H. Thomas, L. Landt, E. Eremina, H. Wabnitz, T. Laarmann, R. Treusch, A. R. B. De Castro, and Thomas Möller. Charge recombination in soft x-ray laser produced nanoplasmas. *Journal of Physics B: Atomic, Molecular and Optical Physics*, 41(18):181001, 2008. ISSN 0953-4075. doi: 10.1088/0953-4075/41/18/181001. URL [http://stacks.iop.org/0953-4075/41/i=18/a=181001?key=crossref.8294ba41a32aa89b0a6ec0f8b550687f\\$&delimiter](http://stacks.iop.org/0953-4075/41/i=18/a=181001?key=crossref.8294ba41a32aa89b0a6ec0f8b550687f$&delimiter)"026E30F\$nhttp://iopscience.iop.org/0953-4075/41/18/181001.
- [95] Michael Ziemkewitz, Camila Bacellar, Adam Chatterley, Maximilian Bucher, Kenneth Ferguson, Taisa Gorkhover, Maria Mueller, Daniela Rupp, Jones Curtis, Rico Mayro P. Tanyag, Charles Bernando, Luis Gomez, Justing Kwok, Sebastian Carron, James Cryan, Jacek Krzywinski, Alberto Lutmann, Agostino Marinelli, Timothy Maxwell, Jim Turner, Franz-Josef Decker, Daniel M. Neumark, Thomas Möller, Andrey Vilesov, Christoph Bostedt, and Oliver Gessner. Controlling explosion dynamics in mixed solid/superfluid clusters with x-ray double pulses. in preparation, 2017.
- [96] J. E. Augustin, A. M. Boyarski, M. Breidenbach, F. Bulos, J. T. Dakin, G. J. Feldman, G. E. Fischer, D. Fryberger, G. Hanson, B. Jean-Marie, R. R. Larsen, V. Lüth, H. L. Lynch, D. Lyon, C. C. Morehouse, J. M. Paterson, M. L. Perl, B. Richter, P. Rapidis, R. F. Schwitters, W. M. Tanenbaum, F. Vannucci, G. S.

- Abrams, D. Briggs, W. Chinowsky, C. E. Friedberg, G. Goldhaber, R. J. Hollebeek, J. A. Kadyk, B. Lulu, F. Pierre, G. H. Trilling, J. S. Whitaker, J. Wiss, and J. E. Zipse. Discovery of a narrow resonance in e^+e^- annihilation. *Phys. Rev. Lett.*, 33:1406–1408, Dec 1974. doi: 10.1103/PhysRevLett.33.1406. URL <http://link.aps.org/doi/10.1103/PhysRevLett.33.1406>.
- [97] R. E. Taylor. *Nucleon Form Factors above 6 GeV*. SLAC National Accelerator Laboratory, Sep 1967. URL <http://www.osti.gov/accomplishments/documents/fullText/ACC0171.pdf>.
- [98] M. L. Perl, G. S. Abrams, A. M. Boyarski, M. Breidenbach, D. D. Briggs, F. Bulos, W. Chinowsky, J. T. Dakin, G. J. Feldman, C. E. Friedberg, D. Fryberger, G. Goldhaber, G. Hanson, F. B. Heile, B. Jean-Marie, J. A. Kadyk, R. R. Larsen, A. M. Litke, D. Lüke, B. A. Lulu, V. Lüth, D. Lyon, C. C. Morehouse, J. M. Paterson, F. M. Pierre, T. P. Pun, P. A. Rapidis, B. Richter, B. Sadoulet, R. F. Schwitters, W. Tanenbaum, G. H. Trilling, F. Vannucci, J. S. Whitaker, F. C. Winkelmann, and J. E. Wiss. Evidence for anomalous lepton production in $e^+ - e^-$ annihilation. *Phys. Rev. Lett.*, 35:1489–1492, Dec 1975. doi: 10.1103/PhysRevLett.35.1489. URL <http://link.aps.org/doi/10.1103/PhysRevLett.35.1489>.
- [99] Raymond J. Kelleher, Peter M. Flanagan, and Roger D. Kornberg. A novel mediator between activator proteins and the rna polymerase ii transcription apparatus. *Cell*, 61(7):1209 – 1215, 1990. ISSN 0092-8674. doi: [http://dx.doi.org/10.1016/0092-8674\(90\)90685-8](http://dx.doi.org/10.1016/0092-8674(90)90685-8). URL <http://www.sciencedirect.com/science/article/pii/0092867490906858>.
- [100] C. Bostedt, J. D. Bozek, P. H. Bucksbaum, R. N. Coffee, J. B. Hastings, Z. Huang, R. W. Lee, S. Schorb, J. N. Corlett, P. Denes, et al. Ultra-fast and ultra-intense x-ray sciences: first results from the linac coherent light source free-electron laser. *J. Phys. B*, 46(16):164003, 2013. ISSN 0953-4075. doi: 10.1088/0953-4075/46/16/164003. URL <http://iopscience.iop.org/0953-4075/46/16/164003>.
- [101] J. D. Bozek. Amo instrumentation for the lcls x-ray fel. *The European Physical Journal Special Topics*, 169(1):129–132, 2009. ISSN 1951-6355. doi: 10.1140/epjst/e2009-00982-y. URL <http://link.springer.com/article/10.1140%2Fepjst%2Fe2009-00982-y>.
- [102] S. Moeller, J. Arthur, A. Brachmann, R. Coffee, F. J. Decker, Y. Ding, D. Dowell, S. Edstrom, P. Emma, Y. Feng, et al. Photon beamlines and diagnostics at lcls.

7 Bibliography

- Nucl. Instrum. Methods Phys. Res. A*, 635(1):S6–S11, 2011. ISSN 0168-9002. doi: 10.1016/j.nima.2010.10.125.
- [103] Stefan P. Hau-Riege, Richard M. Bionta, Dmitri D. Ryutov, Richard A. London, Elden Ables, Keith I. Kishiyama, Stewart Shen, Mark A. McKernan, Donn H. McMahon, Marc Messerschmidt, Jacek Krzywinski, Peter Stefan, James Turner, and Beata Ziaja. Near-ultraviolet luminescence of n_2 irradiated by short x-ray pulses. *Phys. Rev. Lett.*, 105:043003, Jul 2010. doi: 10.1103/PhysRevLett.105.043003. URL <http://link.aps.org/doi/10.1103/PhysRevLett.105.043003>.
- [104] W. F. Schlotter, J. J. Turner, M. Rowen, P. Heimann, M. Holmes, O. Krupin, M. Messerschmidt, S. Moeller, J. Krzywinski, R. Soufli, et al. The soft x-ray instrument for materials studies at the linac coherent light source x-ray free-electron laser. *Rev. Sci. Instrum.*, 83(4):043107–043107–10, 2012. ISSN 0034-6748. doi: 10.1063/1.3698294.
- [105] Regina Soufli, Mónica Fernández-Perea, Sherry L Baker, Jeff C Robinson, Eric M Gullikson, Philip Heimann, Valeriy V Yashchuk, Wayne R McKinney, William F Schlotter, and Michael Rowen. Development and calibration of mirrors and gratings for the soft x-ray materials science beamline at the linac coherent light source free-electron laser. *Appl. Opt.*, 51(12):2118–2128, 2012. doi: 10.1364/Ao.51.002118.
- [106] Georgi L. Dakovski, Philip Heimann, Michael Holmes, Oleg Krupin, Michael P. Minitti, Ankush Mitra, Stefan Moeller, Michael Rowen, William F. Schlotter, and Joshua J. Turner. The soft x-ray research instrument at the linac coherent light source. *J. Synchrotron Rad.*, 22(3):498–502, 2015.
- [107] Lothar Strüder, Sascha Epp, Daniel Rolles, Robert Hartmann, Peter Holl, Gerhard Lutz, Heike Soltau, Rouven Eckart, Christian Reich, Klaus Heinzinger, Christian Thamm, Artem Rudenko, Faton Krasniqi, Kai-Uwe Kühnel, Christian Bauer, Claus-Dieter Schröter, Robert Moshammer, Simone Techert, Danilo Miessner, Matteo Porro, Olaf Hälker, Norbert Meidinger, Nils Kimmel, Robert Andritschke, Florian Schopper, Georg Weidenspointner, Alexander Ziegler, Daniel Pietschner, Sven Herrmann, Ullrich Pietsch, Albert Walenta, Wolfram Leitenberger, Christoph Bostedt, Thomas Möller, Daniela Rupp, Marcus Adolph, Heinz Graafsma, Helmut Hirsemann, Klaus Gärtner, Rainer Richter, Lutz Foucar, Robert L. Shoeman, Ilme Schlichting, and Joachim Ullrich. Large-format, high-speed, x-ray pnccds combined with electron and ion imaging spectrometers in a multipurpose chamber for experiments at 4th generation light sources.

- Nuclear Instruments and Methods in Physics Research Section A: Accelerators, Spectrometers, Detectors and Associated Equipment*, 614(3):483 – 496, 2010. ISSN 0168-9002. doi: <http://dx.doi.org/10.1016/j.nima.2009.12.053>. URL <http://www.sciencedirect.com/science/article/pii/S0168900209023900>.
- [108] Jim Turner. personal communication, 2016.
- [109] Paul Kirkpatrick and A V Baez. Formation of optical images by X-rays. *Journal of the Optical Society of America*, 38(1895):766–774, sep 1948. ISSN 0030-3941. doi: 10.1364/JOSA.38.000766. URL <https://www.osapublishing.org/abstract.cfm?URI=josa-38-9-766>.
- [110] SPI collaboration. Straylight effects in the amo instrument at the lcls. Currently no publication in progress., 2015-2016.
- [111] *X-ray laser-induced ablation of lead compounds*, volume 8077, 2011. doi: 10.1117/12.890134. URL <http://dx.doi.org/10.1117/12.890134>.
- [112] J. Chalupsky, P. Bohacek, V. Hajkova, S. P. Hau-Riege, P. A. Heimann, L. Juha, J. Krzywinski, M. Messerschmidt, S. P. Moeller, B. Nagler, et al. Comparing different approaches to characterization of focused x-ray laser beams. *Nucl. Instrum. Methods Phys. Res. A*, 631(1):130–133, 2011. ISSN 0168-9002. doi: 10.1016/j.nima.2010.12.040. URL <http://www.sciencedirect.com/science/article/pii/S0168900210027816>.
- [113] G. Doumy, C. Roedig, S. K. Son, C. I. Blaga, A. D. DiChiara, R. Santra, N. Berrah, C. Bostedt, J. D. Bozek, P. H. Bucksbaum, et al. Nonlinear atomic response to intense ultrashort x rays. *Phys. Rev. Lett.*, 106(8):083002, 2011. ISSN 1079-7114.
- [114] J. M. Liu. Simple technique for measurements of pulsed gaussian-beam spot sizes. *Opt. Lett.*, 7(5):196–198, May 1982. doi: 10.1364/OL.7.000196. URL <http://ol.osa.org/abstract.cfm?URI=ol-7-5-196>.
- [115] Phay J. Ho, Christoph Bostedt, Sebastian Schorb, and Linda Young. Theoretical tracking of resonance-enhanced multiple ionization pathways in x-ray free-electron laser pulses. *Phys. Rev. Lett.*, 113:253001, 2014.
- [116] Yu.M. Bruck and L.G. Sodin. On the ambiguity of the image reconstruction problem. *Optics Communications*, 30(3):304–308, 1979. ISSN 00304018. doi: 10.1016/0030-4018(79)90358-4.

7 Bibliography

- [117] RHT Bates. Fourier phase problems are uniquely solvable in more than one dimension, 1. Underlying theory, 1981. ISSN 00304026.
- [118] D. Sayre. Some implications of a theorem due to Shannon. *Acta Crystallographica*, 5(6):843–843, 1952. ISSN 0365-110X. doi: 10.1107/S0365110X52002276.
- [119] G J Williams, H M Quiney, A G Peele, and K A Nugent. Fresnel coherent diffractive imaging: treatment and analysis of data. *New Journal of Physics*, 12(3):035020, 2010. URL <http://stacks.iop.org/1367-2630/12/i=3/a=035020>.
- [120] J R Fienup. Phase retrieval algorithms: a comparison. *Applied Optics*, 21(15):2758–2769, 1982. ISSN 0003-6935. doi: 10.1364/AO.21.002758. URL [http://www.opticsinfobase.org.ezproxy.lib.purdue.edu/viewmedia.cfm?uri=ao-21-15-2758&seq=0&html=true\\$\\delimiter"026E30F\\$npapers3://publication/doi/10.1364/AO.21.002758](http://www.opticsinfobase.org.ezproxy.lib.purdue.edu/viewmedia.cfm?uri=ao-21-15-2758&seq=0&html=true$\\delimiter).
- [121] J R Fienup. Reconstruction of an object from the modulus of its Fourier transform. *Optics letters*, 3(1):27–29, 1978. ISSN 0146-9592. doi: 10.1364/OL.3.000027.
- [122] Filipe R. N. C. Maia, Tomas Ekeberg, David van der Spoel, and Janos Hajdu. Hawk: the image reconstruction package for coherent X-ray diffractive imaging. *Journal of Applied Crystallography*, 43(6):1535–1539, Dec 2010. doi: 10.1107/S0021889810036083. URL <http://dx.doi.org/10.1107/S0021889810036083>.
- [123] M. M. Seibert, T. Ekeberg, F. R. Maia, M. Svenda, J. Andreasson, O. Jonsson, D. Odic, B. Iwan, A. Rocker, D. Westphal, et al. Single mimivirus particles intercepted and imaged with an x-ray laser. *Nature*, 470(7332):78–81, 2011. ISSN 0028-0836. doi: 10.1038/nature09748.
- [124] M Marvin Seibert, Sébastien Boutet, Martin Svenda, Tomas Ekeberg, Filipe R N C Maia, Michael J. Bogan, Nicusor Timmneanu, Anton Barty, Stefan Hau-Riege, Carl Caleman, et al. Femtosecond diffractive imaging of biological cells. *Journal of Physics B: Atomic, Molecular and Optical Physics*, 43(19):194015, 2010. URL <http://stacks.iop.org/0953-4075/43/i=19/a=194015>.
- [125] Filipe RNC Maia. The coherent x-ray imaging data bank. *Nat. Methods*, 9(9):854–855, 2012. ISSN 1548-7091. doi: 10.1038/nmeth.2110.
- [126] D Russell Luke. Relaxed averaged alternating reflections for diffraction imaging. *Inverse Problems*, 21(1):37, 2005. URL <http://stacks.iop.org/0266-5611/21/i=1/a=004>.

7 Bibliography

- [127] Max F. Hantke, Dirk Hasse, Filipe R. N. C. Maia, Tomas Ekeberg, Katja John, Martin Svenda, N. Duane Loh, Andrew V. Martin, Nicusor Timneanu, Daniel S. D. Larsson, et al. High-throughput imaging of heterogeneous cell organelles with an x-ray laser. *Nat. Photonics*, 8:943–949, 2014. doi: 10.1038/nphoton.2014.270.

8 Appendix

8.1 Source alignment

8.2 Python code psana example

Per popular request, a small analysis example is discussed¹. To begin, you should verify that you have a SLAC unix account and a SSH terminal with -Y flag capabilities². To access the psana computer cluster, see the following commands

```
$ ssh -Y USERNAME@pslogin.slac.stanford.edu  
$ ssh -Y psana  
$ source /reg/g/psdm/etc/ana_env.csh
```

This logs you into the SLAC psana server and loads the psana framework. Once logged in, make yourself familiar with the following python code ‘psmonLocal.py’. ‘psmonLocal.py’ has been created by Chris O’Grady for demonstration purposes and more information can be found under

<https://confluence.slac.stanford.edu/display/PSDM/Visualization+Tools>

```
from psana import *
ds = DataSource('exp=xpptut15:run=54:smd')
det = Detector('cspad')

for nevent, evt in enumerate(ds.events()):
    img = det.image(evt)
    y = img.sum(axis=0)
    break

from psmon.plots import Image, XYPlot
from psmon import publish
publish.local = True
plotimg = Image(0, "CsPad", img)
publish.send('IMAGE', plotimg)
```

¹Programming languages change their syntax often, it is therefore useful to visit the web-page
<https://confluence.slac.stanford.edu/display/PSDM/LCLS+Data+Analysis>

²If you have problems with graphics visualization, try the following link
<https://confluence.slac.stanford.edu/display/PCDS/Remote+Visualization>

8 Appendix

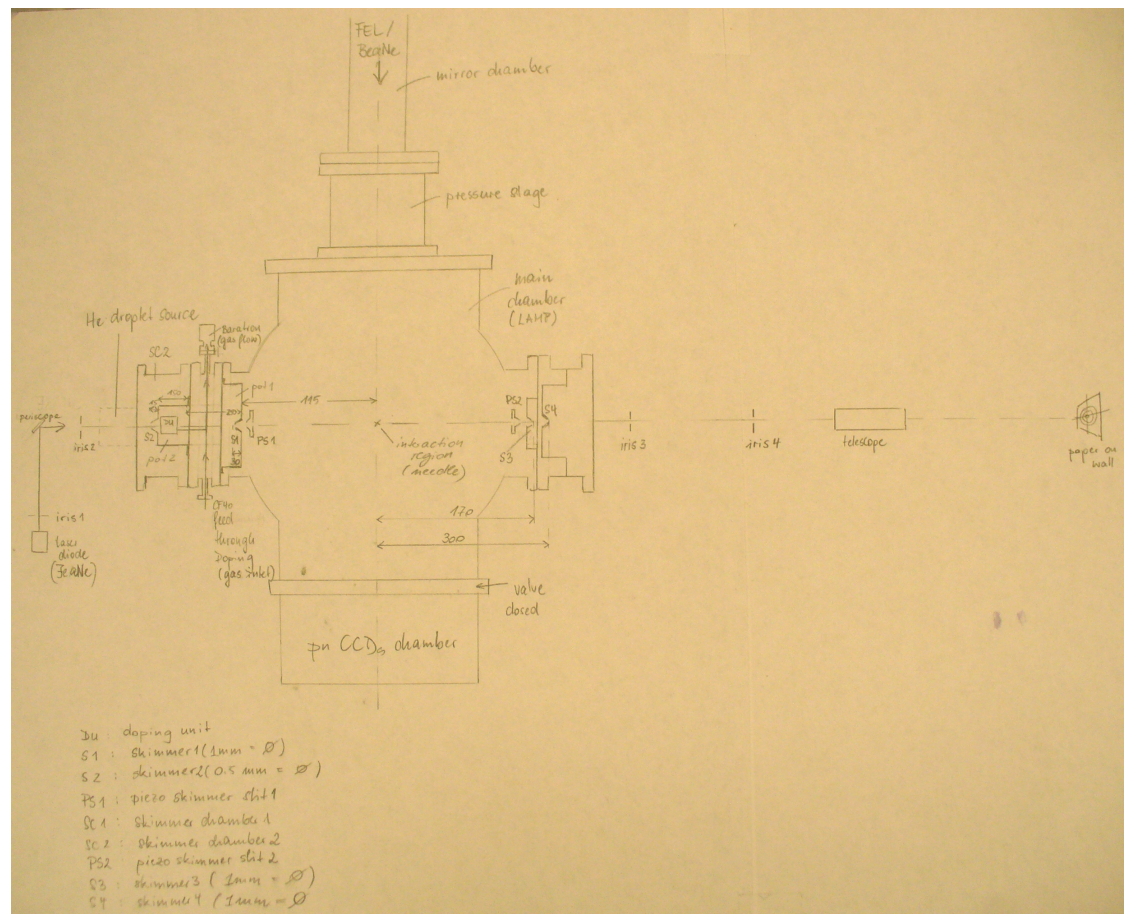


Figure 8.1: caption

B

8.3 Matlab code on spherical integrations

```
plotxy = XYPlot(0,"Y_vs._X",range(len(y)),y)
publish.send('XY',plotxy)
```

This script demonstrates a pixel detector image (CSpad) and an XY-Plot. Finally, run the script like any python script with

```
$ python /reg/g/psdm/tutorials/examplePython/psmonLocal.py
```

An interesting aspect to the python interaction is the 'TAB' method, where one can code without reading the documentation. Here a user should be on the psana servers and start ipython as follows

```
$ ipython

$ from psana import *
$ ds = DataSource('exp=amotut13:run=206')
$ det = Detector('AmoETOF.0:Acqiris.0')
$ det. (NOTE: user hits <TAB> after typing the ".") to get list of available methods)
$ evt = ds.events().next() (NOTE: getting an event, since the above "Definition" line
$ print det.waveform(evt) (NOTE: calling the "waveform" method as required by the abo
```

TBD

8.3 Matlab code on spherical integrations

Excerpt of the Matlab code that has been used to reduce 2D diffraction images to 1D arrays with the intensity as a function of the scattering vector \vec{Q} .

```
%% CENTER OF HIT
x_center=xLen/2; % Actually Y-center
y_center=yLen/2; % Actually X-center
for r=(1:1500)
    %looping over points
    for y=(1:yLen)
        for x=(1:xLen)
            %check if in circle
            if (x - x_center)^2 + (y - y_center)^2 < r^2
                %norm
                rnorm(r)=rnorm(r)+1;
                % testing for noise/photons
                if rearpnccd(x,y)>0
                    circleSum(r)=circleSum(r)+rearpnccd(x,y);
                end
            elseif (x - x_center)^2 + (y - y_center)^2 == r^2
                %norm
```

8 Appendix

```

rnorm( r)=rnorm( r)+(1/2);
% testing for noise/photons
if rearpnccd(x,y)>0
    circleSum( r)=circleSum( r)+(rearpnccd(x,y)/2);
end
end
end
if rnorm( r)==0
    rnorm( r)=1;
end
if r==1
    plotSum( r)=circleSum( r)/rnorm( r);
elseif rnorm( r)-rnorm( r-1)>0
    plotSum( r)=(circleSum( r)-circleSum( r-1))/(rnorm( r)-rnorm( r-1));
else
    plotSum( r)=0;
end
end

```

8.4 Python code on 1D phase-retrieval

An excerpt of the python code that has been used to iteratively retrieve the complex fields of the diffraction pattern.

```

# fft
for i in range(1,160):
    print i
    # Fourier Transform to Fourier Space
    fourierSpace = np.fft.fft(realSpaceAdjusted)
    # Get Phase in Fourier Space
    phase = np.exp(np.angle(fourierSpace)*I)
    # Take absolute measurement and multiply with phase
    ##fourierSpaceAdjusted = abs(target)*phase
    fourierSpaceAdjusted = abs(np.concatenate((target[0:len(phasedAmplitudes)], fourierSpaceAdjusted[len(phasedAmplitudes):len(phasedAmplitudes)])))
    #print len(fourierSpace)=len(fourierSpaceAdjusted)=len(phase)
    # Calculate Error in Fourier Space
    errorDiffraction = np.append(errorDiffraction,np.std(abs(fourierSpace[0:len(phasedAmplitudes)])))
    #####
    # Fourier Transform to Real Space
    realSpace = np.fft.ifft(fourierSpaceAdjusted)
    realSpaceAdjusted = realSpace.real

```

```

#print len(realSpace)==len(realSpaceAdjusted)
# Set values to zero where object not expected
#realSpaceAdjusted[30:len(realSpaceAdjusted)-30] = np.zeros(len(realSpaceAdjusted)-60)
realSpaceAdjusted[realSpaceAdjusted < 0] = 0
# Claculate error of Support
errorSupport = np.append(errorSupport,np.sum(np.abs(np.fft.ifftshift(realSpace))[0:len(realSpaceAdjusted)]))
#print errorSupport

```

8.5 Python code on combining detectors

Python code that has been used to combine pnCCD detectors.

```

# -*- coding: utf-8 -*-
import numpy as np
import h5py
import matplotlib.pyplot as plt
from matplotlib.colors import LogNorm
from scipy import interpolate
from random import random
from scipy import ndimage

#import argparse
#parser = argparse.ArgumentParser()
#parser.add_argument("hit", help="number of hit", type=int)
#args = parser.parse_args()

#####
# Things to adjust per shot
#####
## Path to data
dirPath = '/Users/Max/Desktop/working_2/doped_13%-800fs_shot_corr_to_1D'+'/'
## NO "/" at the end
#hitList = np.loadtxt(dirPath+'goodhits_r0108-scratch.txt', dtype="string")
pathToHDF5 = dirPath+'r0174_-5973757754469218304.h5' #hitList[args.hit] #there is a name bug in

#####
# Gaps between front top pnCCD and front bottom pnCCD to the middle of the rear pnCCD.
gapTop = 231
gapBot = 252

#####
# offset between rear and front pnCCDs
xShift = -1

#####
# Data about the cluster
#clusterSize = 3.04*10**-8
# must be float

```

8 Appendix

```

#clusterInt = 0.1#390239.0*10**43                                # must be float

#overlapCheck=0
#####
##### Things to adjust per run/experiment
pixelSizePnccd =75*10**-6                                         # Size of a pixel in m

distanceOfRearPnccd =0.74                                         # Distance from IR to
distanceOfFrontPnccd =0.36

gainRearPnccd =1./64.                                              # Detector multiplier
gainFrontPnccd =1.

scatteredWaveLength =1.5*10**-9                                    # Wavelength of the scattered photons

#####
## Functions
# Phi/2 - scatter angle
def PhiScatt(pixel, pixelSize, distanceToDetector):
    return np.arctan(pixel*pixelSize/distanceToDetector)

# q vector function
def qVector(pixel, pixelSize, distanceToDetector, waveLength):
    return 4.*np.pi*np.sin(PhiScatt(pixel, pixelSize, distanceToDetector)/2)/waveL

#####
## Reading detectors
intFrontTop =np.lib.pad(np.asarray(h5py.File(pathToHDF5, 'r')[ '/data/FrontPnCCDLab'] ,dt
intRear =np.asarray(h5py.File(pathToHDF5, 'r')[ '/data/RearPnCCDLab'] ,dtype='float32')
intFrontBottom =np.lib.pad(np.asarray(h5py.File(pathToHDF5, 'r')[ '/data/FrontPnCCDLab'] ,dt

#####
## Intensity normalization and offset of electronic noise.
intRear =intRear*(1/gainRearPnccd)*(distanceOfRearPnccd**2)*(1/distanceOfFrontPnccd**2)

# Offset rear
intRear[intRear<15*(1/gainRearPnccd)*(distanceOfRearPnccd**2)*(1/distanceOfFrontPnccd *2)] =0.0
# Offset front top
intFrontTop[intFrontTop<350] =0.0
# Offset front bottom
intFrontBottom[intFrontBottom<350] =0.0

#####
## Combining front detector

```

F

8.5 Python code on combining detectors

```

ztop = np.concatenate((intFrontTop, np.zeros((gapTop+gapBot, 1028)), intFrontBottom))

### Combining rear with front detector
# Creating pixel to q-vector correlation vectors
yRear, xRear = np.ogrid[(-len(intRear))/2:(len(intRear))/2,
-(len(intRear[0]))/2:(len(intRear[0]))/2]

# To transform q values from rear pnCCD to front pnCCD pixel values
qDiv = qVector(1, pixelSize=pixelSizePnccd, distanceToDetector=distanceOfFrontPnccd, waveLength=s)

# Actual transform
y_comb = len(ztop)/2
x_comb = len(ztop[0])/2

qyRear = np.round(qVector(yRear, pixelSize=pixelSizePnccd, distanceToDetector=distanceOfRearPnccd))
qxRear = np.round(qVector(xRear, pixelSize=pixelSizePnccd, distanceToDetector=distanceOfRearPnccd))

# Keep track of per pixel additions to create mean
norm = np.zeros(ztop.shape)

# Iterating over the array, is there a faster way than a for loop?
it = np.nditer(intRear, flags=['multi_index'])

while not it.finished:
    # read pixel transform coordinates
    y_idx = qyRear[it.multi_index[0],0]
    x_idx = qxRear[0,it.multi_index[1]]

    # add intensities and add to norm
    ztop[y_idx,x_idx] += it[0]
    norm[y_idx,x_idx] += 1

    it.iternext()

# Corrections to norm so not 1/0, seems inefficient but is fast enough.
norm -= 1
norm[norm<0]=0
norm += 1

# Actual mean value creation
ztop = ztop/norm

#####

```

8 Appendix

```
##### Plotting #####
#####
z_min, z_max = 0.1, intRear.max()

# plt.subplot(2,1,1)
#plt.pcolormesh(qXRear, qYRear, intRear, norm=LogNorm(vmin=z_min, vmax=z_max), cmap='p'
#plt.pcolormesh(qXFrontTop, qYFrontTop, intFrontTop, norm=LogNorm(vmin=z_min, vmax=z_m
#plt.pcolormesh(qXFrontBottom, qYFrontBottom, intFrontBottom, norm=LogNorm(vmin=z_min,
#plt.colorbar()

#plt.imshow(znew, norm=LogNorm(vmin=z_min, vmax=z_max), cmap='plasma')
#plt.colorbar()

# plt.subplot(2,1,2)

#combinedArray =np.add(intRearDownSmpldReshp, ztop)
w, h = plt.figaspect(1.)

plt.Figure(figsize=(w,h))
plt.imshow(ztop+0.1, norm=LogNorm(vmin=z_min, vmax=z_max), cmap='plasma')
#plt.colorbar()
plt.show()

### saving for further use, uncomment as needed
#np.save('0fs_cluster_weird_shot',combinedArray)
#np.save('0fs_cluster_shot_mask',invertMaskCombined)
#np.save('0fs_cluster_shot_ampSim',ampSimulatedCombinedArray)
#np.save('0fs_cluster_shot_phase',phaseSimulatedCombinedArray)
```

9 Index

- afterpulse, 24
- algorithm
 - coalescent-photon finding, 37
- amplitude
 - complex, 30
- Bragg's law, 41
- brilliance, *see also* spectral brightness
- cluster size, 23
- Coulomb potential, 40
- dispersion correction
 - complex, 31
- dopant, 24
- electron density
 - expanding, 41
- emittance, 11
- Fourier Transform, 82
- Free electron LASer in Hamburg
 - FLASH, 45
- Hagena, *see* scaling law
 - scaling parameter, 23
- Hawk software package, 76
- Helium
 - liquid density, 82
- imprint, 51
- ionization
 - energy, 33
 - inner, 40
 - multistep, 39, 40, 44
- LCLS, *see also* Linac Coherent Light Source
- lead tungstate, 51
- Linac Coherent Light Source, 6, 7
- Matlab, 80, 82
- microbunching, 11
- nanoplasma
 - transition, 40
- oversampling, 75
- Nyquist rate, 75
- Nyquist-Shannon sampling theorem, 75
- photoionization, 33
- pnCCD, 57, 58
 - CAMEX, 59
- common mode, 65
- Data Acquisition, 59
- gain, 59
- module, 58
- pedestal correction, 65

Index

pixel size, 58
psana, 59
 calibman, 65
pulse energy, 44

radiation damage, 44
refractive index, 31
 complex, 41

scaling law, 23
self-seeding, 14
 soft x-ray, 14
slippage, 11
spectral brightness, 5

time of flight
 mass spectroscopy, 45
time-of-flight, 49

undulator, 7

wave vector
 transfer, 28
wiggler, 7

X-ray
 Bremsstrahlung, 5
Xenon
 bulk density, 82

10 Acknowledgment

This has to be written.